

Development of nanoprobes for Optical and Magnetic Resonance Molecular Imaging

A THESIS PRESENTED BY

Ariya Saraswathy

TO



SREE CHITRA TIRUNAL INSTITUTE FOR MEDICAL
SCIENCES AND TECHNOLOGY
THIRUVANANTHAPURAM
INDIA

IN PARTIAL FULFILMENT OF THE REQUIREMENTS
FOR THE AWARD OF
DOCTOR OF PHILOSOPHY

2016

DECLARATION

I, Ariya Saraswathy, hereby certify that I had personally carried out the work depicted in the thesis entitled, “*Development of nanoprobes for Optical and Magnetic Resonance Molecular Imaging*”, except where due acknowledgment has been made in the text. No part of the thesis has been submitted for the award of any other degree or diploma prior to this date.

Thiruvananthapuram

26-03-2015

Ariya Saraswathy

Reg No: PhD/2010/09

Roll No: 6092

SREE CHITRA TIRUNAL INSTITUTE FOR MEDICAL SCIENCES & TECHNOLOGY, TRIVANDRUM

Thiruvananthapuram – 695011, INDIA

(An Institute of National Importance under Govt. of India)

Phone-(91)0471-2520273 Fax-(91)0471-2341814

Email: jayasree@sctimst.ac.in Web site – www.sctimst.ac.in



CERTIFICATE

This is to certify that **Mrs. Ariya Saraswathy**, in the Biophotonics and Imaging Division of this institute has fulfilled the requirements prescribed for the Ph. D. degree of the Sree Chitra Tirunal Institute for Medical Sciences and Technology, Thiruvananthapuram. The thesis entitled, ***“Development of nanoprobes for Optical and Magnetic Resonance Molecular Imaging”*** was carried out under my direct supervision. No part of the thesis was submitted for the award of any degree or diploma prior to this date.

* Clearance was obtained from the Institutional Ethics Committee/ Institutional Animal Ethics Committee for carrying out the study.

Thiruvananthapuram
26-03-2015

Dr. R S Jayasree. PhD
(Research Supervisor)

Scientist D & SIC
Biophotonics & Imaging Lab,
BMT wing, SCTIMST,
Thiruvananthapuram

The thesis entitled

***“Development of nanoprobes for Optical and Magnetic Resonance
Molecular Imaging ”.***

Submitted by

Ariya Saraswathy

for the degree of

Doctor of Philosophy

Of

**SREE CHITRA TIRUNAL INSTITUTE
FOR MEDICAL SCIENCES AND TECHNOLOGY,
THIRUVANANTHAPURAM - 695011**

is evaluated and approved by

.....
Dr. R S Jayasree. PhD.
(Research Supervisor)

.....
Examiner

*Dedicated To My father &
My daughters*

ACKNOWLEDGEMENT

I would like to express my heartfelt gratitude and respect to my supervisor Dr. R.S Jayasree, Scientist D and Head, Biophotonics and Imaging Division-BMT Wing, SCTIMST. Her guidance, timely advice, lively discussions, critical evaluations and encouragement helped in nurturing my passion for science throughout the course of study. This work would not have been possible without her support and encouragement. Her guidance not only added my knowledge but also increased my confidence and dedication in work. I thank her for the entire support offered during my Ph.D programme.

I am grateful to the former and present Director of SCTIMST and the present Head and the previous Heads, BMT Wing for all support provided during the course of my work.

I thank members of the doctoral advisory committee, Dr. C P Sharma, (former Head, BMT Wing, SCTIMST), Dr C Kesavadas, (Professor, Imaging Sciences & Intervention Radiology), Dr K Sreenivasan, (Scientist G, Polymer Analysis Lab) and Dr. P R HariKrishna Varma, (Scientist F, Bioceramic Lab) for their timely suggestions and critical comments.

I am thankful to Dr. Sundar Jayasingh, Deputy Registrar, Dr. Prabha D. Nair, Associate Dean for PhD affairs, Dean, and all members of academic division and Director's office for their administrative support and accounts office for their financial support.

I thank all the present and former staffs and students of Imaging Sciences & Interventional Radiology (IS&IR) department, SCTIMST for the help extended during MRI experiments.

I thank Dr.A Ajayaghosh, Dr. Manoj Rama Varma, Dr Sinoy Thomas, NIIST, TWM, Dr. P.A.Joy, NCL, Pune and Dr K G Suresh, IIT, Mumbai for providing DLS and VSM facilities.

I thank Dr. Sachin J Shenoy, DIMT, Dr. Harikrishnan V S, DLAS, Dr.Sabareeswaran A, Histopathology, Dr.Annie John, & Mrs. Susan, TEM, Dr.V.Kumary, Dr P R AnilKumar, TIC, Dr. V Kalliyanakrishnan, DPL, Dr. A. Maya Nandkumar, Mr

Pradeepkumar S S, Microbiology, Dr. Rekha, BioSurface Technology lab, Mr. Willi Paul, Mr. Durgadas, FADDS Dr. Suresh Babu, Mr. Vijayan, Mr. Nishad, Mr Sreekanth, Mr. Ansar, Bioceramic laboratory, Dr. Radhakumary, LPA, Dr. T Anoop Kumar and staff, MOM, all the staffs of DLAS, Mr. Merlin and Ms Rakhi, DTEPI for their assistance during the evaluations.

I thank all my friends of our department, Shaiju, Nimi, Hema, Parvathy, Madhu, Nimmi, Lakshmi, Resmi, Anish and Aneesha for their timely help and encouragement. I extend my thanks to all friends in BMT Wing and Hospital Wing, SCTIMST.

Thanks to the staff of various administrative departments and library of the Institute and fellow students in the campus for their lively companionship.

I am thankful to CSIR and BRNS for fellowships.

I further thank many who directly or indirectly helped me to prepare this thesis.

Words fail to express how grateful I am to my mother S. Santhilatha, being an eternal lamp through out my life without whom I may not have completed the work, my Sisters (Anupama & SreeLekshmi), brother (Vinod), for lifting me up to this phase of life and giving all support and encouragement in each fall back, I extend my thanks to my husband (Suseel Kumar) and sweet twin daughters (Swathi & Swaya) for adjusting with the situations during the due course of this PhD.

Above all, I remember with tears my beloved father Shri S.K. Sasidharan Thampi, the first teacher in my life, guiding me through my whole life even in his absence.

Last but not the least: I thank the force of nature which thrived me all the way in my life upto this level.

Ariya Saraswathy

Contents

DECLARATION.....	i
CERTIFICATE OF GUIDE.....	ii
APPROVAL OF THESIS.....	iii
ACKNOWLEDGEMENTS.....	v
LIST OF FIGURES.....	x
LIST OF TABLES.....	xiv
ABBREVIATIONS.....	xv
Synopsis.....	xvii
Chapter 1 INTRODUCTION.....	2
1.1 Imaging modalities for diagnosis.....	4
1.2 Magnetic Resonance Imaging.....	5
1.2.1. T ₁ Weighted MR Imaging.....	8
1.2.2 T ₂ Weighted MR Imaging.....	10
1.2.3 Contrast agents in MRI.....	11
1.2.3.1 T ₁ Contrast Agent.....	12
1.2.3.2 T ₂ Contrast agents.....	13
1.3 Optical Imaging.....	15
1.4 Nanotechnology and Imaging.....	16
1.5 Biomedical application of Magnetic Nanoparticles.....	19
1.6 Fluorescent nanoprobcs and its biomedical application.....	21

1.7 Liver Fibrosis.....	23
1.7.1 Passive Targeting of Liver abnormalities.....	25
1.7.2 Active Targeting of Liver abnormalities.....	26
1.8 Hypothesis.....	27
1.9 Objective of the Study.....	28
Chapter 2 REVIEW OF LITERATURE.....	30
2.1 Ironoxide nanoparticles.....	30
2.2 Gold nano clusters.....	36
2.3 Carbon nanodots.....	39
2.4 Hybrid Nanoparticles.....	45
Chapter 3 Materials & Methods.....	54
3.1 Materials.....	54
3.2 Development of ironoxide based MR Contrast Agents.....	55
3.2.1 Synthesis of Ultra small Super Paramagnetic Iron Oxide nanoparticles (USPIONs).....	55
3.2.2. Synthesis of Citrate stabilized USPIONs (C-SPIONs).....	55
3.2.3. Synthesis of Carbohydrate polymer stabilized SPIONs.....	56
3.2.3.1 Synthesis of Dextran Stabilized USPIONs (D-SPIONs).....	56
3.2.3.2. Synthesis of Alginate Stabilized SPIONs (A-SPIONs).....	57
3.2.3.3. Synthesis of Pullulan Stabilized SPIONs (P-SPIONs).....	57
3.3 Preparation of Multimodal nanoprobess.....	58

3.3.1 Synthesis of Multimodal D-SPIONs (DSPIONs-AT).....	58
3.3.2 Synthesis of Multimodal A-SPIONs (ASPION-AT).....	58
3.3.3 Synthesis of Multimodal P-SPIONs (PSPION-AT).....	59
3.4 Hybrid nanoprobe using Gold Clusters and SPIONs.....	59
3.4.1 Synthesis of Gold Clusters (AuC).....	59
3.4.2 Synthesis of Hybrid Nanomaterial (ASPION-Au).....	59
3.5 Hybrid nanoprobe using Carbon dots and SPIONs.....	60
3.5.1 Synthesis of Carbon Dots (CDTS).....	60
3.5.2 Synthesis of Hybrid Nanomaterial (ASPION-CDTS).....	60
3.5.3 Synthesis of Hybrid Nanomaterial (PSPION-CDTS).....	61
3.6 Characterization of the nanoparticles.....	61
3.6.1 Determination of Particle Size.....	61
3.6.1.1 Transmission Electron Microscopy (TEM).....	61
3.6.1.2 Dynamic Light Scattering Technique (DLS).....	62
3.6.2 Determination of Phase by X-ray Diffraction Technique (XRD).....	62
3.6.3 Surface characterization of the nanoparticles.....	62
3.6.3.1 Fourier Transform Infra-red spectroscopy (FT-IR).....	62
3.6.3.2 Thermo Gravimetric Analysis (TGA).....	63
3.6.4 Characterization of magnetic properties.....	63
3.6.4.1 Magnetic Property.....	63
3.6.4.2 Magnetic Relaxivity measurements.....	64

3.6.4.3 Hyperthermia.....	65
3.6.5 Characterization of Optical property.....	65
3.7 Hemocompatibility Evaluation.....	65
3.7.1 RBC aggregation.....	65
3.7.2 WBC and Platelet aggregation.....	66
3.7.3 Hemolysis assay.....	66
3.8 Cell culture studies.....	67
3.8.1 Cytotoxicity assessment.....	67
3.8.2 Cell uptake efficiency.....	67
3.9 In vivo studies.....	67
3.9.1 Animal Model Development for liver fibrosis.....	67
3.9.2 In vivo MRI measurements.....	68
3.9.3 In vivo Optical Imaging.....	69
3.9.3.1 In vivo Optical imaging of multimodal nanoprobe.....	69
3.9.3.2 In vivo optical imaging of Hybrid nanoprobe.....	69
3.9.4 Histological analysis.....	70
Chapter 4 Results.....	72
4.1 Preparation of ironoxide based MR Contrast Agents.....	72
4.1.1 Synthesis of Ultra small Super Paramagnetic Iron Oxide nanoparticles (USPIONs).....	72
4.1.2. Synthesis of Citrate stabilised SPIONs (C-SPIONs).....	73
4.1.3. Synthesis of Carbohydrate polymer stabilised SPIONs.....	73

4.1.4 Results of Physico-Chemical & Magnetic Characterisation.....	74
4.1.4.1 Determination of Particle Size.....	74
4.1.4.2 Results of X-ray Diffraction studies (XRD).....	76
4.1.4.3 Fourier Transform Infra-red spectroscopy (FT-IR).....	76
4.1.4.4 Thermo Gravimetric Analysis(TGA).....	78
4.1.4.5 Magnetic Property.....	80
4.1.4.6 Magnetic Relaxivity measurements.....	81
4.1.4.7 Hyperthermia.....	84
4.1.5 Hemocompatibility Evaluation.....	86
4.1.6 Cell culture studies.....	87
4.1.6.1 Cytotoxicity assessment.....	87
4.1.6.2 Cell uptake efficiency.....	88
4.1.7 In vivo studies.....	88
4.1.7.1 Animal Model Development for liver fibrosis.....	88
4.1.7.2 In vivo MRI measurements.....	89
4.1.8 Histopathological Analysis.....	92
4.2 Preparation of Multimodal nanoprobe.....	94
4.2.1 Optical Characterisation.....	95
4.2.2 In vivo Optical imaging of multimodal nanoprobe.....	99
4.3 Hybrid nanoprobe using Gold Clusters and SPIONs.....	101
4.3.1 Synthesis of Hybrid Nanomaterial (ASPION-Au).....	101

4.3.2 Physico-Chemical & Magnetic Characterisation.....	102
4.3.2.1 Determination of Particle Size.....	102
4.3.2.2 Results of X-ray Diffraction studies (XRD).....	102
4.3.2.3 Fourier Transform Infra-red spectroscopy (FT-IR).....	103
4.3.2.4 Magnetic Property.....	104
4.3.2.5 Magnetic Relaxivity.....	105
4.3.3 Optical Characterisation.....	106
4.3.4 Hemocompatibility Evaluation.....	108
4.3.5 Cell culture studies.....	109
4.3.5.1 Cytotoxicity assessment.....	109
4.4 Hybrid nanoprobe using Carbon dots and SPIONs.....	110
4.4.1 Synthesis of Hybrid Nanomaterial (ASPION-CDTS & PSPION-CDTS).....	110
4.4.2 Physico-Chemical & Magnetic Characterisation.....	110
4.4.2.1 Determination of Particle Size.....	110
4.4.2.2 Results of X-ray Diffraction studies (XRD).....	111
4.4.2.3 Fourier Transform Infra-red spectroscopy (FT-IR).....	112
4.4.2.4 Magnetic Property.....	113
4.4.2.5 Magnetic Relaxivity.....	114
4.4.3 Optical Characterisation.....	114
4.4.4 Hemocompatibility Evaluation.....	118
4.4.5 Cell culture studies.....	119

4.4.5.1 Cytotoxicity assessment.....	119
4.4.5.2 Cell uptake efficiency.....	120
4.4.6 In vivo studies.....	121
4.4.6.1 In vivo Optical imaging of Hybrid nanoprobes.....	121
4.4.7 Histopathological Analysis.....	123
Chapter 5 Discussions.....	126
5.1 Preparation of ironoxide based MR Contrast Agents.....	126
5.1.1 Synthesis of Ultra small Super Paramagnetic Iron Oxide nanoparticles (USPIONs).....	126
5.1.2. Synthesis of Citrate stabilised USPIONs (C-SPIONs).....	127
5.1.3. Synthesis of Carbohydrate Polymer Stabilised SPIONs.....	127
5.1.4. Physico-Chemical & Magnetic Characterisation.....	129
5.1.4.1 Determination of Particle Size.....	129
5.1.4.2 X-ray Diffraction (XRD) Studies.....	129
5.1.4.3 Fourier Transform Infra-red spectroscopy (FT-IR).....	130
5.1.4.4 Thermo Gravimetric Analysis (TGA).....	131
5.1.4.5 Magnetic Property.....	132
5.1.4.6 Magnetic Relaxivity measurements.....	133
5.1.4.7 Hyperthermia.....	136
5.1.5 Hemocompatibility Evaluation.....	137
5.1.6 Cell culture studies.....	138
5.1.6.1 Cytotoxicity assessment.....	138

5.1.6.2 Cell uptake efficiency.....	138
5.1.7 In vivo MRI studies.....	139
5.1.8 Histopathological Analysis.....	141
5.2 Preparation of Multimodal nanoprobes.....	142
5.2.1 Optical Characterisation.....	142
5.2.2 In vivo Optical imaging of multimodal nanoprobes.....	143
5.3 Hybrid nanoprobes using Gold Clusters and SPIONs.....	143
5.3.1 Synthesis of Hybrid Nanomaterial (ASPIONs-Au).....	143
5.3.2 Physico-Chemical & Magnetic Characterisation.....	144
5.3.2.1 Determination of Particle Size.....	144
5.3.2.2 X-ray Diffraction Studies (XRD).....	144
5.3.2.3 Fourier Transform Infra-red spectroscopy (FT-IR).....	144
5.3.2.4 Magnetic Property.....	145
5.3.2.5 Magnetic Relaxivity.....	145
5.3.3 Optical Characterisation.....	145
5.3.4 Hemocompatibility Evaluation.....	146
5.3.5 Cell culture studies.....	146
5.3.5.1 Cytotoxicity assessment.....	146
5.4 Preparation of Hybrid nanoprobes using Carbon dots and SPIONs.....	146
5.4.1 Synthesis of Hybrid Nanomaterial (ASPION-CDTS & PSPION-CDTS).....	146
5.4.2 Physico-Chemical & Magnetic Characterisation.....	147

5.4.2.1 Determination of Particle Size.....	147
5.4.2.2 X-ray Diffraction Studies (XRD).....	147
5.4.2.3 Fourier Transform Infra-red spectroscopy (FT-IR).....	148
5.4.2.4 Magnetic Property.....	148
5.4.2.5 Magnetic Relaxivity.....	149
5.4.3 Optical Characterisation.....	149
5.4.4 Hemocompatibility Evaluation.....	150
5.4.5 Cell culture studies.....	150
5.4.5.1 Cytotoxicity assessment.....	150
5.4.5.2 Cell uptake efficiency.....	151
5.4.6 In vivo studies.....	151
5.4.6.1 In vivo Optical imaging of Hybrid nanoprobe.....	151
5.4.7 Histopathological Analysis.....	152
Chapter 6 SUMMARY & CONCLUSIONS.....	154
6.1 Summary.....	154
6.2 Conclusion.....	160
6.3 Future prospects.....	161
BIBLIOGRAPHY.....	162
List of publications.....	186
Curriculum vitae.....	188

LIST OF FIGURES

Fig. No.	Caption	Page No.
1	Resolution Sensitivity and cost comparison of various imaging modalities.....	4
2	The growth of longitudinal magnetization (and tissue brightness) during the relaxation process following saturation.....	9
3	The decay of transverse magnetization during the relaxation process and the associated tissue brightness.....	11
4	Biomedical applications of nanoparticles.....	20
5	Schematic diagram of architecture of normal liver and the fibrotic liver.....	24
6	T ₂ -weighted images of livers after the stPEI-SPIO/MCLacZ nanocomplex injection at 3 h and 48 h.....	34
7	Fluorescence imaging in mice with interdermal injection of the carbon dots.....	42
8	Fluorescence imaging in mice with intravenous injection of the carbon dots.....	43
9	Schematic representation of formation of C-SPIONs.....	56
10	Schematic representation of formation of D-SPIONs.....	56
11	Schematic representation of formation of A-SPIONs.....	57
12	Schematic representation of formation of P-SPIONs.....	58
13	Illustration of the synthesis of the formation of ASPION-Au.....	60
14	TEM image of (a) bare USPIO (b) C-SPION (c) D-SPION (d) A-SPION and (e) P-SPION.....	74
15	Hydrodynamic size distribution of (a) bare USPIO (b) C-SPION (c) D-SPION (d) A-SPION and (e) P-SPION.....	75
16	XRD pattern of bare USPIOs,C-SPIONs,D-SPIONs,A-SPIONs & P-SPIONs	76
17	FTIR spectra of (a) bare USPIO (b) tri-sodium citrate and C-SPION (c) Dextran and D-SPION (d) Sodium Alginate and A-SPION and (e) Pullulan and P-SPION.....	77-78

18	TGA curves of C-SPION (A) and tri-sodium citrate (a) and D-SPION (B) and Dextran (b) and A-SPION (C) and Sodium Alginate (c) and P-SPION (D) and Pullulan (d)	79-80
19	M-H curve of (a) bare USPIO (b) C-SPION (c) D-SPION (d) A-SPION and (e) P-SPION.....	81
20	T ₁ & T ₂ weighted MR images for varying concentrations and Longitudinal (r ₁) and Transverse relaxation rates (r ₂) of (a) USPIO (b) C-SPION (c) D-SPION (d) A-SPION and (e) P-SPION.....	82-83
21	Time-Temperature plot of bare SPION, C-SPION, D-SPION, A-SPION and P-SPION on the application of varying current at a frequency of 275 KHz.....	85
22	The photographic image of the hemolysis study of all SPIONs, water and saline. (a) Blood aggregation studies (b).....	86
23	Percentage cell viability determined by MTT assay against different concentrations.....	87
24	Microscopic visualization of cell uptake of C-SPIONs, D-SPIONs, A-SPIONs, P-SPIONs and control without USPIOs on Prussian Blue staining.....	88
25	Photograph of intraperitoneal administration of CCl ₄ : Olive oil to induce liver fibrosis and SGOT and SGPT levels of fibrosis induced and control rat model..	89
26	Pre and post contrast in vivo MR images and corresponding pseudo coloured images and the percentage signal intensity variation from pre to post contrast MR image of liver fibrosis rat model administered with (a) C-SPIONs (b) D-SPIONs (c) A-SPIONs and (d) P-SPIONs.....	90-91
27	H&E, MT & PB stained histopathological images of normal liver and fibrosed rat liver administered with SPIONs probe. Photograph of normal and fibrosed liver	93
28	PB stained histopathological images of fibrosed liver in the case of C-SPIONs, D-SPIONs, A-SPIONs and P-SPIONs administration.....	94
29	Photographic image of SPION-AT in aqueous solution.....	95
30	Optical properties of multimodal nanoprobe: (a)UV-Vis absorption spectra (b) Excitation and (c) Emission Spectra of DSPION-AT, ASPION-AT and PSPION-AT compared with the Atto dye.....	95-96
31	Fluorescence images and the corresponding spectra of DSPION-AT with varying concentration.....	96

32	Fluorescence images and the corresponding spectra of ASPION-AT with varying concentration.....	97
33	Fluorescence images and the corresponding spectra of DSPION-AT with varying concentration.....	97
34	Excitation-Emission-Efficiency contour plots of DSPION-AT, ASPION-AT and PSPION-AT.....	98
35	Photograph of intraperitoneal administration of CCl ₄ : Olive oil and SGOT and SGPT levels of fibrosis induced and control mice model.....	99
36	<i>In vivo</i> optical images of control and fibrosis induced mice model administered with (a) DSPION-AT, (b) ASPION-AT and (c) PSPION-AT. The <i>ex vivo</i> fluorescence images of the organs on the right.....	100-101
37	TEM Micrograph of (a) Au cluster and (b) ASPION-Au.....	102
38	XRD pattern of ASPION-Au, ASPION and Au cluster.....	103
39	FTIR spectra of ASPION-Au compared with ASPION and Au cluster.....	104
40	Magnetisation curve (M-H) of ASPION-Au.....	105
41	Longitudinal (r ₁) & Transverse relaxation rates (r ₂) of ASPION-Au.....	105
42	Optical properties of Hybrid nanoprobe, ASPION-Au: (a)UV-Vis absorption spectra (b) Excitation and (c) Emission Spectra compared with Au cluster.....	106
43	Fluorescence images and the corresponding spectra of ASPION-Au and Au cluster with varying concentrations.....	107
44	Excitation-Emission-Efficiency contour plots of ASPION-Au and Au cluster...	108
45	Blood aggregation studies with ASPION-Au, Au cluster, positive control, PEI and negative control, saline.....	108
46	Percentage viability of cells against different concentrations determined by MTT assay.....	109
47	TEM Micrographic images of (a) CDTS (b) ASPION-CDTS and (c) PSPION-CDTS.....	111
48	XRD pattern of ASPION-CDTS, ASPION and CDTS and PSPION-CDTS, PSPION and CDTS.....	112
49	FTIR spectra of ASPION-CDTS & PSPION-CDTS.....	113

50	Magnetic hysteresis curve (M-H) of ASPION-CDTS and (b) PSPION-CDTS...	113
51	T_1 & T_2 weighted MR images for varying concentrations and Longitudinal (r_1) and Transverse relaxation rates (r_2) of (a) ASPION-CDTS and (b) PSPION-CDTS.....	114
52	Optical properties of CDTS based Hybrid nanoprobe, (a)UV-Vis absorption spectra (b) Excitation and (c) Emission Spectra of ASPION-CDTS, PSPION-CDTS and CDTS.....	115
53	Fluorescence images of CDTS with varying concentration.....	116
54	Fluorescence images of ASPION-CDTS with varying concentration.....	116
55	Fluorescence images of PSPION-CDTS with varying concentration.....	117
56	Excitation-Emission-Efficiency contour plots of (a) CDTS (b) ASPION-CDTS, and PSPION-CDTS.....	118
57	Blood aggregation studies: RBCs, WBC's and platelets incubated with ASPION-CDTS, PSPION-CDTS, positive control, PEI and negative control, saline.....	119
58	Percentage cell viability of CDTS, ASPION-CDTS and PSPION-CDTS determined by MTT assay.....	120
59	Fluorescence microscopic images of L929 cells on incubation with ASPION-CDTS and PSPION-CDTS.....	120
60	<i>In vivo</i> optical images of fibrosis induced mice model administered with ASPION-CDTS and PSPION-CDTS.....	122
61	H&E , MT and PB stained histopathological images of normal liver and early stage fibrosis of mice liver	123
62	PB stained histopathological images of fibrosed rat liver administered with ASPION-CDTS and PSPION-CDTS.....	124
63	Comparison of Pre to Post contrast Signal Intensity Ratio of the <i>in vivo</i> MR imaging.....	159

LIST OF TABLES

Table No.	Caption	Page No.
1	Comparison of important physical, optical and magnetic properties of different systems developed under this study	157

ABBREVIATIONS

ASGPR	:Asialoglycoprotein Receptor
AuC	:Gold nanoclusters
BSA	:Bovine Serum Albumin
CCl ₄	:Carbon tetrachloride
CDTS	:Carbon Dots
CNP	:Carbon NanoParticle
CNT	:Carbon NanoTubes
CT	:Computed Tomography
DLS	:Dynamic Light Scattering
DMEM	:Dulbecco's Modified Eagle's Medium
DNP	:Diamond Nanoparticle
DTPA	:diethylenetriamine pentaacetic acid
EDC	:1-Ethyl-3-(3-dimethylaminopropyl)carbodiimide
EPI	:Echo-Planar Imaging
EPR	:Enhanced Permeability and Retention
FBS	:Fetal Bovine Serum
fMRI	:Functional Magnetic Resonance Imaging
FNPs	:Fluorescent NanoProbes
FRET	:Fluorescence Resonance Energy Transfer
FTIR	:Fourier Transform Infra Red Spectroscopy
Gd	:Gadolinium
HCC	:HepatoCellular Cancer
HE	:Haematoxylin–Eosin
IONs	:Iron Oxide Nanoparticles
LFT	:Liver Function Test
MNPs	:Magnetic Nano Particles
MRA	:Magnetic Resonance Angiography
MRI	:Magnetic Resonance Imaging
Ms	:saturation magnetization
MT	:Masson's trichrome
MTT	:3-(4, 5- dimethylthiazol-2-yl)-2.5-diphenyl tetrazolium bromide
NIR	:Near Infra Red
NIRF	:Near Infra Red Fluorescence
NMR	:Nuclear Magnetic Resonance
NMV	:Net Magnetization Vector
NNI	:National Nanotechnology Initiative
PB	:Pearls' Prussian blue
PEG	:poly(ethyleneglycol)

PEI	:polyethyleneimine
PET	:Positron Emission Tomography
QD	:Quantum dots
RBC	:Red Blood Cells
RF	:Radio Frequency
SGOT	:Serum Glutamic Oxaloacetic Transaminase
SGPT	:Serum Glutamic Pyruvic Transaminase
SNP	:Silica NanoParticle
SPECT	:Single Photon Emission Coherence Tomography
SPIONs	:SuperParamagnetic IronOxide Nanoparticles
TE	:Echo Time
TEM	:Transmission Electron Microscopy
TGA	:Thermo Gravimetric Analysis
TI	:Inversion Time
TR	:Repetition Time
TSC	:Tri Sodium Citrate
USPIONs	:Ultra small SuperParamagnetic IronOxide Nanoparticles
VSM	:Vibration Sample Magnetometry
WBC	:White Blood Cells
WI	:Weighted Image
XRD	:X-ray Diffraction

SYNOPSIS

The field of biomedical technology necessitates advancement in research leading to improvement in the accuracy of diagnosis at the pertinent stage of vulnerable diseases. Disease diagnosis with different imaging modalities are currently available that differ both in their sensitivity and resolution. Combination of these complimentary modalities for accurate disease diagnosis has attained much attention in the present era. Recently, combination of Magnetic Resonance Imaging (MRI) and optical imaging has drawn great attention because they are highly complementary imaging techniques and a combined system has its own uniqueness. MRI, a powerful and highly useful tool in soft-tissue medical imaging and diagnostics, is highly effective in imaging tumors. Even though MRI provides high resolution images, for the effective discrimination between normal and tumor tissues, need for a contrast agent becomes essential in majority of cases. Currently used contrast agents are Gadolinium based complexes, which provide positive contrast, ie, hyperintensity, on (longitudinal) T₁-weighted images. Considering the safety profile and the suitability of the organ specific imaging using contrast agents, ironoxide based agents are preferred over Gd based ones. Optical imaging techniques, such as bioluminescence and fluorescence, are explicitly the most versatile and benefited techniques which can extract biochemical signatures involved in the disease progression. The main limitation of fluorescence based imaging with conventional fluorophores are poor skin/tissue penetration, wide emission and absorption bands, poor signal strength, short imaging times *in vivo*, and high susceptibility to photo bleaching. New advances in fluorescent nanomaterials can overcome many of these problems.

Tuning the emission maxima of the fluorescent probe to NIR region (700-900 nm) also helps in enabling the technique suitable for *in vivo* imaging. The development of multimodal nanoprobe by incorporating the magnetic and optical properties can serve as ideal platforms for so-called “multimodal imaging”. Magnetic nanoparticles, especially, ironoxide nanoparticles serve as target specific T₂ weighted MR contrast agents. The core size of the nanoparticles, surface chemistry, stability, coating thickness, and its magnetic property are some of the important factors that influence the performance of the iron oxide nanoparticles in the *in vivo* imaging application. Incorporation of the iron oxide nanoprobe with NIR dyes or with highly stable fluorescent nanoparticles like Gold clusters or Carbon dots will make magneto-optic imaging possible with a single probe.

Liver cancer is one among the top three killer diseases identified worldwide, the incidence of which is very high in India. Early stage of most of chronic liver diseases is the fibrosis which is a reversible condition and detection at this stage can regain functions of the liver to the normal order, completely. Liver fibrosis is the pathologic result of ongoing chronic inflammatory liver diseases and is characterized by the over activation of hepatic stellate cells (HSC) and Kupffer’s cells leading to the deposition of extracellular matrix (ECM) and collagen. The high iron affinity of Kupffer’s cells, the liver macrophages and the overexpression of asialoglycoprotein receptors with carbohydrate domain in liver malignancies favors the use of carbohydrate polymer stabilized ironoxide nanoparticles as liver specific contrast agents for diagnostic applications.

With these backgrounds, the main aim of this thesis work has been designed to develop multimodal/hybrid nanoprobe for the diagnosis of early stage of liver abnormalities using MR and Optical imaging techniques. The work summarizes the synthesis of ultra small superparamagnetic ironoxide nanoparticles (USPIONs) stabilised with different biopolymers exhibiting high relaxivity property and its application as contrast agents. The systematic physicochemical, magnetic and biological characterization of the developed USPIONs and subsequent *in vivo* imaging studies in liver fibrosis models of rat and mouse have also been included. To enable multifunctional application, fluorescing probes with emission in the NIR region were conjugated to USPIONs and their characterization and imaging potential are illustrated. For the development of hybrid nanoprobe, USPIONs were modified with additional nanostructures like gold clusters and carbon dots retaining both magnetic and optical properties of the individual materials. For this, NIR emitting gold clusters and carbon dots were prepared and characterized for their relevant properties. The *in vivo* imaging was also carried out to evaluate the feasibility of the developed multimodal nanoprobe for diagnostic applications.

The thesis has been structured into six chapters. Chapter 1 gives a general introduction about Magnetic Resonance Imaging, Optical imaging, the need for multimodal imaging, Magnetic nanoparticles, fluorescent NIR dyes, fluorescent nanoprobe, development of multimodal nanoprobe and liver disorders.

Chapter 2 summarizes the literature review of magnetic, fluorescent and multimodal nanoparticles used in the field of biomedical applications. The chapter also

elaborates an overview of the current scenario and the need for the improvement of currently available contrast agents.

Chapter 3 describes the materials & methods used for the development of multimodal nanoprobe for optical and magnetic resonance imaging. Materials used for the study are listed in the first section. The methods used for the synthesis of ultra small superparamagnetic ironoxide nanoparticles (USPIONs) followed by various surface modification of the nanoparticles are explained in the second section. USPIONs were prepared by co-precipitation method. Briefly, ferric and ferrous salts were mixed at particular proportions and a known amount of NaOH was added. The reaction was carried out in an inert atmosphere. Depending on the final application of the USPIONs, the surface of the USPIONs has been modified with different biocompatible moieties like citrate, dextran, alginate and pullulan. The synthesis route followed for the incorporation of the different SPIONs with fluorescent dyes and nanoparticles like gold clusters and carbon dots were also explicated. For *in vivo* optical imaging applications, incorporation of NIR emitting dye will yield remarkable outcome for imaging. The surface modified USPIONs were conjugated with Atto 700 dye which has emission around 700 nm, to enable multimodal imaging. Gold clusters were synthesized using Bovine Serum Albumin (BSA) with gold chloride and was conjugated with Alginate coated USPIONs. To prepare another hybrid nanoprobe for multimodal imaging Carbon dots (CDTS) was synthesized. A known amount of acetic acid was added slowly to phosphorous pentoxide (P₂O₅) for preparing carbon dots. The as synthesized carbon dots were incorporated with alginate and pullulan stabilized USPIONs. This chapter also

deals with the evaluation of physicochemical, optical and magnetic properties of the developed nanoprobes. The *in vitro* studies carried out for evaluating the biocompatibility of the nanoprobes and the potential for *in vivo* imaging carried out has also been explained in the present chapter. The *in vitro* studies include the evaluation of blood cell aggregation, cytotoxicity with MTT assay and cell uptake. Animal model for liver fibrosis was developed in rat and mice model and the feasibility of the MR and optical imaging by the intravenous administration of the developed contrast agents were also evaluated.

Chapter 4 elucidates the results of different phases of the development and application of the multimodal nanoparticles for liver imaging. The results include the size and phase analysis, physico-chemical characterizations of the ironoxide nanoparticles with four different surface modifications viz citrate, dextran, alginate and pullulan and the multimodal imaging materials developed with ironoxide nanoparticles and modified with fluorescent dye Atto 700, modified with gold clusters and carbon dots. The size and morphology of the USPIOs determined by TEM revealed an average particle size of 12nm and the magnetite phase of the particles was confirmed using the x-ray diffraction pattern. The coating efficiency of each of the USPIOs evaluated using FTIR and Thermo Gravimetric Analysis (TGA) provided corresponding shifts on comparison with the bare USPIOs and polymers. Magnetic hysteresis curve confirmed the superparamagnetic nature of USPIOs at room temperature with a high saturation magnetization. Decrease in pixel intensity of the phantom images with the increase in Fe concentration was observed for the T₂ weighted MR images. The NIR

emission of Atto dye was found to be retained in the Atto modified USPIOs which favoured the *in vivo* application. The CDTs with emission around 500nm were found more efficient than Au clusters with emission around 680nm on conjugation with USPIOs. So further *in vitro* and *in vivo* studies were carried out with the CDT-USPIOs samples. The chapter also describes the results that were obtained from the *in vitro* studies carried out for the evaluation of the extent of biocompatibility of the nanoparticles. All the nanoprobes were found to be hemo-compatible and cyto-compatible. The results of the *in vivo* evaluation of the studies carried out for the assessment of imaging efficiency includes the development of rat and mice model of liver fibrosis, MR imaging of the fibrosed rat model using the ironoxide based nanoprobes, and Optical imaging of fibrosed mice model using ironoxide nanoparticles modified with fluorescent dye and carbon dots. The remarkable contrast variation in the *in-vivo* MR imaging of fibrosed liver demonstrated the liver uptake and imaging potential of the surface modified USPIOs. Pullulan stabilized nanoprobes provided better pre to post contrast signal intensity ratio among all the nanoprobes developed. Histological analysis of liver sections performed after the MR imaging reconfirmed the fibrosis stage and the iron uptake in liver.

Chapter 5 comprises of the discussion part, which discusses in detail, the inferences of the study along with the possible theoretical explanation of the observations. The liver uptake of various ironoxide based nanoparticles of this study has been well compared and the reason for the range of uptake efficiency has also been well

interpreted, in this chapter. A comparison of the results of the present study with that of earlier reports has been made in this chapter.

Chapter 6 gives the conclusion, summary and future scope of the study. The development of multimodal contrast agents have been made possible in the study and the feasibility of the same in liver specific imaging also favored its application as contrast media. The hyperintense streaks observed in the hypointense fibrotic liver MR image further helped in visualising the extent of fibrosed tissue as part of the progression of liver disease which in turn will assist the radiologist to predict the degree of fibrosis. The prospective applications of the multimodal nanoprobe in the biomedical field are also accentuated in this section. The limitations of the current study have been identified and the future areas of research to produce NIR fluorescing hybrid nanoprobe for both imaging as well as therapeutic application have been projected. Citations are listed in the bibliographic section.

Chapter 1

INTRODUCTION

1. INTRODUCTION

The emergence of nanotechnology is expected to create innovations and play a vital role in various biomedical applications, not only in drug delivery and therapy, but also in molecular imaging, areas of biomarkers and biosensors. Considering the necessity in the field of healthcare, improvement in the diagnostic tools demands primary importance. Various *in vivo* imaging modalities like CT, MRI, ultrasound and PET have been used for diagnosis. Of all the imaging modalities available, Magnetic Resonance Imaging (MRI) gains wide acceptance because of its accuracy, high resolution and non invasive nature. Combining MRI with another one having high sensitivity and specificity, will yield better diagnostic efficiency. Such an emerging complimentary technique which can be combined with MRI is the optical imaging technique. The combined system will function with its own uniqueness.

Even though MRI provides images with intrinsic contrast, precise diagnosis of diseases especially liver associated malignancies often requires the use of intravenous contrast agents to enhance the image contrast for better visualization. Currently using Gadolinium based contrast agents, which on administration in patients with renal problems, induces a diseased condition, named, Nephrogenic systemic fibrosis (Bernstein *et al.*, 2012). Also, for the diagnosis of early fatty changes within the liver, transverse relaxation T_2 is preferred over longitudinal imaging relaxation T_1 due to low T_1 response of accumulated fat within liver than hepatocytes. Due to these reasons, contrast agents with enhanced transverse relaxivity like surface modified

superparamagnetic iron oxide nanoparticles (SPIONs) are preferred over conventional gadolinium based contrast agents with longitudinal relaxation properties for liver imaging. There are many contrast agents which are classified as iron oxide based transverse contrast agents. Important application of these contrast agents are liver, lymph node and vascular MR imaging (Wang, 2011; Bulte *et al.*, 2004). Non-specificity is one of the major drawbacks of these blood pool contrast agents. Moreover most of these contrast materials have already been withdrawn from the market due to safety concerns. It has been reported that low molecular weight polymers used for coating on such contrast agents has the tendency to cause osmotic nephropathy which leads to chronic renal failure (Feest, 1976; Morgan, Little & Evans, 1966) similar to the problem reported with the administration of Gadolinium based contrast agents. Surface modification of iron oxide nanoparticles with high molecular weight, water soluble and biocompatible polymers is an alternate way to overcome safety concerns.

Common optical imaging techniques work on the principle of fluorescence and can extract biochemical signatures involved in the disease progression. The major restraint of fluorescence based imaging with conventional fluorophores are poor skin/tissue penetration, wide emission and absorption bands, poor signal strength, short imaging times *in vivo*, and high susceptibility to photo bleaching.(Jiang *et al.*, 2010) Tuning the emission maxima of the fluorescent probe to NIR region (700-900 nm) and the development of custom designed fluorescent nanoprobes also helps in enabling the technique suitable for *in vivo* imaging. The development of multimodal nanoprobes by

incorporating the magnetic and optical properties can serve as ideal platforms for so-called “multimodal imaging”.

1.1 Imaging modalities for diagnosis

Timely and accurate disease diagnosis is the key to treat effectively any of the diseased conditions. It becomes more beneficial if this can be done at an early stage. The imaging techniques in the biomedical field serve as a better diagnostic tool. The techniques enable to visualize physiological structures, measure biological functions, and evaluate cellular and molecular events without requiring invasive procedures. The imaging modalities currently available includes magnetic resonance imaging (MRI); positron emission tomography (PET); single photon emission coherence tomography (SPECT); ultrasound imaging; computed (x-ray) tomography; bioluminescence imaging; fluorescence imaging; and other optical imaging methods.

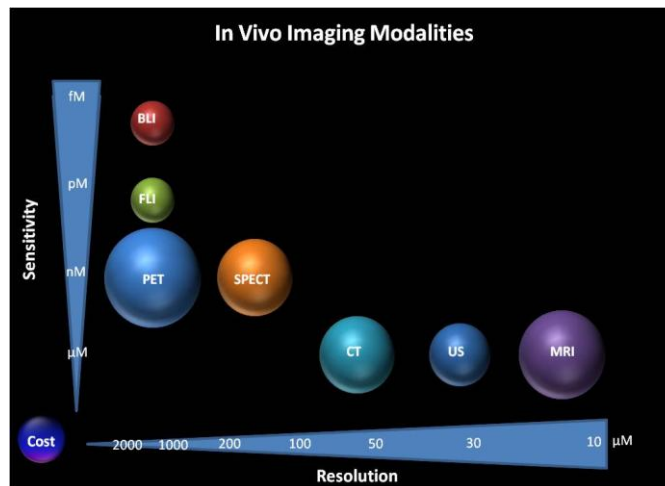


Figure-1. Resolution Sensitivity and cost comparison of various imaging modalities.

MRI uses a very strong magnetic field and radio waves to extract details of the structure and function of intact tissue in living organisms. SPECT and PET imaging techniques uses radionuclides to demonstrate function of a particular organ or system. Ultrasound imaging (sonography) uses high-frequency sound waves to view inside the body and CT technique uses x-rays to produce three dimensional images of the body. Optical imaging uses visible light and the special properties of photons to obtain detailed images of organs and tissues as well as smaller structures including cells and even molecules (Mundry *et al.*, 2003).

Among all the commonly available modalities, MRI, ultrasound and optical imaging techniques donot use ionizing radiation and are comparatively safer for disease diagnosis. Depending on the sensitivity, resolution and non-invasiveness, MRI and optical imaging techniques can be chosen as better measures of diagnostic modality (Figure 1).

1.2 Magnetic Resonance Imaging

Magnetic resonance imaging (MRI) is a noninvasive tool to investigate the internal anatomy and physiology of living subjects. They exploit the phenomenon of nuclear magnetic resonance (NMR), whereby atomic nuclei exposed to a strong magnetic field absorb and re-emit electromagnetic waves at a characteristic or ‘resonant’ frequency, which falls in the radio frequency (RF) range. Because there are no known adverse effects from either the strong magnetic fields or the radio waves, MRI is considered safe for human studies and longitudinal animal experiments. They are also

extremely versatile, because of the wealth of information contained in the signal, regarding both the gross structural properties of the tissue and its biochemistry.

. Glimpsing on the brief history of MRI, Felix Bloch and Edward Purcell, discovered the magnetic resonance phenomenon independently in 1946, both were awarded the Nobel Prize in 1952. In the period between 1950 and 1970, equipments based on NMR was developed and used for chemical and physical molecular analysis. In 1971, Raymond Damadian showed that the nuclear magnetic relaxation times (T_1 and T_2) of tissues and tumors differed, thus motivating scientists to consider magnetic resonance for the detection of disease. In 1973, MRI was first demonstrated on small test tube samples by Paul Lauterbur (Nobel Prize in Medicine,2003). In 1975, Richard Ernst proposed magnetic resonance imaging using phase and frequency encoding, and the Fourier Transformation methods. This technique forms the basis of current MRI scan. A few years later, in 1977, Raymond Damadian demonstrated a technique called field-focusing nuclear magnetic resonance. In this same year, Peter Mansfield (Nobel Prize in Medicine,2003) developed the echo-planar imaging (EPI) technique. This technique was developed in later years to produce images at video rates (30 ms / image). Edelstein and coworkers demonstrated imaging of the body using Ernst's technique in 1980. A single image could be acquired in approximately five minutes by this technique. By 1986, the imaging time was reduced to about five seconds, without sacrificing too much of image quality. The same year people were developing the NMR microscope, which allowed approximately 10 μm resolution on approximately one cm samples. In 1987 echo-planar imaging was used to perform real-time movie imaging of a single

cardiac cycle. In this same year Charles Dumoulin was perfecting magnetic resonance angiography (MRA), which allowed imaging of flowing blood without the use of contrast agents. In 1991, Richard Ernst was rewarded for his achievements in pulsed Fourier Transform NMR and MRI with the Nobel Prize in Chemistry. In 1992 functional MRI (fMRI) was developed. This technique allows the mapping of the function of the various regions of the human brain. The development of fMRI opened up a new application for EPI in mapping the regions of the brain responsible for thought and motor control. In 1994, researchers at the State University of New York at Stony Brook and Princeton University demonstrated the imaging of hyperpolarized ^{129}Xe gas for respiration studies (Guy and ffytche, 2005; Haacke *et al.*, 1999).

The basic physical phenomenon in MRI is the interaction between nuclei with a nonzero magnetic moment and an external magnetic field. For medical imaging, proton nuclei are used because of the abundance of water protons in the human body. When a patient is inside the powerful magnetic field of the scanner, in the presence of an external magnetic field these protons align their spin states either with or against the external magnetic field depending on whether it is in a low or high energy state. This phenomenon results in giving the object inside the magnetic field a very weak magnetic charge described by the net magnetization vector (NMV). Later, on the application of RF pulse, the spin states will get flipped between high and low energy states. The radio frequency required to cause the transition is dependent on an intrinsic property of the atom called the gyromagnetic ratio and the strength of the external magnetic field by the Larmor's equation, $\omega = egB/2m$ which is the underpinning principle behind MRI. On

removal of RF pulse, the flipped spin will relax back to its original equilibrium state and change the NMV back to its original orientation. This is known as relaxation, it is the extent of how quickly this process is achieved in MRI allows which to differentiate between the tissues in the body. There are two types of relaxation constants, T_1 (longitudinal or Spin-lattice) relaxation and T_2 (transverse or Spin-Spin) relaxation. T_1 relaxation is the time constant for the NMV to return back to align with the external magnetic field. T_2 relaxation is the time constant for the NMV to leave the plane perpendicular to the external magnetic field.(Hashemi *et al.*, 2004) The value of these constants are material dependent, specifically they depend on the water content of the material. Low water containing materials, such as bone and other hard tissues, have very fast relaxation constants while in contrast soft tissues have a high water content to give long relaxation constants. Additionally, since the water content in soft tissues is variable this gives MRI the ability not only to measure the relaxation process but to distinguish between different soft tissues by quantifying the relaxation constant. Diseased tissue, such as tumors, can be detected because relaxation rates will differ drastically from that of the normal tissue.

1.2.1. T_1 Weighted MR Imaging

T_1 weighted image (T_1 WI) is one of the basic pulse sequences in MRI which demonstrates differences in the T_1 relaxation times of tissues. For a T_1 weighted sequence set up, some of the terms to be familiarized are TE and TR. The echo time, TE refers to time between the application of radiofrequency excitation pulse and the peak of the signal induced in the coil. It is measured in milliseconds. The repetition time, TR is

the time from the application of an excitation pulse to the application of the next pulse. It determines how much longitudinal magnetization recovers between each pulse. It is measured in milliseconds.

A T_1 WI relies upon the longitudinal relaxation of a tissue's net magnetization vector (NMV). Basically, spins aligned in an external field (B_0) are flipped into the transverse plane by an RF pulse. They then slide back toward the original equilibrium of B_0 . All tissues do not get reverted back to equilibrium at an equal rate. T_1 of a tissue reflects the amount of time taken for the protons' spins of that particular tissue to realign with the main magnetic field (B_0).

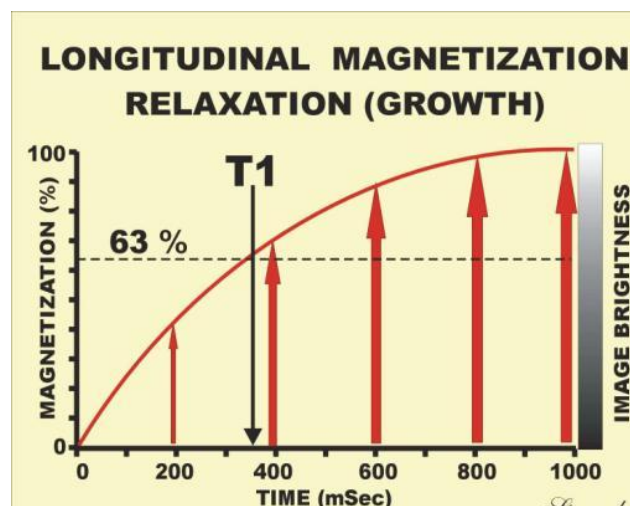


Figure-2. The growth of longitudinal magnetization (and tissue brightness) during the relaxation process following saturation.

The time required for the longitudinal magnetization to regrow, or relax, depends on characteristics of the material and the strength of the magnetic field. Longitudinal magnetization grows at an exponential rate following the relation, Magnetization, $M_t =$

$M_0 (1 - e^{-t/T_1})$, as shown in Figure-2, where M_t is the magnetization at time = t , the time after the 90° pulse, M_0 is the maximum magnetization at full recovery. The characteristic that varies from one type of tissue to another, and can be used to produce image contrast, is the time required for the magnetization to re-grow, or the relaxation time. This time, the longitudinal relaxation time, is designated T_1 . At a time T_1 , the signal will recover to 63% of its initial value after the RF pulse has been applied.

Fat quickly realigns its longitudinal magnetization with B_0 , and it therefore appears bright on a T_1 weighted image. Conversely, water has much slower longitudinal magnetization realignment after an RF pulse, and therefore has less transverse magnetization after a RF pulse. Thus, water has low signal and appears dark. If T_1 WI did not have short TRs, then all the protons would recover their alignment with the main magnetic field and the image would be uniformly intense. Selecting a TR shorter than tissues' recovery time allows one to differentiate them (i.e. tissue contrast).

1.2.2 T_2 Weighted MR Imaging

T_2 weighted image (T_2 WI) is another basic pulse sequence in MRI. This sequence highlights differences in the T_2 relaxation time of tissues. A T_2 WI relies upon the transverse relaxation of the net magnetization vector (NMV). After an RF excitation pulse, there is relaxation of the spins from the transverse plane toward the main longitudinal magnetic vector (B_0). This is T_1 weighting. At the same time, spins are decaying from their aligned precession in the transverse plane following the relation, $M_{XY} = M_{XY0} e^{-t/T_2}$. Differences in this decay are captured in T_2 weighting. The characteristics of transverse magnetization and relaxation are quite different from those

for the longitudinal direction. A major difference is that transverse magnetization is an unstable condition and the relaxation process results in the decay, or decrease, in magnetization, as shown in Figure-3. The T_2 value is the time required for 63% of the initial magnetization to dissipate. ie, at one T_2 , 37% of the initial magnetization is present.

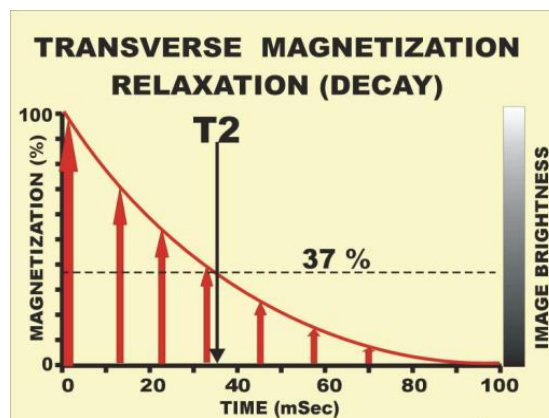


Figure-3. The decay of transverse magnetization during the relaxation process and the associated tissue brightness.

1.2.3 Contrast agents in MRI

MRI contrast agents are those chemical media on administration in to the body improves the visibility of internal body structures in MRI. MRI contrast agents may be administered by injection into the blood stream or orally, depending on the area of interest. Oral administration is well suited to G.I. tract scans, while intravascular administration proves more useful for most other scans. In MRI, the contrast enhancement occurs as a result of the interaction between the contrast agents and neighboring water protons, which can be affected by many intrinsic and extrinsic factors such as proton density and MRI pulse sequences. The contrast agents can be classified

according to the magnetic property of the agent, the dominant effect of the agent on the signal intensity and the bio-distribution of the agent. Based on the relaxation processes, the contrast agents are broadly classified into two, T_1 contrast agents and T_2 contrast agents.

1.2.3.1 T_1 Contrast Agent

T_1 contrast agents work through the shortening of T_1 relaxation time of protons located nearby. T_1 shortens with an increase in rate of stimulated emission from high energy states (spin anti-aligned to the main field) to low energy states (spin aligned parallel to the main field). Thermal vibration of the strongly magnetic metal ions in the contrast agent creates oscillating electromagnetic fields at frequencies corresponding to the energy difference between the spin states (via $E = h\nu$), resulting in the requisite stimulation. T_1 contrast agents enhance T_1 relaxation, a signal-increasing imaging effect, which gives positive contrast or bright signal that can be distinguished clearly from other pathogenic or biological conditions. T_1 contrast agents are based on paramagnetic ions and are used in the form of ion complexes. They have short life spans in the body and work in a nonspecific manner. Most T_1 contrast agents reside within the extracellular space, and usually interact with the blood so that they have many limitations as molecular probes for long time tracking (Geraldes and Laurent, 2009).

Paramagnetic materials are metals with unpaired electrons in the outer orbital shells (transition and lanthanide metals), giving rise to magnetic dipoles when exposed to a magnetic field. Since the magnetic moment of an electron is about 700 times larger than that of a proton (due to smaller mass), the paramagnetic ions induce large

fluctuating magnetic fields experienced by nearby protons. If the frequency of this fluctuation has components close to the Larmor frequency it will result in a significant enhancement of proton relaxation. There are many paramagnetic metal ions that could potentially be used as MR contrast agents, but the transition metal gadolinium (Gd^{3+}) is the most commonly used. This is due to a favourable combination of many (seven) unpaired electrons. But, due to the toxicity of heavy metal ions, the conventional contrast agents are in the form of ionic complexes with chelating ligands, which are thermodynamically and kinetically stable and less toxic. One of the most common chelates is Gd-DTPA (DTPA = diethylenetriamine pentaacetic acid), which is a clinically used contrast agent under the commercial name Magnevist®. In spite of their fewer unpaired electrons and lower magnetic moments, manganese(II), iron(III), and copper(II) ions could be alternative candidates (Na, Song, and Hyeon, 2009) .

1.2.3.2 T₂ Contrast agents

T₂ contrast agents work through shortening of T₂ relaxation time of protons located nearby. Magnetic nanoparticles based contrast agents serve as T₂ contrast agents. Under an applied magnetic field, induced magnetic spins in magnetic nanoparticles perturb the nuclear spin relaxation processes of protons of water molecules surrounding magnetic nanoparticles. This effect leads to the shortening of spin-spin relaxation time (T₂) of the proton due to inhomogeneities in local magnetic field and fluctuating magnetic fields at molecular level, which results in darkening of MR images, called as negative contrast agents. Iron oxide nanoparticles of different sizes have been developed as T₂ contrast agent for clinical applications on MR imaging.

They are referred to as superparamagnetic iron oxides (SPIO, mean size > 50 nm) and ultrasmall superparamagnetic iron oxides (USPIO, mean particle size < 50 nm). When materials with unpaired electrons are contained in a crystalline structure, they produce a stronger magnetic effect (susceptibility) in comparison with the independent molecules of a paramagnetic substance. The susceptibility of superparamagnetic materials is several orders of magnitude greater than that of paramagnetic materials. The superparamagnetic property of SPIONs is one of their most important characteristics for *in vivo* imaging applications, which only occurs when the individual particles are below 20nm in size. This property is absent in bulk iron oxide, which is a ferromagnetic (permanently magnetized) material (Guy and ffytche, 2005).

Superparamagnetism is similar to the paramagnetism exhibited by materials such as gadolinium; the material only shows a net magnetization when placed in an external magnetic field. However in contrast to paramagnetic materials, superparamagnetic materials retain zero net magnetization upon removal of the external field (i.e. they exhibit no hysteresis). The absence of any remnant magnetization significantly reduces the magnetic dipole-dipole interactions between SPIONs and thus helps to keep them from agglomerating. When a strong magnetic field is applied, however, SPIONs exhibit a stronger magnetic response than most paramagnetic materials, making them highly useful for imaging applications. The degree of MRI signal interference, and thus the contrast enhancement, provided by SPIONs is proportional to their saturation magnetization (M_s) value, the point at which all the individual magnetic moments in a sample are uniformly aligned. The various phase of iron oxide exhibit different M_s

values. Bulk magnetite has a higher M_s (92 emu/g at 300 K) than that of maghemite (76 emu/g) making the former a somewhat better choice for imaging applications. In practice, the M_s of SPIONs rarely reaches that of the bulk because it depends strongly on their size and morphology in addition to the manner in which they are synthesized. Variables such as reaction temperature, pH and reactant concentration all have an effect on the magnetic properties of SPIONs. Although iron oxide is considered non-toxic and is eventually metabolized by the body into hemoglobin, high doses of iron increases the probability of toxicity. Therefore, for *in vivo* work, it is important to use SPIONs with high saturation magnetization values at optimum concentrations to minimize iron loading. The particles produce inhomogeneities in the magnetic field, which results in rapid de-phasing of the protons in the transverse plane and a shortening of T_2 (Geraldes and Laurent, 2009).

1.3 Optical Imaging

Optical imaging is explicitly the most versatile and emerging visualization modality in clinical practice and research. Optical imaging which includes visible, ultraviolet and infrared could significantly reduce patient exposure to harmful radiation due to non-ionizing radiation. Optical techniques, such as bioluminescence and fluorescence, are emerging as powerful new modalities for molecular imaging in diagnosis and therapy. Fluorescence imaging has several advantages, including high sensitivity, low cost, noninvasiveness, lack of ionizing radiation, and multiplex detection capabilities. Most importantly, fluorescence signals can provide cellular and molecular information of biological tissues. In order to obtain high sensitivity and specificity of the

fluorescence signals *in vivo*, the important aspects to be taken care of are: (1) the photostability and biocompatibility of fluorescent probes; (2) the tissue penetration capability of excitation light source and emission light; (3) the distinction between target signal and background signal; and (4) the targeting ability of fluorescent probe to the desired tissue or organ (Luker *et al.*, 2008).

The optical imaging techniques offer high sensitivity, ie, the lower limits of picomolar or even femtomolar concentrations of an optical reporter or contrast agent is capable of producing signals for optical imaging. A major challenge for optical imaging probes and instrumentation, particularly in clinical applications, is the difficulty in overcoming attenuation and scattering of light by tissues. For light in the visible spectrum, absorption by hemoglobin and other molecules may reduce optical signals by approximately 10-fold per centimeter of tissue. To image fluorescence from deeper tissues, near-infrared fluorescence (NIRF) with emission wavelengths between 650 and 900 nm are suitable. At these wavelengths, absorption of light by hemoglobin, lipids, and water is lowest, and tissue autofluorescence also is greatly reduced. As a result, the sensitivity of NIRF imaging agents increases potentially allowing for tomographic optical imaging signals to be detected at depths of 7–14 cm (Montet *et al.*, 2005). Because it can obtain images of structures across a wide range of sizes and types, optical imaging can be combined with other imaging techniques, such as MRI or x-rays, to provide enhanced information for doctors monitoring complex diseases or researchers working on intricate experiments.

1.4 Nanotechnology and Imaging

Nanotechnology has emerged as a multidisciplinary research area undertaken at comprehending and molding materials by congregating concepts from the streams of engineering, chemistry, biology, medicine and others. Latest advances in technology in the generation of various types of nanoparticles clearly illustrates its importance in biological imaging applications (Ferrari, 2005). The ideas and concepts behind nanoscience and nanotechnology started with a talk entitled “There’s Plenty of Room at the Bottom” by the physicist Richard Feynman at an American Physical Society meeting at the California Institute of Technology (CalTech) in the year 1959, long before the term nanotechnology was used. In his talk, Feynman described a process in which scientists would be able to manipulate and control individual atoms and molecules. According to the National Nanotechnology Initiative (NNI), nanoparticles are particles having diameter ranging from 1 to 100 nm. Within the biomedical field, slightly larger particles are also often defined as nanoparticles as well, owing to a similarity in size to important naturally occurring structures such as viruses. At these dimensions, nanoparticles exhibit unique properties which vary distinctly from both molecules and bulk solids. Nanoparticles possess the ability to target tumors even without the aid of exogenous targeting ligands, passively through the enhanced permeability and retention effect (EPR), or specific tissues such as the lymphatic system through molecular sieving (Yin *et al.*, 2014). Apart from this, on conjugation with tumor targeting ligands (e.g., peptides, small organic molecules, antibodies, etc.), nanoparticles can be successfully used as tumor-specific probes with high specificity (Davis *et al.*, 2008). These development of molecular nanoprobe combined with the advancement in imaging

technology helps in the visualization of cellular function, characterization and the measurement of molecular processes in living organisms at the cellular and molecular level (Weissleder, 2006). At the nanometer scale, materials exhibit unique physical, chemical, magnetic and optical properties. As a result, synthesis methods which can control precisely the size and shape of nanoparticles to tune the magnetic and optical properties have been evolved. Parallely, surface modification or ‘biofunctionalization’ of nanoparticles has strengthened the high surface-to-volume ratio to enable multivalent ligand binding to target biomolecules and to make it biocompatible for *in vivo* applications (Nune *et al.*, 2009).

At present, a variety of nanoparticle systems are being investigated to explore their potential in molecular imaging, with many applications aimed at diagnosis or treatment of cancer (Lee and Chen, 2009). Particle charge, size, shape and hydrophilicity are the most important properties of nanoparticles for effective delivery to the desired target. For instance, a nanoparticle’s shape directly influences uptake into cells. Reports shows that rod shaped nanoparticles show the highest uptake, followed by spheres, cylinders, and cubes if the synthesized nanoparticles are larger than 100 nm. But, in studies with sub-100-nm nanoparticles, spheres show an appreciable advantage over rods (Albanese *et al.*, 2012). For intravenously administered nanoparticles, diameter is an important determinant of pharmacokinetics and biodistribution owing to the variable size of interendothelial pores lining the blood vessels. Nanoparticles with diameters smaller than 6 nm are quickly eliminated from the body because they can be excreted by the kidneys. Unless a nanomaterial consists of degradable materials such as

polymers, lipids, or hydrogels, it cannot be eliminated by the kidneys when the diameter is greater than 6 nm. Nanoparticles with diameters larger than 200 nm accumulate in the spleen and liver, where they are processed by the mononuclear phagocyte system cells. To produce long-circulating nanoparticles that can accumulate inside tumor tissues, a diameter between 30 nm and 200 nm is desired (Jain & Stylianopoulos, 2010). Regarding the surface charge of the surface modified nanoparticles, the internalization of negatively charged nanoparticles is believed to occur through nonspecific binding and clustering of the particles on cationic sites on the plasma membrane and their subsequent endocytosis. Positive nanoparticles are quickly adsorbed by serum proteins onto their surface that “tag” them for removal by the mononuclear phagocyte system. While for the neutral nanoparticles, any cellular uptake have been noticed (Verma *et al.*, 2009). Various types of nanoparticle are now under investigation, including solid lipid nanoparticles, liposomes, micelles, nanotubes, metallic nanoparticles, quantum dots, dendrimers, polymeric nanoparticles and iodinated nanoparticles. Of which for imaging, magnetic and fluorescing nanoparticles gather more attention due to the importance of MRI and optical imaging.

1.5 Biomedical application of Magnetic Nanoparticles

Magnetic nanoparticles (MNPs) gain great interest in research among wide range of disciplines, including industrial application, biotechnology/biomedicine, magnetic resonance imaging, cell separation, data storage and environmental remediation (Lu *et al.*, 2007). The biomedical application of MNPs ranges from contrast agents for magnetic resonance imaging to the destruction of cancer cells via

hyperthermia treatment. Most of these promising applications require distinct and convenient interactions between the MNPs and living cells. In many of the envisaged applications, the particles perform best when the core size of the nanoparticles is below a critical value, around 10–20 nm. At this particular size, each nanoparticles becomes a single magnetic domain and shows superparamagnetic behavior when the temperature is above the so-called blocking temperature. Such individual nanoparticles have a large constant magnetic moment with a fast response to applied magnetic fields with negligible remanence and coercivity. These features make superparamagnetic nanoparticles very attractive for a broad range of biomedical applications because the risk of forming agglomerates is negligible at room temperature. Furthermore, applications in biology like medical diagnosis and therapy requires the magnetic particles to be stable in water at neutral pH and physiological salinity.

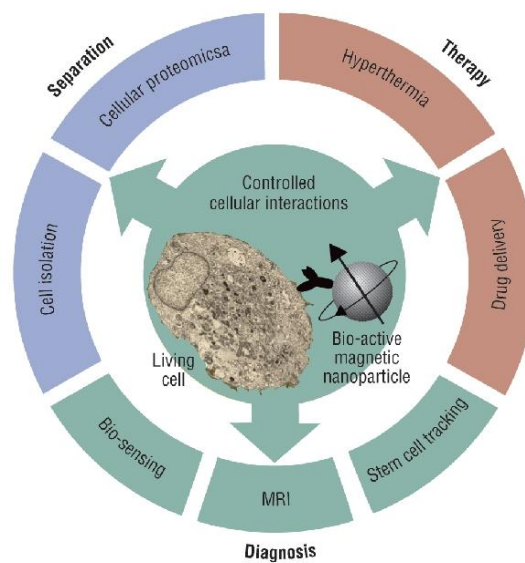


Figure-4. Biomedical applications of nanoparticles.

The various streams of biomedical use include diagnostic applications like contrast agent in MRI, biosensing and stem cell tracking (Figure-4). On interaction of MNPs with the protons of the tumor and normal tissue in a human body, there will be change in the relaxation rates of the protons which in turn results in the contrast difference on MR images. Cell separation or cell sorting are other applications. Cell separation or cell sorting involves the tagging or labeling of the desired biological entity with MNPs, and separating out of these tagged entities via a fluid-based magnetic separation device. These MNPs have proven its efficiency in the therapeutic applications, namely, hyperthermia and drug delivery. Hyperthermia involves dispersing MNPs throughout the target tissue, and then applying an AC magnetic field of sufficient strength and frequency to cause the particles to heat. This heat conducts into the immediately surrounding diseased tissue whereby, the cancer is destroyed if the temperature can be maintained above the therapeutic threshold of 42°C for 30 min or more. Drug delivery involves the incorporation of drug with MNPs and administered through any desired route to release the drug at the required tissue or organ where the release can be tuned by means of controlling the parameters like pH, time, photoresponsivity etc.

1.6 Fluorescent nanoprobes and its biomedical application

Conventional fluorophores such as fluorescent dyes, bioluminescent proteins and fluorescent proteins were used previously as contrast media for optical imaging. But they all are reported to be highly toxic, making them not suitable for biomedical applications. The recent advancements in the development of more biocompatible

fluorescent nanoprobes (FNPs) have made the technique a potential candidate for imaging-guided therapy. The desirable features of an optical contrast agent is it should be biocompatible, possesses a tolerable toxicity profile, small size, better fluorescence efficiency, high quantum yield, maintains photostability, pH insensitivity, has a low background signal with prominent contrast-to-noise enhancement, should not dilute with cell division nor transfer to other cells and enables long-term cell tracking. FNPs emitting in the visible range, imposes limitations for *in vivo* application as the autofluorescence from the body will hinder the actual desired signal. So NIR emitting FNPs are highly desirable for *in vivo* imaging or cell tracking. Cyanine dyes are found to be more efficient among NIR emitting dye for *in vivo* applications (Kircher *et al.*, 2003). Quantum dots (QDs), gold nanoclusters (AuCs), nanoparticles of diamond (DNP), carbon (CNP), and silica (SNP) have proven extremely useful in molecular imaging.

QDs are nanometer-sized, semiconductor crystals that offer superior photophysical properties over organic dyes including high quantum yields, broad excitation spectra, and narrow emission spectra and high photostability but presumably have limitations with respect to long-term biocompatibility (Smith *et al.*, 2008). AuCs have yielded highly luminescent structures with emissions ranging from 400 to 1200 nm. This NIR emission makes them suitable for optical spectral imaging of biological tissues, since tissue absorption at these wavelengths is limited. AuCs require an adequate protecting and stabilizing organic shell for their luminescence and display relatively narrow excitation and broad emission spectra with a quantum yield up to 40% (Lin *et al.*, 2009). DNPs possess efficient scattering properties, bright and photostable

fluorescence, low cytotoxicity, and chemical stability. Fluorescence spectra of these NPs show excitation maxima around 488, 532 and 633 nm and emission around 500–530 nm, 580–680 nm and 640–720 nm and the phenomena arises from so-called point defects which are initiated by high-energy irradiation (Chao *et al.*, 2007). The tunable luminescent properties of QDs also arises from the size dependent quantum confinement effects, develop when the thickness of an electronic layer approaches the de Broglie wavelength of the electron in a quantum well structure and when the radius of a semiconductor sphere is smaller than the bulk-exciton Bohr radius, in a nanocrystal (Bera *et al.*, 2010). Preliminary studies report DNPs as nontoxic *in vitro* as well as *in vivo* but lacks long term studies (Vlasov *et al.*, 2014). CNPs, include carbon nanotubes (CNTs) and carbon dots (or C-Dots), which are less cytotoxic when compared with QDs. CNTs and C-Dots holds photostability but display relatively broad emission spectra around 520 nm on excitation around 450 nm. Nonaggregated CNTs were found to exhibit an inherent NIR luminescence with a quantum yield not less than 10%. Long-term effects of CNPs on *in vitro* studies summarizes that the cell viability strongly depend on surface-stabilization, dosage and presence of traces of metal catalysts used during synthesis. Until now, few studies only have utilized CNPs for *in vivo* optical imaging (Luo *et al.*, 2013).

1.7 Liver Fibrosis

Cancer is one of the leading causes of disease associated death worldwide. The burden of cancer continues to increase globally due to the increase in the unhealthy lifestyle habits that promote this deadly disease. An accurate and early diagnosis is

necessary for the prophylaxis of such devastating diseases (Ali I, Wani A W. and Saleem K, 2011). Liver cancer is the fifth most frequently diagnosed cancer among men and seventh most commonly diagnosed cancer among women. Also it is the second and sixth most frequent cause of cancer death among men and women (Jemal *et al.*, 2011). Hepatitis virus infection and intake of intoxicants are the major causes behind this state of affair. Chronic alcoholism is one of the major reasons behind this devastating incidence of liver cancer in south India. Liver diseases associated with alcoholism are classified as fibrosis and cirrhosis depending on the degree of damage caused by alcohol. Among this, cirrhosis is the advanced stage and the most prevalent causes of alcohol related death (Mann, Smart & Govoni, 2003; Szabo & Mandrekar, 2010).

Hepatic architectural damage due to accumulation of extra cellular matrix proteins is the prime feature of most of the chronic liver diseases. Fatty liver is the earliest stage of liver damage which develops through fibrosis to cirrhosis and finally resulting in hepatocellular cancer (HCC). An efficient management of the disease is possible if diagnosed at the fibrosis stage which is curable where as on advancement of the condition to cirrhosis and HCC, the management becomes difficult or rather not possible. Liver fibrosis refers to the accumulation of tough, fibrous scar tissue in the liver preceded by an injury or necrosis of hepatocytes.

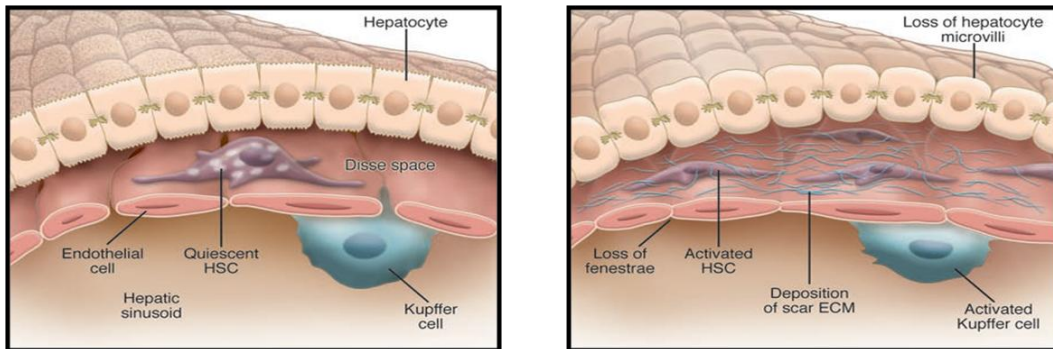


Figure-5. Schematic diagram of architecture of normal liver (left) and the fibrotic liver (right).

Once hepatocytes get injured due to infection with a virus, heavy alcohol consumption, toxins, trauma, or other factors, the immune system is activated to repair the damage. The injury or death (necrosis) of hepatocytes stimulates inflammatory immune cells to release cytokines, growth factors, and other chemicals. These chemical messengers direct support cells in the liver called hepatic stellate cells to activate and produce collagen, glycoproteins (such as fibronectin), proteoglycans, and other substances. These substances are deposited in the liver, causing the build-up of extracellular matrix (nonfunctional connective tissue). At the same time, the process of breaking down or degrading collagen is impaired. Fibrosis occurs when excessive scar tissue builds up faster than the speed at which it can be broken down and removed from the liver (Figure-5). In the early stages of fibrosis, the liver functions properly and very few patients experience symptoms. But as the inflammation and liver injury continue, scar tissue builds up and connects with existing scar tissue, which can eventually disrupt the metabolic functions of the liver. Progression of the disease can lead to cirrhosis, a

condition in which the liver is severely scarred at which its blood flow restricts, and its ability to function gets impaired (George J & Chadrasan G, 2000).

Diagnosing the disease at the fibrosis stage will help for a better management and to revert the diseased condition back to normal. The delivery of nanoparticles with magnetic and optical properties to the liver leads to the contrast variation of fibrosed area with the surrounding normal tissue and helps in the effective diagnosis. The NPs target to the exact organ or site through mechanisms related to either passive targeting or active targeting.

1.7.1 Passive Targeting of Liver abnormalities

Passive targeting is a strategy whereby the physicochemical properties of carrier systems increase the target/nontarget ratio of the quantity of drug delivered to the target tissues, organs, or cells. In this way, targeting of drugs would avoid side effects by preventing major distribution to a particular organ or cell type. Carriers included in this category are synthetic polymers, some natural polymers such as albumin, liposomes, micro (or nano) particles, and polymeric micelles. Chemical factors such as hydrophilicity and positive/negative charge and physical factors such as size and mass greatly influence the passive targeting efficiency. Along with this, passive targeting takes advantage of the size of nanoparticles and exploits the unique anatomical and pathological abnormalities of the tumor vasculature. Nanoparticles can extravasate and accumulate inside the interstitial space. This contributes to an “enhanced permeability”. Moreover, lymphatic vessels are absent or inactive in tumors, leading to inefficient drainage of the tumor tissue. This contributes to an “enhanced retention”. Together these

two phenomena constitute the “Enhanced Permeability and Retention” (EPR) effect (Albanese *et al.*, 2012). In the case of liver fibrosis, the normal architecture of liver collapse resulting in the increased formation of connective tissue and decreased lymphatic drainage which favours the passive targeting of the NPs.

1.7.2 Active Targeting of Liver abnormalities

Active targeting employs specific receptor interactions to increase the delivery of NPs to a target site where the contrast effect is required. The incorporation of a homing devices, or site-directed ligands, redirects the NPs to specific binding sites on cell membranes. These interactions include antigen-antibody and ligand-receptor binding. The homing devices can be carbohydrate ligands, functional groups bearing antibodies or other peptide ligands. These homing devices may be coupled to nanoparticles and delivered. In liver associated malignancies, over expression of asialoglycoprotein receptors occur which has got a carbohydrate recognition domain (Reimer *et al.*, 1991; Stefanescu *et al.*, 2011). The presence of this domain could be exploited in modifying the surface of the nanomaterials with carbohydrate polymers to enhance passive uptake. This receptor-mediated internalization has a major advantage of targeted nanoparticles in addition to the specific targeting of nanoparticles.

1.8 Hypothesis

The diagnosis of early fatty changes within the liver favours transverse relaxation T_2 over longitudinal relaxation T_1 due to low T_1 response of accumulated fat within liver than hepatocytes. Due to this reason, contrast agents with enhanced transverse relaxivity like surface modified superparamagnetic iron oxide nanoparticles (SPIONs) are

preferred for liver imaging over conventional gadolinium based contrast agents with longitudinal relaxation properties. There are many commercially available contrast agents which are classified as iron oxide based transverse contrast agents like Endorem, Resovist, Clariscan etc. Important application of these contrast agents are liver, lymph node and vascular MR imaging. Non-specificity is one of the major drawbacks of these blood pool contrast agents. Organ/site specific contrast enhancement is not possible while using these blood pool contrast agents. Moreover, most of these contrast materials have already been withdrawn from the market due to safety concerns. It is reported that most of these contrast agents used low molecular weight polymers for the surface modification, which has a tendency to cause osmotic nephropathy which leads to chronic renal failure. A similar problem has also been reported with the administration of gadolinium based contrast agents. For more accurate and efficient means of diagnosis, optical contrast moieties also can be incorporated leading to the multimodal imaging possibility using a single probe. Considering these factors, it is hypothesized that

- i. Tuning the size and magnetic properties of ironoxide NPs (USPIONS) can improve the imaging efficiency.
- ii. Surface modification of USPIONS with appropriate biopolymers will improve biocompatibility and reduce toxicity.
- iii. A combination of magnetic NPs with fluorescent materials will yield multimodal imaging efficacy.

- iv. Targeting the probes for Liver abnormalities will yield efficient system for early diagnosis.

1.9 Objective of the Study

Objectives of this study are defined as

1. Synthesize SPIONs with optimum size, magnetic properties and surface modification for targeted liver MRI.
2. Modify the SPIONs with fluorescent nanoprobe or dyes to develop multimodal (MRI & Optical) imaging contrast.
3. Demonstrate the potential of the developed probes for targeted liver imaging by *in vitro* and *in vivo* methods.

Chapter 2
REVIEW OF LITERATURE

2. REVIEW OF LITERATURE

2.1 Ironoxide nanoparticles

In the last few decades, nanoparticle research has achieved great advances in biomedical fields of diagnostic imaging and therapeutic applications. In particular, magnetic nanoparticles offer remarkable progress in important bio applications like magnetic bioseparation, diagnosis and therapy such as MRI and MFH (magnetic fluid hyperthermia), targeted drug delivery and biological labelling. Among the magnetic nanoparticles, iron oxide nanoparticles (ION) clutch vast application profile among biomedical needs. Investigations on the application of IONPs for *in vitro* diagnostic tests has started since 1950's (Gilchrist *et al.*, 1957). Studies on the size dependent variation in the property of IONs particularly in the range of about 3–20 nm in diameter is still progressing. Major reported IONs in medical application include maghemite, γ -Fe₂O₃, or magnetite, Fe₃O₄. Among these, magnetite is very appealing and its biocompatibility has already been proven (Mahmoudi *et al.*, 2011). The important phenomena of superparamagnetism contribute remarkably for the tremendous application of IONs in biomedical field. Quantum size effects and the large surface area of magnetic nanoparticles contribute for this superparamagnetic phenomena and quantum tunnelling of magnetization, because each particle can be considered as a single magnetic domain (Goya *et al.*, 2003). For the production of the desired shape, stability, biocompatibility and monodispersivity, the synthesis approaches have to be selected and modified accordingly. The most common methods of synthesis includes co-precipitation (Kotsmar

et al., 2010), thermal decomposition (Sun & Zeng, 2002), hydrothermal synthesis (Takami *et al.*, 2007), microemulsion (Husein & Nassaraat, 2008) and sonochemical (Sodipo *et al.*, 2013) synthetic route. In addition, these NPs can also be prepared by other methods such as electrochemical synthesis (Ibrahim *et al.*, 2009) and laser pyrolysis techniques (Morjan *et al.*, 2007). Of all the synthesis procedures, coprecipitation is the most convenient method and also gives high material yield. The size and shape of the synthesized IONs depends mainly on the type of precursors used (such as chlorides, sulfates, nitrates, perchlorates, etc.), the ferric and ferrous ions molar ratio, the reaction temperature, the pH value, ionic strength of the media, and other reaction parameters like stirring rate, dropping speed of basic solution etc (Wu *et al.*, 2008). For coprecipitation method, a 1:2 molar ratio of Fe^{2+} and Fe^{3+} chloride is used to synthesize magnetite which resulted in a precipitate in the presence of a base at pH 8–14 which is black in colour under anaerobic conditions. Since magnetite is very sensitive to oxidation, the reaction must be under N_2 atmosphere to protect the particles and to reduce the size (Gupta and Curtis, 2004 and Kim *et al.*, 2001). The presence or absence of oxygen could critically affect the physical and chemical properties of the IONPs to a greater extent; hence the formation of aggregates can be reduced by suitably coating IONPs. For the storage of nanoparticles in colloidal form, the stability of the colloid demands supreme importance. The stability depends on the surface stabilization of the nanoparticles using either polymers or inorganic materials or both. Polymeric coating materials can be classified into synthetic and natural. Polymers based on poly(vinylpyrrolidone) (PVP), poly(lactic-co-glycolic acid) (PLGA),

poly(ethyleneglycol) (PEG), poly(vinyl alcohol) (PVA), etc. are typical examples of synthetic polymeric systems (Lee *et al.*, 2008; Liu *et al.*, 2007; Zhiwei Li *et al.*, 2013; Mahmoudi *et al.*, 2009; Xue *et al.*, 2001). Natural polymers such as dextran, chitosan, pullulan, etc (Chung *et al.*, 2012; Saboktakin *et al.*, 2010, Yim *et al.*, 2011) also serve as important surface stabilizers with more biocompatibility. Other inorganic surface coatings include silica, gold etc which are also usually used to enhance dispersibility in an aqueous medium (Qianyun Li *et al.*, 2013; Leung *et al.*, 2012). These coatings provide both stability to the nanoparticles in solution and also helps in the binding process of various biological ligands to the nanoparticle surface for different biomedical applications. For introducing the targeting property to the IONs, various biological molecules such as antibodies, proteins, targeting ligands, etc., can also be bound to the polymer surfaces onto the nanoparticles by chemically coupling via amide or ester bonds (Xie *et al.*, 2011). The work reported by Xie *et al.*, shows the potential of Lactoferrin conjugated SPIONs in targeting the glioma site of brain thereby recommending the same for the diagnosis of Alzheimer's disease and other carcinogenic tumors. The application of IONs depends mainly on the magnetic properties of nanoparticles which in turn depend upon their physical structure, the size and shape of the particles.

One of the most important applications of magnetic nanoparticles is in drug delivery as drug carriers, which is proposed in the 1970s by Widder *et al.* (Lu *et al.*, 2007) The application of polyethyleneimine (PEI)-modified magnetic nanoparticles as a potential vascular drug/gene carrier to brain tumors using magnetic targeting and

intra-carotid administration has been studied extensively by Chertok *et al* (Chertok *et al.*, 2010). The effective *in vivo* brain accumulation of nanoparticles by magnetic targeting was studied in rats by harboring 9L glioma by Chertok and group utilizing the pathophysiology of the tumor site (Chertok *et al.*, 2008). Many research groups still works with the aim to improve the efficiency of the targeting to the recommended site and to overcome difficulties associated with conventional free anticancer drugs, including insolubility under aqueous conditions, rapid clearance, lack of selectivity resulting in nonspecific toxicity toward normal cells and to lower the dose of drugs delivered to the cancer cells (Laurent *et al.*, 2008). Another interesting application of IONs is its therapeutic application, hyperthermia, which is considered as an alternative treatment to chemotherapy, radiotherapy, and surgery in cancer treatment. The hyperthermia works on the principle of rise in the temperature of a region of the body affected by malignancy or other growths to above 41–42°C ie, a direct cell-killing effect. The physical principle behind hyperthermia is that when magnetic nanoparticles are exposed to a varying magnetic field, heat is generated by the magnetic hysteresis loss, Neel-relaxation, and Brown-relaxation (Tartaj *et al.*, 2003). The hyperthermia effect of pullulan acetate coated IONs were demonstrated through *in vitro* studies by Gao and group (Gao *et al.*, 2010). The *in vivo* studies of biomagnetic hydroxyapatite nanoparticles carried out by Hou and group showed significant and fast therapeutic effect of murine colon cancer within 2 weeks (Hou *et al.*, 2009). Another important *in vitro* application of IONs is the functionalization for protein for cell separation. Magnetic separation techniques is very simple, and all steps of the purification can take place in one test tube

which is advantageous over traditional separation procedures. Li *et al* have demonstrated that anti-BSA antibody-covered carboxy methylated dextran coated IONPs possess good selectivity and are able to capture protein antigens from real samples (Li *et al.*, 2011). The most promising applications of targeted IONs remain as the molecular imaging based on the technique of MRI. Lots of studies using IONs have been evaluated *in vitro* and in animal experiments.

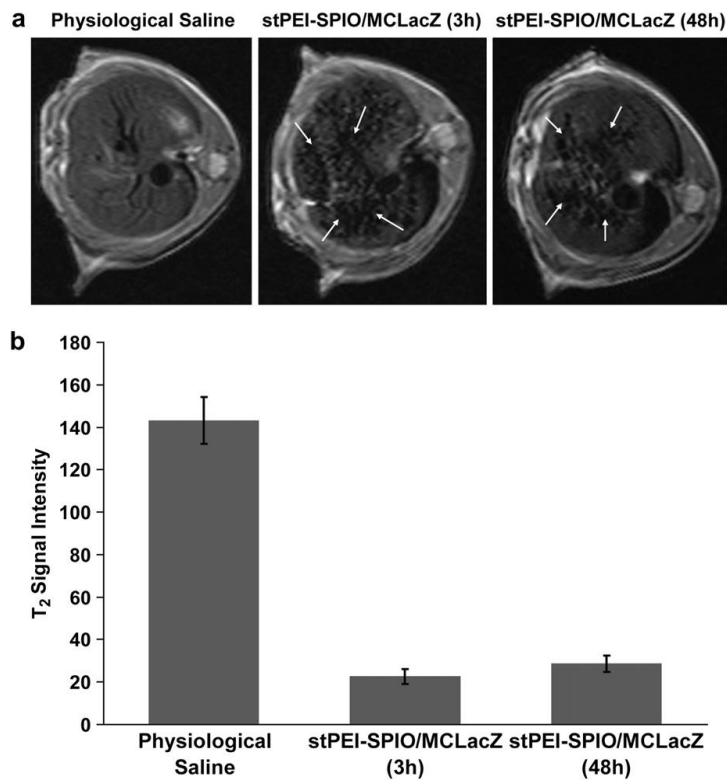


Figure - 6. (a) T₂-weighted images of livers after the stPEI-SPIO/MCLacZ nanocomplex injection at 3 h and 48 h. Herein, the mice injected with physiological saline have been used as the control groups (TR = 3000 ms, TE = 48 ms). (b) Signal intensity quantification of T₂-weighted images (Gao *et al.*, 2011).

The study contributed by Gao *et al* provides the efficacy of MRI visible IONs in delivering minicircle DNA into liver via intrabiliary infusion. The group constructed the

nanoparticle via self-assembly of stearic acid modified low molecular polyethyleneimine (stPEI) and superparamagnetic iron oxide (SPIO) nanocrystals. Furthermore, the MCDNA was combined with the nanoparticles via electronic interaction. Through intrabiliary infusion, the stPEI-SPIO/MCDNA nanoparticles were efficiently delivered to liver that was visualized by MRI *in vivo* (Figure - 6) and confirmed by histology (Gao *et al.*, 2011). The *in vivo* detection of early stage of liverfibrosis have been extensively studied and reported by our group with dextran and citrate stabilized IONs (Saraswathy^a *et al.*, 2014 ; Saraswathy^b *et al.*, 2014). Muller and co-workers (Laurent *et al.*, 2008) comprehensively reviewed all the major applications of superparamagnetic iron oxide NPs as a contrast agent. Kim *et al.* synthesized starch coated IONs for MRI contrast agents. The MRI results imply that for MR imaging with starch-coated SPION, both the image intensity and contrast might be severely amended by the existence of SPION. The synthesized starch-coated SPION in buffered artificial cerebro-spinal fluid was injected into the brain parenchyma of anaesthetized rats for *in vivo* monitoring. The T2*-weighted images and T2*-maps revealed formation of a concentration gradient for the SPION at the injection site, indicating SPION dispersion in the living brain parenchyma from the center of the injection site toward the periphery (Kim *et al.*, 2003). Very small sized IONs possessed T₁ weighted MR relaxivity due to the spin canting effect. Uniform and extremely small-sized iron oxide nanoparticles (ESIONs) with diameters of the order of 4 nm or less were synthesized by controlled thermal decomposition of iron-oleate complex via heat-up process by Kim and group. The as synthesized 3 nm-sized nanoparticles exhibited a high r₁ relaxivity of 4.78 mM⁻¹

s^{-1} and low r_2/r_1 ratio of 6.12, demonstrating that ESIONs can be efficient T_1 contrast agents. The high r_1 relaxivities of ESIONs can be attributed to the large number of surface Fe^{3+} ions with 5 unpaired valence electrons (Kim *et al.*, 2011). Recently MRI tracking of stem cells have gained much importance and effectiveness. In the study carried out by Qin and group, IONs coated with meso-2,3-dimercaptosuccinic acid (DMSA) were synthesized. The particles were shown to exhibit a considerable potential for use as nanoprobes for MRI of stem cells enhancing the understanding of cell-based therapeutic strategies for ischemic diseases. The study reflected that for MR imaging, the DMSA-IONs labelled Green Fluorescent Protein expressing Adipose-derived stem cells can be sensitively monitored in the T_2 -weighted images, and the signal intensity persists over an extended period until the cells completely vanish at week 8 (Qin *et al.*, 2013).

2.2 Gold nano clusters

Gold nanoclusters attract a capital of interest in many areas of nanotechnology. Gold nanoparticles show a size-dependent plasmon absorption band when their conduction electrons in both the ground and excited states are confined to dimensions smaller than the electron mean free path (ca. 20 nm), but plasmon absorption disappears completely for nanoparticles less than 2 nm when Mie's theory can no longer be applied (Chevrier D M, Amares Chatt, and Peng Zhang, 2012). These sub-nanometer particles demonstrate molecular-like electronic transitions between highest occupied molecular orbital and lowest unoccupied molecular orbital (HOMO- LUMO) energy levels, due to their finite cluster size. This unique electronic nature of gold nanoclusters

causes for the photoluminescent properties. The synthesis procedure of nanoclusters can be of two routes, the template-based synthesis and monolayer-protected nanoclusters (MPCs) synthesis. Template synthetic strategies include electrochemical and electroless depositions, chemical polymerization, sol-gel deposition, and chemical vapour deposition. MPCs synthesis research was started by Brust and co-worker in 1994 (Brust *et al.*, 1994) , which includes the synthesis of noble metal clusters (Au, Ag, etc.) protected by ligands, such as thiolates (Shichibu *et al.*, 2007), phosphines (Shen *et al.*, 2014) and amines (Jin *et al.*, 2014). Tsukuda *et al.* showed that among the various glutathione protected QCs, Au₂₅ is the most thermodynamically stable and larger analogues can be converted to Au₂₅ by adding excess glutathione (Shichibu *et al.*, 2007). The same group also electrophoretically isolated a series of magic-numbered clusters, Au₁₈(SG)₁₁, Au₂₁(SG)₁₂, Au₂₅(1(SG))₁₄, Au₂₈(SG)₁₆, Au₃₂(SG)₁₈, and Au₃₉(SG)₂₃ (Negishi *et al.*, 2004). The size and temperature dependence of the plasmon absorption is studied for 9, 15, 22, 48, and 99 nm gold nanoparticles in aqueous solution by El-Sayed and group (Link *et al.*, 1999). Several studies starting from the important optical and photothermal properties of gold nanoparticles in different shapes and structures and to their recent applications for cancer imaging, spectroscopic detection and photothermal therapy have been reported by El Sayed *et al* (Huang *et al.*, 2010). Protein-stabilized Au NCs are being recognized with wide application and for their strong fluorescence. Au NCs experimenting with BSA was a perfect opening to study protein-Au NC systems which was ignited by Xie *et al.* by using BSA (Xie *et al.*, 2009). They introduced a facile protein directed synthesis which has been followed by

several other groups for other protein-Au NC systems (Durgadas *et al.*, 2011). The system shows red emission around 640 nm with quantum yields reported as high as 6% and have the intracellular sensing application. The Au-BSA clusters prepared for the detection of Cu^{2+} by Durgadas and group demonstrates the efficient Cu^{2+} selectivity from 50 μM to 5 mM concentration intracellularly. The interaction of Au-BSA clusters quenches the fluorescence linearly with increasing Cu^{2+} concentration. It has also been shown that BSA-Au NCs can detect other metals such as Hg^{2+} (Hu *et al.*, 2010). Another study by Söptei *et al* have shown the interactions between BSA coated Au clusters and cell membrane-mimetic phospholipid bilayers successfully. The study also includes the point that the changes in emission characteristics of the embedded Au clusters offer a way to develop 'local sensor quantum clusters' to indicate the alterations in the physico-chemical behavior of surrounding medium (Söptei *et al.*, 2014). Liu and group demonstrated BSA-Au-NC-based fluorescent sensor for highly sensitive and selective detection of cyanide in aqueous solution, which was based upon the cyanide etching triggered fluorescence quenching of the Au NCs (Liu *et al.*, 2010). Zheng *et al* developed highly fluorescent, water-soluble Au quantum dots from poly(amidoamine) dendrimers (PAMAM) encapsulated Au that behave as multielectron artificial atoms with size-tunable, discrete electronic transitions throughout the visible and near IR range (Zheng *et al.*, 2004). Zhou and group developed folic acid conjugated silica coated AuNCs nanoprobe which has a uniform sphere shape and size distribution. These studies used Au NCs as an imaging probe for detection of folate receptors on oral carcinoma cells with an emission profile extending into the near-IR, suitable for tissue

penetration (Zhou *et al.*, 2013). Pradeep and his group synthesized luminescent gold clusters using a therapeutically important protein, transferrin, which can target *in vivo* gastric cancer cells (Xavier *et al.*, 2013). Jayasree *et al.*, developed NIR emitting glutathione gold cluster and demonstrated its use in the sensing application of urea directly from the whole blood which is an advantage over the existing clinical methods and industry. The group also demonstrated the generality of the nanosensor in detecting urea in adulterated milk samples (Lakshmi *et al.*, 2013). Eventhough many studies demonstrated cellular studies which showed good biocompatibility, no studies till now reports on *in vivo* studies of gold cluster-SPION hybrid complex.

2.3 Carbon nanodots

Luminescent carbon nanodots have emerged as a hopeful beginning showing high potential in the optical imaging and sensing in the biomedical field. The chemical inertness and biocompatibility make the C-Dots more preferable than the conventional quantum dots. Carbon nanomaterials includes carbon nanoparticles, carbon nanotubes and Carbon nanodots (C-dots) of which, C-dots fall under the category of nanoparticle of size below 10 nm which was reported to be first obtained during purification of single-walled carbon nanotubes through preparative electrophoresis in 2004 (Xu *et al.*, 2004). C-Dots are conjugated systems consisting of sp^2 and sp^3 hybridized carbons atoms with plenty of oxygen- containing groups. C-dots offer excellent photostability, favourable biocompatibility, low toxicity, high water solubility, high sensitivity and selectivity to target analytes, tunable fluorescence emission and excitation, high quantum yield (QY) and large Stokes shifts (Yang *et al.*, 2013). Synthesis routes of C-

dots include laser ablation (Sun *et al.*, 2006), electrochemical oxidation (Zhou *et al.*, 2007) and combustion/thermal microwave heating (Wang *et al.*, 2011). Considering the ease of synthesis and easy operating steps, hydrothermal, solvothermal, and microwave synthesis methods are getting popularized. Zhu *et al.* synthesized C-Dots by the hydrothermal treatment of citric acid and ethylenediamine which yielded the highest quantum yield of up to 80%. The highest value is almost equal to that of fluorescent dyes. The reaction includes ionization, condensation, polymerization, and carbonization by bottom-up method (Zhu *et al.*, 2013). Microwave synthesis methods can be carried out by exploiting a domestic microwave oven with less reaction time needed. Many works have been reported by microwave methods in recent years. Qu *et al.* reported the development of excitation wavelength-dependent C-Dots by using citric acid and urea in 700 W for 4 to 5 min. These synthesized C-Dots can emit light in dry and aggregate states. They can be coated on commercial gauzes, vegetable fibers, animal furs, feathers, and skins as fluorescent ink. These large-scale synthesizable C-Dots can be applied in information encryption and information storage (Qu *et al.*, 2011) applications. Wang and group developed a general and simple microwave synthesis method to produce multicolour photoluminescent carbon dots, which are biologically compatible with favourable optical properties. All these properties recommend the C-Dots as a promising imaging agent in biomedical applications (Wang *et al.*, 2011). Unfortunately, the majority of the reported C-Dots shows blue fluorescence which is not advisable for *in vivo* imaging. So for *in vivo* applications, the synthesis conditions have to be modified.

Zhu and group synthesized the bifunctional nitrogen-doped C-Dots via hydrothermal treatment of soy milk for the first time. These C-Dots not only showed favourable PL properties, but also exhibited good electrocatalytic behavior towards oxygen reduction rate. Along with this green and cost effective protocol of synthesis, the authors expect that these novel carbon nanodots have potential applications in bioimaging and electrocatalysis (Zhu *et al.*, 2012). Goh *et al* synthesized C-Dots of particle size in the range 5-7 nm by the pyrolysis of citric acid in the presence of PEG diamine and is then conjugated with hyaluronic acid. They compared the *in vivo* real-time bioimaging of C-Dots and HA-Cdot conjugates which revealed the target-specific delivery of HA-Cdot conjugates to the liver with HA receptors such as Cluster determinant 44 (CD44), lymphatic vessel endothelial hyaluronan receptor (LYVE)-1, and HA receptor for endocytosis (HARE), reflecting the feasibility of HA derivatives as a drug delivery carrier for the treatment of liver diseases and Cdots as a promising bioimaging agent (Goh *et al.*, 2012). Zhou *et al* demonstrated a simple and green approach to synthesis of amphibious C-Dots from peach gum polysaccharide. The CDs exhibit excellent solubility and strong photoluminescence both in water and in organic solvents (Zhou *et al.*, 2013). Another study by Yu *et al* demonstrated C-Dots to form a FRET system with an organic dye which serve as a ratiometric sensor for H₂S in aqueous solution, biological fluids and in living cells with high selectivity and a very low detection limit. Due to the biocompatible nature and small size of the synthesized C-dots, the sensor can easily permeate through the cell membrane and trace the intracellular H₂S level change. The demonstrated strategy may provide a new approach

for constructing FRET-based ratiometric systems for detecting analytes in aqueous media and inside live cells (Yu *et al.*, 2013). Castilo *et al* synthesized C-Dots with down and upconversion luminescence properties for selective and sensitive detection of Cu^{2+} (Castilo *et al.*, 2013).

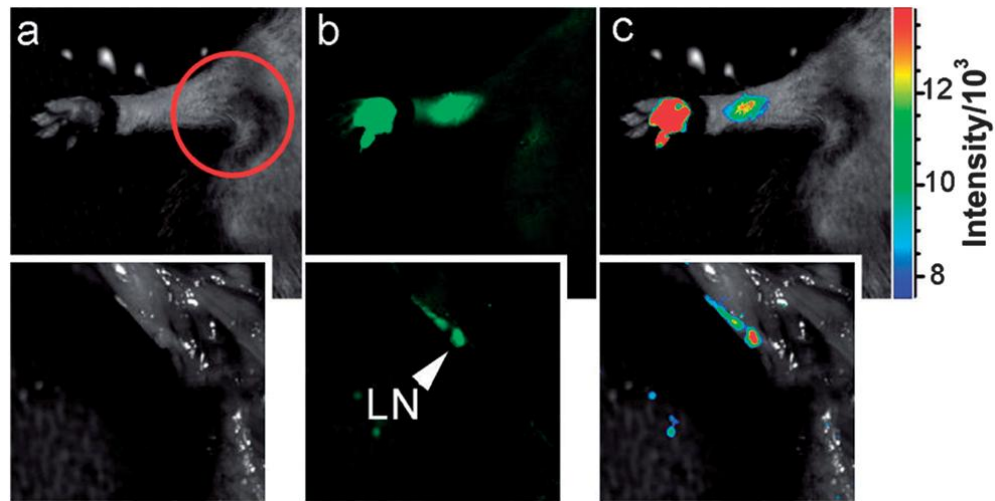


Figure-7. Fluorescence imaging in mice with interdermal injection of the carbon dots: (a) bright field and (b) as-detected fluorescence and (c) colour-coded images. Insets: images on the dissected (in the circled area) axillary lymph node (LN) (Yang *et al.*)

Yang *et al.* were the first to explore the feasibility of C-dots as a fluorescence contrast agent in mice. PEGylated carbon dots in an aqueous solution were injected subcutaneously, intradermally and intravenously into mice, and the fluorescence images at different excitation wavelengths were collected. For the sentinel lymph node imaging, the PEGylated C-dots were injected intradermally into the front extremity, and fluorescence images at 470 nm excitation were collected continuously. Following the injection, carbon dots migrated along the arm to the axillary lymph node (sentinel lymph node, Figure - 7). The observed migration of the carbon dots was slower in comparison

with that of the semiconductor QDs, probably due to the smaller sizes of the carbon dots (around 5 nm) and/or the surface PEG functionalization. The axillary lymph nodes were harvested and dissected at 24 h post-injection, and the fluorescence from the carbon dots could readily be detected in the specimen (Figure - 8).

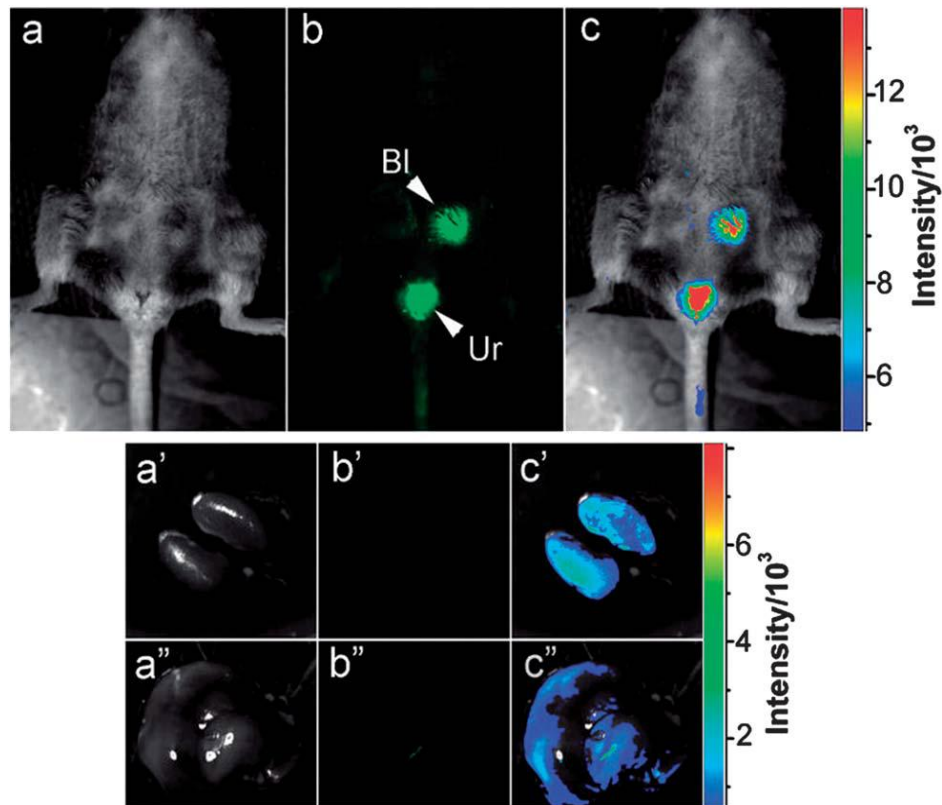


Figure – 8. Fluorescence imaging in mice with intravenous injection of the carbon dots: (a) bright field, (b) as-detected fluorescence and (c) colour-coded images. Insets: the corresponding images on the dissected kidneys (a'–c') and liver (a''–c'') (Yang *et al.*) The iv administration yielded signals from the bladder area on *in vivo* imaging, but signals were present in the dissected kidneys and liver on harvesting organs after 4 hrs of administration (Yang *et al.*, 2009). Recently, Tao *et al.* applied the same protocol to nude mice and obtained similar results. In this experiment, an aqueous solution of

carbon dots was injected subcutaneously into the mice, followed by *in vivo* fluorescence imaging with excitations at seven different wavelengths from 455 nm to 704 nm. The best fluorescence contrast was found at 595 nm excitation (Tao *et al.*, 2012). Another study by Cao *et al.* made a direct comparison between carbon dots and commercially available CdSe–ZnS QDs for fluorescence imaging in mice. The carbon dots were harvested from the commercially supplied carbon nano-powders for relatively higher fluorescence quantum yields, about 60% at 440 nm excitation. The subcutaneous and intradermal lymph node *in vivo* imaging in mice provided comparable performance of the carbon dots to that of the presently dominating semiconductor QDs for *in vivo* fluorescence imaging in the specific visible wavelength region (Cao *et al.*, 2012). Ko *et al.* prepared and isolated fluorescent C-dots from tire soot (tC-dots) by means of an oxidative acid treatment with nitric acid and demonstrated NIRF properties of the tC-dots using C6 (a rat glioma cell line) cells *in vitro* and *in vivo*. The C6 cells with and without incubation with the tC-dots were subcutaneously implanted into the right and the left thigh of a nude mice, respectively. The *in vivo* imaging of the tC-dots at NIR emission wavelengths including 660, 700, 740 and 800 nm showed a sensitive fluorescence activity from the left thigh with a significant decrease in tissue autofluorescence background (Ko *et al.*, 2013). The assessment of C-dots *in vivo* has only had a good launch, with much remaining to be explored. However, we can conclude with very few reported works that the *in vivo* imaging efficiency C-dots give hope for a transformation of a new era replacing QDs. The modification in the synthesis criteria for yielding NIR emitting C-dots will become a better candidate for optical

imaging contrast agent. Further investigations on application potentials by coupling with targeting moieties and by combining with magnetic NPs can utilize the total competence of C-dots in cancer diagnostics and angiography (Tao *et al.*, 2012).

2.4 Hybrid Nanoparticles

An important outlook advent in the research direction in nanoparticle synthesis is the integration of single-component nanoparticles to multicomponent hybrid nanostructures with distinct domains of diverse materials set in a regular and controlled fashion. The advantages of hybrid structures stretch out in realizing the multifunctionality, integrating different functionalities and with the dimension and material parameters of the individual components independently optimized (Zeng H and Sun S). Hybrid nanoparticles can be considered as the assembling of two or more distinct nanoparticles in a functional structure, together they still remain in the nanoscale dimensions. The main aim of the formation of hybrid nanosystem is to design a nanostructure whose medical effects are superior to those that could be comprehended from any of the individual components. Mainly, hybrid nanoparticles are expected to be those that contain both therapeutic and diagnostic nanocomponents. The incorporation of both the entities in a nanoparticles are reported to be of two ways, ie either it is fixed to the surface of another nanoparticle, or it is encapsulated in a porous nanostructure (Sailor M J. and Park Ji-Ho, 2012). The properties of hybrid nanoparticles were not simply resulting from the sum of the individual contributions of the entities , but also from the strong synergy created by an extensive hybrid interface. Indeed, the mineral/organic interface present in the hybrid system, including the types of

interactions present, the surface energy, and the existence of labile bonds, plays a strong role in modulation of a number of properties like optical, magnetic, mechanical, and chemical and thermal stability(Nicole *et al.*, 2010). Kim and group reported Co/CdSe bifunctional magneto-optic nanocrystals, in which the core/shell nanoparticles retain the magnetic and optical properties of each single component and permit potential applications as optical reporters and magnetic handles for bioassay. Since the dimensions of the individual components are comparable to the size of the biomolecules, the combination is expected to provide improved performance (Kim *et al.*, 2005; Bishnu P. Joshi 1 and Thomas D. Wang, 2010).

Multicomponent hybrid nanoparticles are commonly synthesized by sequential growth of a second and third component on the preformed seeds, categorized as seed-mediated growth (Zeng H and Sun S, 2008). The successful synthesis of multicomponent nanoparticles relies critically on promoting heterogeneous nucleation while suppressing homogeneous nucleation. Other core/shell nanoparticles with a variety of material combinations have also been realized by similar approaches. Teng *et al.* reported the synthesis of metallic/magnetic Pt/Fe₂O₃ nanoparticles by sequential decomposition of Pt(acac)₂ and Fe(CO)₅ (Teng *et al.*, 2002). Shi *et al* demonstrated a general strategy for engineering binary and ternary hybrid nanoparticles based on spontaneous epitaxial nucleation and growth of a second and third component onto seeded nanoparticles in high-temperature organic solutions. Multifunctional hybrid nanoparticles that combine magnetic, plasmonic, and semiconducting properties and that are tunable in size and morphology can be realized, as demonstrated for combinations of

Au, Fe₃O₄, and PbS or PbSe, such as Au/Fe₃O₄, semiconducting/metallic, such as Au/PbS, Au/PbSe, and Au/CdS, and magnetic/semiconducting, such as PbS/Fe₃O₄ (Shi *et al.*, 2006). Xu *et al* presented biocompatible Au-Fe₃O₄ nanoparticles suitable for A431 cell (human epithelial carcinoma cell line) attachment. The developed particles were found to be magnetically and optically active. The hybrid nanoparticles shorten the T₂ relaxation time of protons, and therefore can be used as magnetic resonance imaging (MRI) contrast enhancement agents. The T₂ relaxivity r₂ of the 8-20 nm Au-Fe₃O₄ nanoparticles around A431 cells is 80.4 mM⁻¹s⁻¹. Along with this, Au-Fe₃O₄ nanoparticles also show strong reflectance at 590-650 nm and A431 cells labeled with these particles can be imaged using a scanning confocal microscope with an optical detection limit upto 90 pM Au. The results indicated that the Au-Fe₃O₄ nanoparticles are promising materials as a new type of multifunctional probe for diagnostic and therapeutic applications. The group also recommends that through proper surface functionalization, the new dumbbell Au-Fe₃O₄ nanoparticles can be made biocompatible and suitable for linking different functional molecules to each end of the structure. On comparison, the EGFR-conjugated dumbbell nanoparticles show higher specificity in their attachment to A431 cells than those without EGFR (Xu *et al.*, 2008). Wu *et al* reported a class of core-shell structured hybrid nanogels to demonstrate the conception of integrating the functional building blocks into a single nanoparticle system for simultaneously optical temperature sensing, cancer cell targeting, fluorescence imaging, and combined chemo-photothermal treatment. They successfully developed a class of multifunctional hybrid nanogels (<100 nm) by coating the Ag-Au

NPs (10-3 nm) with the thermo-responsive gel shell based on the nonlinear PEG oligomers for integration of optical temperature sensing, tumor cell targeting and imaging, and thermo-/photothermal- regulated drug delivery. The resulted Ag-Au@PEG-HA hybrid nanogels have strong fluorescence for combined sensing on the temperature change and could overcome cellular barriers to enter the intracellular region and light up the mouse melanoma B16F10 cells. Along with this the hybrid nanogels offered high loading capacity for a model anticancer drug TMZ, and also offer a thermo-triggered release of the drug molecules in the gel network (Wu *et al.*, 2010). Hybrid nanomaterials possessing both fluorescent and magnetic properties may be used in various biomedical applications in nanobiotechnology, such as bioimaging, bio- and chemo-sensing, cell tracking and sorting, bioseparation, drug delivery and therapy systems in nanomedicine (Corr *et al.*, 2008). Lu and group prepared silica encapsulated commercial ferrofluid (EMG 304, Ferrofluids) with controlled coating thickness of the silica shell between 2 and 100 nm by changing the concentration of the tetraethyl orthosilicate (TEOS) precursor. The authors inferred the increase in the particle monodispersity with the thickness of the silica coating. The 7-(dimethylamino)-4-methylcoumarin-3-isothiocyanate and tetramethylrhodamine-5-isothiocyanate dye has been incorporated into the silica shell and magnetic-fluorescent nanocomposite materials have been prepared. Along with this, the organic dyes are incorporated during the coating process—in effect, the dye is trapped in the silica shell. The isothiocyanate functionality present on the dye moieties has been coupled to 3-aminopropyltriethoxysilane, which can be subsequently co-hydrolysed in the presence

of TEOS during the formation of the silica shell coating the magnetic cores. In addition to their uses as dispersions in liquid media, the work demonstrated the application of these magnetic particles with relatively thick shells as building blocks to construct photonic crystals whose band gap properties could be manipulated using an external magnetic field (Lu *et al.*, 2002). Another study by Lu *et al* developed up-converting fluorescent magnetic nanoparticles with covalently bound streptavidin using ytterbium and erbium co-doped sodium yttrium fluoride (NaYF₄:Yb, Er), which was deposited on iron oxide nanoparticles by the co-precipitation of the rare-earth metal salts in the presence of a chelator, EDTA [28]. A layer of silica was coated on the magnetic-fluorescent nanoparticles before being covalently coupled to streptavidin. These core-shell nanoparticles possess a silica coating of 20–30 nm, containing up-converting phosphors, on exciting at 980-nm, emit up-conversion fluorescence at 539 and 658 nm. The magnetic property of these hybrid particles were visualized with a stack in chain-like assemblies when subjected to an external magnetic field. The multi-functionality of the nanoparticles was demonstrated by VSM, fluorescence spectroscopy, fluorescence microscopy and bio-affinity reaction. The protein arrays revealed the successful surface immobilization of streptavidin. The authors conclude the report stating streptavidin-coated fluorescent magnetic nanoparticles can be used for immobilization of biotinylated biomolecules and subsequent capture of target molecules in samples (Lu *et al.*, 2004). Electrostatic interactions have also been utilised in order to provide new fluorescent-magnetic nanocomposites. The interactions among the core nanoparticle, the spacer group and the fluorophore have been employed to prepare new fluorescent

magnetite-porphyrin nanocomposites (Corr *et al.*, 2006). Herdt and group synthesized “magnetomicelles” by coating hydrophobic magnetic nanoparticles with an amphiphilic polystyrene₂₅₀-block-poly(acrylic acid)₁₃ block copolymer. PAA outer block provided water solubility to the composite and by ensuring only 50% of the surfactant is cross-linked, further functionalization also had been made possible through the attachment to the remaining carboxylic acid groups present. Immobilised metal affinity chromatographic technique was employed for the bioconjugation. Bertorelle and group described the preparation and characterization of new magnetic fluorescent nanoparticles with a magnetic oxide core composed of a dimercaptosuccinic acid (DMSA) ligand at the surface and a covalently attached fluorescent dye to label living cells. The fluorescence intensity of magnetic-fluorescent nanocomposites using fluorescein and rhodamine has found to be respectively 3.5 and 2 times lower than the dyes alone (Bertorelle *et al.*, 2006).

Das *et al* introduced a novel, inexpensive biofunctionalization approach to develop a multimodal and theranostic nanoagent, which combines cancer-targeted magnetic resonance/optical imaging and pH-sensitive drug release into one system. This multifunctional nanosystem, consist of an ultrasmall superparamagnetic iron oxide (USPIO) nanocore, modified with a hydrophilic, biocompatible, and biodegradable coating of N-phosphonomethyl iminodiacetic acid (PMIDA), along with appropriate spacers and functional molecules such as rhodamine B isothiocyanate, folic acid, and methotrexate coupled to the amine-derivatized USPIO–PMIDA support with the aim of endowing simultaneous targeting, imaging, and intracellular drug-delivering capability

(Das *et al.*, 2009). Taylor and group systematically studied the effects of different acid treatments on the dissolution of the core metal and surface properties of carbon-encapsulated iron nanoparticles. Carboxylated FeNP was effectively conjugated with molecules containing amine groups with reactions based on diimide-activated amidation, opening the possibility for conjugation of biomolecules with FeNPs making them more attractive for biomedical applications (Taylor *et al.*, 2010). Bae *et al* synthesized highly water-dispersible carbon-coated iron oxide nanoparticles for use as contrast agents in MRI by coprecipitation and hydrothermal method. The T_1 and T_2 relaxivities of hydrogen protons of the 90 nm sized hybrid probe measured using an MRI scanner in the aqueous solutions of various concentrations of nanoparticles ranging from 0.427 to 4.27 mM were 1.139 and 1.115 (mM·s)⁻¹, respectively showing the suitability of carbon-coated iron oxide nanoparticles as both T_1 and T_2 contrast agents in MRI (Bae *et al.*, 2012). Cha *et al* developed a fabrication method of Cy5.5-MMP substrate and PEG conjugated iron oxide nanoparticles with thin silica coating (PCM-CS) and its potential as an ‘activatable’ dual imaging probe for tumor imaging is described in the report. The *in vivo* MR imaging resulted in noticeable darkening of the tumor region with a maximum signal difference between tumor region and healthy muscle of 34% (Cha *et al.*, 2011). Another study by Jenkins and group evaluated the organ clearance and toxicity of gold-iron nanorose nanoparticles *in vivo* for the first time. The gold content of 11 murine tissues were found to decrease significantly in 31 days following i.v. nanorose injection, and this excretion was more efficient and rapid than other gold nanoparticles of comparable size in the literature, The authors claims

that the nanorose can be degraded via acid digestion in macrophages into subunits which could be excreted through renal and/or hepatobiliary mechanisms. This biodegradability, along with the absence of toxicity detected up to 14 days post injection, recommended the nanocluster design of nanorose a promising strategy for avoiding the problems associated with the long-term retention of gold nanoparticles (Jenkins *et al.*, 2013). Mu *et al* synthesized polymer grafted Fe@CNPs that have potential applications in magnetic resonance imaging (MRI), magnetic hyperthermia and drug delivery. In the study they prepared and modified pristine Fe@CNPs with different surface functionalities to make Fe@CNPs possess negative (acid), positive(amine), zwitterionic (vinyl pyrrolidone), and neutral (alcohol) charges at the physiological pH, which was used in cellular experiments. The dynamic cellular responses, cell uptake, oxidative stress and their effects on cell apoptosis and cell cycle were investigated for diverse chemistry modifications on surface. The results indicated the dependence of surface chemistry and cell type with the biocompatibility of Fe@CNPs. They concluded that except for the carboxyl modified Fe@CNPs, all other Fe@CNPs present low toxicity and can be used for further functionalization and in a wide range of biomedical applications (Mu *et al.*, 2010). Recently, Wang *et al* prepared a new type of hybrid NPs integrated with magnetic Fe₃O₄ nanocrystals and fluorescent C-Dots in porous carbon using a one-pot solvothermal synthesis method. The study demonstrates both the magnetic responsive properties and the optical properties from CDs with strong and upconversion fluorescence, excellent photostability, and an NIR photothermal effect for the developed Fe₃O₄@C-CDs hybrid NPs. The mesoporous structures and hydrophilic surface

functional groups endow the hybrid NPs with high drug loading capacity and excellent dispersibility in aqueous solutions. Combining the non-toxicity and low cost of the carbon materials, the authors recommends the as-prepared Fe₃O₄@C-CDs hybrid NPs as a great promise towards advanced nanoplatforms for simultaneous imaging diagnostics and high efficacy therapy (Wang *et al.*,2014).

Chapter 3
MATERIALS & METHODS

3. MATERIALS & METHODS

This chapter gives an overview of all the materials used in the study and the detailed methodology adopted for the synthesis of different systems. The chapter also deals with the detailed techniques involved in the biological, physical and chemical characterization of the developed system at various stages of the study.

3.1 Materials

All the chemicals employed were used as supplied or freshly prepared unless otherwise stated. Deionized Milli Q water of resistivity 18.2 Ω m was used throughout the experiment. FeCl_3 anhydrous, $\text{FeCl}_2 \cdot 4\text{H}_2\text{O}$, NaOH, 35% HCl (All from Merck, Germany/India) were used for the preparation of USPIONs. Tri-sodium citrate (TSC) (Merck, Germany/India), Dextran (M_w -70,000) (Sigma lifescience), Sodium Alginate Polysaccharide (250 cps), Pullulan (M_w ~100,000) (Sigma Aldrich , St. Louis, MO, USA) were used for the preparation of C-SPIONs, D-SPIONs, A-SPIONs and P-SPIONs respectively. Gold chloride (HAuCl_4) (Sigma Aldrich,USA), Bovine Serum Albumin (BSA) (Sigma Aldrich, USA), Phosphorous pentoxide (P_2O_5) (Merck, India), Acetic acid (Merck, India), 1-Ethyl-3-(3-dimethylaminopropyl)carbodiimide (EDC) (Sigma Aldrich, USA), O-O'Bis 2-(aminopropyl) polyethyleneglycol 1900 (diaminoPEG) (Sigma Aldrich, India). The chemicals used for the cell culture studies were 3-(4, 5- dimethylthiazol-2-yl)-2,5-diphenyl tetrazolium bromide (MTT), Dulbecco's Modified Eagle's Medium (DMEM), sodium bicarbonate, Gentamicin (Himedia, Germany), Amphotericin B solution and FBS (Sigma-Aldrich, Germany).

Human hepatocellular carcinoma (HepG2) and Mouse fibroblast (L929) cell lines were supplied from National Centre for Cell Science (NCCS, Pune). The chemicals used for the development of fibrosis model were CCl₄ (Spectrum Reagents & Chemicals Ltd., India) and Olive oil.

3.2 Development of ironoxide based MR Contrast Agents

3.2.1 Synthesis of Ultra small Super Paramagnetic Iron Oxide nanoparticles (USPIONs)

Alkaline co-precipitation method of ferrous salts was followed for the preparation of USPIONs with slight modifications from the earlier reported method [17]. Briefly, FeCl₃ and FeCl₂.4H₂O were mixed in the 2:1 molar ratio in deionized water. The reaction was carried out at a temperature of 80° C. After adequate mixing, 1M NaOH was added slowly into the system with continuous stirring. Black precipitate resulted indicating the formation of ironoxide nanoparticles and the whole system was allowed to continue under the same reaction condition for another 2 hours to allow complete precipitation. The nanoparticles were magnetically separated and the residue was washed by centrifugation with deionized water and HCL and centrifuged.



3.2.2. Synthesis of Citrate stabilized USPIONs (C-SPIONs)

To stabilize the resultant iron oxide nanoparticles with citrate through hydroxyl interactions, the nanoparticles were dispersed in 0.1 M tri-sodium citrate and stirred for 6 hrs at 80°C. The citrate coated ironoxide nanoparticle suspension was then washed

with deionized water until pH reached around 7. The residual sample was then collected and freeze dried and subsequently used for further characterization.

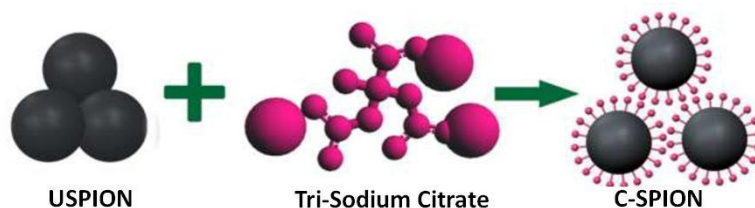


Figure-9. Schematic representation of formation of C-SPIONs

3.2.3. Synthesis of Carbohydrate polymer stabilized SPIONs

3.2.3.1 Synthesis of Dextran Stabilized USPIONs (D-SPIONs)

For the stabilization of USPIONs with carbohydrate polymers, high molecular weight dextran was used for the surface modification. The synthesized iron oxide nanoparticles were dispersed in 3% (w/v) dextran and stirred for 12 hrs. The dextran coated ironoxide nanoparticle suspension was then washed with deionized water. The residual sample was collected by centrifugation.

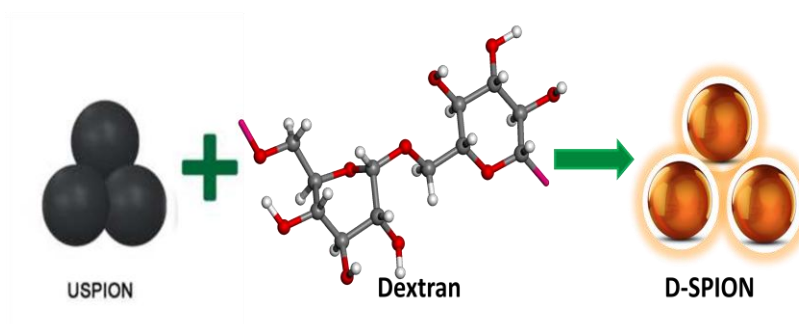


Figure-10. Schematic representation of formation of D-SPIONs

3.2.3.2. Synthesis of Alginate Stabilized SPIONs (A-SPIONs)

Sodium Alginate, a carbohydrate polymer with carboxyl group, enables the ease of further functionalization and has been used as a surface stabilizer for USPIONs. The prepared USPIONs were dispersed in 1.2% (w/v) sodium alginate and stirred overnight. The alginate stabilized ironoxide nanoparticle suspension was then centrifuged and washed to remove unreacted alginate.

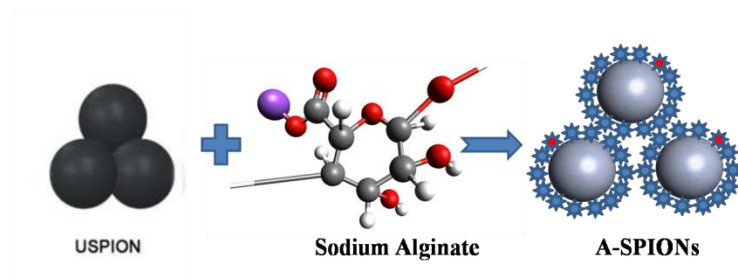


Figure-11. Schematic representation of formation of A-SPIONs

3.2.3.3. *Synthesis of Pullulan Stabilized SPIONs (P-SPIONs)*

Pullulan, a carbohydrate polymer with high liver affinity, has been used for the surface stabilization of the USPIONs. USPIONs were redispersed in 1.2% pullulan to formulate the nanoparticles more stable, biocompatible and hepato-specific. The solution mixture was stirred for 12 hrs. Magnetic separation was carried out to remove excess pullulan. After washing several times, P-SPIONs were dispersed in 10 mL deionized water and used for rest of the studies.

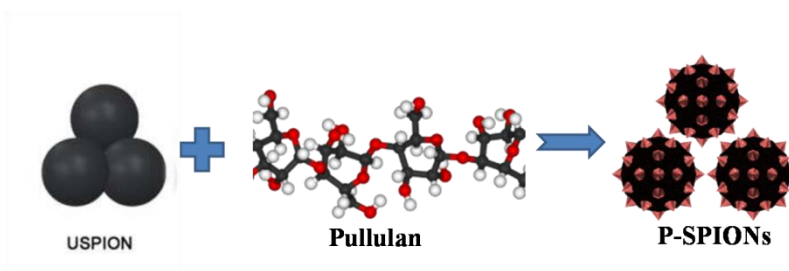


Figure-12. Schematic representation of formation of P-SPIONs

3.3 Preparation of Multimodal nanoprobes

Different surface modified USPIOs were further functionalized with a NIR emitting dye (Atto 700) for using the system for multimodal use of MRI and optical imaging.

3.3.1 Synthesis of Multimodal D-SPIOs (DSPIOs-AT)

D-SPIOs (10 ml of 1.2 mg/ml concentration) were mixed with Atto 700 dye (20 μ L of 1.3 μ g/ μ l concentration) and kept under ultrasonication for 6 hrs. The pale brown colour of the D-SPIOs had changed to pale green colour after sonication. The final suspension was washed by centrifugation and used for further characterization and studies.

3.3.2 Synthesis of Multimodal A-SPIOs (ASPIO-AT)

10 ml of A-SPIOs with 1.2 mg/ml concentration was mixed with 20 μ L Atto 700 dye of concentration, 1.3 μ g/ μ l and kept for ultrasonication for 6 hrs. A change in colour from pale brown of the A-SPIOs to pale green colour was observed after sonication. The suspension thus resulted was washed by centrifugation and used for further characterization.

3.3.3 Synthesis of Multimodal P-SPIOs (PSPIO-AT)

20 μ L of 1.3 μ g/ μ l concentrated Atto dye was added to 10 ml of 1.2 mg/ml P-SPIOs and ultrasonicated for 6 hrs. The colour change as mentioned in sections 3.3.1 and 3.3.2 was observed at the end of 6 hrs of sonication. The final suspension was centrifuged and used for further studies.

3.4 Hybrid nanoprobes using Gold Clusters and SPIONs

3.4.1 Synthesis of Gold Clusters (AuC)

Gold nanoclusters were synthesized from gold chloride in presence of BSA. 5 ml of 10mM Gold chloride solution and 50 mg/ml concentration of 5 ml BSA were mixed in 1:1 ratio under stirring. After 2 min, 0.5 ml of 2 M NaOH was added to the mixture and the reaction was allowed to continue for 6 hrs under mild stirring. The reddish brown solution resulted indicating the formation of red fluorescent gold nano clusters. The resulted gold clusters was dialysed against distilled water for 48 hrs to make it neutral and the purified samples were stored at 4°C for further use.

3.4.2 Synthesis of Hybrid Nanomaterial (ASPION-Au)

5 ml of 2 mg/ml A-SPIONs, 50 mg of EDC, and 2 ml of dialysed Au clusters were used for the preparation of ASPION-Au nanoparticles. As described earlier, carboxyl group in ASPIONs was activated with EDC at 6 pH and stirred for 2 hrs. To it, Au cluster was added , which has free amine groups and stirred for five minutes and the pH was adjusted to 10 and stirred for 12 hrs. The final suspension was washed by centrifugation.

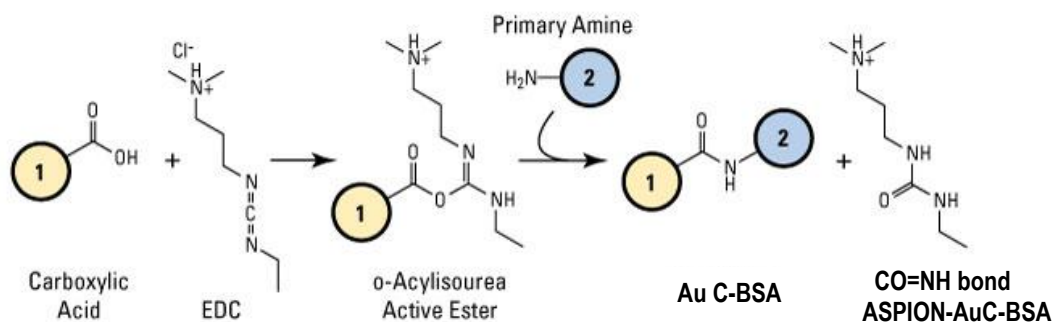


Figure-13. Illustration of the synthesis of the formation of ASPION-Au.

3.5 Hybrid nanoprobes using Carbon dots and SPIONs

3.5.1 Synthesis of Carbon Dots (CDTS)

Carbon dots (CDTS) were synthesized using acetic acid as precursor in presence of P_2O_5 as per the reported procedure (Fang *et al.*, 2012). Briefly, One ml of glacial Acetic acid containing 200 μ L of water was quickly added to 2.5 g of P_2O_5 to produce CDTS. Acetic acid acts both as the carbon precursor and the hydrophilic reaction medium. The colour of the mixture changed to brown within 10s, and the volume of the sticky slurry mixture was dramatically expanded by foaming. The reaction lasted for about 5 min until exhaustion of the P_2O_5 .

3.5.2 Synthesis of Hybrid Nanomaterial (ASPION-CDTS)

A-SPIONs were modified for amine functional groups with diamino PEG by EDC chemistry and the reaction continued for 12 hrs. For this, 5 ml of ASPIONs of concentration 3.5 mg/ml was amine functionalized with 0.3 gm diamino PEG through 2 mg EDC. The final suspension was washed by centrifugation. The carboxyl group of CDTS was activated with EDC and the amine modified A-SPIONs was conjugated with CDTS. The final suspension was washed and centrifuged.

3.5.3 Synthesis of Hybrid Nanomaterial (PSPION-CDTS)

Equal parts of P-SPIONs of 3.5 mg/ml concentration was incorporated with CDTS of 5 mg/ml concentration through physical interaction and stirred for 12 hrs. The final suspension was washed and centrifuged.

3.6 Characterization of the nanoparticles.

3.6.1 Determination of Particle Size

The particle size determination of all the above prepared samples were carried out using two established techniques, TEM and DLS.

3.6.1.1 Transmission Electron Microscopy (TEM)

The size and morphology of the nanoparticles were examined by a transmission electron microscopy at 100 kV (TEM, JEM-2010, JEOL, Tokyo, Japan). The magnetically separated and thoroughly washed samples were dispersed in deionized water followed by ultrasonication for 5 min. A very small amount of sample dispersed in deionized water was allowed to slowly dry on a formvar-coated copper grid for TEM observation. The particle size and size-distributions had been quantified through a visual analysis of particles in the TEM micrographs.

3.6.1.2 Dynamic Light Scattering Technique (DLS)

Hydrodynamic diameter and zeta potentials of the prepared nanoparticles were measured using a dynamic light scattering instrument (DLS, Zetasizer NanoZS90, Malvern Instruments Ltd., Worcestershire, UK). Samples were dispersed in deionized water in a very low concentration followed by ultrasonification for 5 min. This solution was transferred into a polystyrene cuvette and placed in the He–Ne laser beam at scattering angle of 90° at room temperature 25° C.

3.6.2 Determination of Phase by X-ray Diffraction Technique (XRD)

The phase analysis of the nanoparticles in powder form was carried out using X'Pert PRO X-ray diffraction instrument. Crystal structure was determined by analyzing

the position and intensities of diffraction peaks observed in the range of diffraction angle $2\theta = 10 - 80^\circ$ using Cu K α radiation of 1.5406 Å at 40 kV and a 20 mA current strength.

3.6.3 Surface characterization of the nanoparticles

The coating efficiency of the surface modified USPIONs were evaluated using Fourier Transform Infra-red spectroscopy (FT-IR) and Thermo Gravimetric Analysis(TGA).

3.6.3.1 Fourier Transform Infra-red spectroscopy (FT-IR)

Fourier transform infrared (FTIR) spectra of the bare and coated USPIONs, Au Clusters, CDTS and the pure polymers used for the stabilization were recorded using Thermo Nicolet 5700 FTIR spectrometer(USA) in the diffuse reflectance mode. To enable high signal to noise ratio, 64 scans were acquired at a resolution of 4 cm⁻¹.

3.6.3.2 Thermo Gravimetric Analysis (TGA)

The thermal properties of the prepared materials in the powder form were assessed using thermo gravimetric analysis (TGA) using SDT 2960 V2.2B (simultaneous TGA-DTA, TA Instruments, Delaware, USA) instrument which was also used to evaluate the amount of polymer bound to the nanoparticles. The experiment was run under oxygen atmosphere within a temperature range of 25–1200°C applying a constant heating rate of 10°C/min. The percentage of weight loss at different stages accounted for the degradation of the organic content present in the sample.

3.6.4 Characterization of magnetic properties

3.6.4.1 Magnetic Property

The magnetic property of bare and coated USPIOs was measured at room temperature using a Lakeshore model 7410 vibrational sample magnetometer (VSM). The samples in the powder form were weighted and tightly packed in the sample holder and it is then introduced into the sample chamber within the strong magnetic field. The magnetic hysteresis and saturation magnetization of both were evaluated in all the cases.

3.6.4.2 Magnetic Relaxivity measurements

For measuring the magnetic relaxation property of the material, MR images of bare and coated USPIOs suspensions were acquired using a clinical, 1.5 T whole body MR scanner (MAGNETOM Avento Tim System 1.5 T, Siemens, Munich, Germany) using a 12 channel head coil. A series of study with iron concentrations of 0.45, 0.23, 0.11, 0.06, 0.03 and 0.0 mM were performed using aqueous phantoms of the samples. An inversion recovery sequence with constant repetition time (TR) and echo time (TE) of 4000 and 11 ms respectively with varying inversion time (TI) of 50, 100, 300, 700, 1200, 2000 and 3000 ms was used for calculating longitudinal relaxation rate (r_1). A modified transverse relaxometry spin echo sequence with TR of 2000 ms with varying TE from 15 to 150 ms was used for getting transverse relaxation rate (r_2). Both sequences were run at three different planes of the phantoms with a slice separation of 10 mm.

Pixel intensity with respect to each concentration was extracted from the resulting MRI maps. Signal intensity against TI and TE values were plotted for getting T_1 and T_2 relaxation times respectively. Likewise, T_1 and T_2 relaxation times for different concentration were obtained. These values were plotted against the iron

concentrations. Longitudinal and transverse relaxation values (r_1 and r_2) were calculated by the linear fit as reported elsewhere (Nidhin *et al.*, 2013; Wan *et al.*, 2012).

3.6.4.3 Hyperthermia

The heat generation of magnetic nanoparticles (MNPs) was investigated using EASY HEAT laboratory system at 275 KHz. One of the advantages of this induction coil is that the magnetic field can be varied by adjusting the current supplied to the coil. The current was changed from 200 to 400 A in steps of 50 A at a fixed frequency of 275 kHz. The number of turns and the diameter of the coil are fixed. The induction heating treatment was performed by suspending the sample particles in 1 ml of distilled water in a 1.5 ml non-magnetic centrifuge tube and was kept at the centre of the coil. The temperature profile was recorded for 15min using noncontact IR thermometer. Exposure of magnetic field strength increases the temperature of the ferrofluid and saturates after a particular temperature.

3.6.5 Characterization of Optical property

Optical properties of the CDTs and Au cluster based nanoprobes were characterized by measuring the absorbance by UV-Vis spectrophotometer (Shimadzu UV-1800, Japan) and fluorescence by spectrofluorometer (Fluorolog-III; Jobin Yvon Inc., USA) and optical imaging system (Xenogen IVIS *in vivo* imaging system).

3.7 Hemocompatibility Evaluation

3.7.1 RBC aggregation

Fresh human Red blood Cells (RBC) were collected by centrifugation of citrated blood at 700 rpm for 10 min and diluted with normal saline in the ratio 1:10. 100 μ l of

100 µg/ml concentration of the nanoprobe were added to 100 µl of diluted RBC and incubated for 30 min at 37°C. Aggregation if any was visually assessed through phase contrast microscope (Leica DM IRB, Germany). Saline was used as negative control and polyethyleneimine (PEI) as positive control.

3.7.2 WBC and Platelet aggregation

Fresh human whole blood was centrifuged at 800 rpm for 20 min and layered on histopaque. The white turbid ring and slightly yellow colouration just above the ring layered above the transparent histopaque layer represents the WBC and platelets. Aggregation if any was observed under a Phase Contrast microscope.

3.7.3 Hemolysis assay

For hemolysis study, 800 µl of separated human RBC was taken and made up to 3 ml with saline and mixed gently. Then 900 µl of 100 µg/ml nanoprobe dispersed in saline was added to 100 µl of washed RBC, mixed gently and incubated for 2 h. The sample was centrifuged for 5 min at 1500 rpm and to the supernatant solution, 900 µl of saline was added and the absorption at 541 nm was recorded using UV spectrophotometer (Carywin UV). Saline was used as the negative control and distilled water as positive control to calculate the percentage hemolysis as follows:

$$\% \text{ Hemolysis} = (\text{OD}_{\text{sample}} - \text{OD}_{\text{Negative}}) / (\text{OD}_{\text{positive}} - \text{OD}_{\text{Negative}}) \times 100$$

The percentage hemolysis thus calculated was then compared with the already reported admissible limit of hemolysis (< 1%).

3.8 Cell culture studies

3.8.1 Cytotoxicity assessment

Cytotoxicity of the nanoprobes on hepato-cellular carcinoma cells, HepG2, was assessed by standard MTT assay in triplicate. Different concentrations of nanoprobes (100, 50 and 25 µg/ml), negative and positive controls were added to the cells and incubated for 24 h. Upon removal of the media, MTT (0.2 mg/ml) was added to each well and again incubated for 3 h. Subsequent removal of MTT is followed by the addition of dimethyl sulfoxide to dissolve the formed formazan crystals and incubated for 30 min. Absorbance was quantified based on the peak at 570 nm using micro plate reader (Biotech, Power wave XS, USA) The percentage viability was calculated from the relation, $[\text{Abs}(\text{sample})/\text{Abs}(\text{control})]*100$.

3.8.2 Cell uptake efficiency

HepG2 cells were incubated with USPIO based nanoprobes and confirmed the uptake and localization of particles in the cells using iron specific Prussian blue staining. CDTS based nanoprobes on incubation with the cells were imaged using Fluorescence Microscopy.

3.9 In vivo studies

3.9.1 Animal Model Development for liver fibrosis

All studies involving animals were approved by the Institutional Animal Ethics Committee of Sree Chitra Tirunal Institute for Medical Sciences and Technology. The animal model for liver fibrosis was developed as per reported protocol of Constandinou, Henderson, & Iredale, 2005. For MRI studies, rat model for liver fibrosis was developed.

For this, male Wistar rats weighing 200–250 g were treated twice a week, intraperitoneally, with equal parts of CCl₄ and olive oil for 6 weeks. For the initial two weeks, 0.2 ml/100 g of the CCl₄-olive oil mix was administered and the dose was reduced to 0.1 ml/100 g for the subsequent weeks. Development of liver fibrosis was confirmed by liver function test for the liver enzyme serum glutamic oxaloacetic transaminase (SGOT) and serum glutamic pyruvic transaminase (SGPT) by the end of six weeks. Histopathology of the organ also confirmed the developed fibrosis.

For optical imaging, mouse model for liver fibrosis was developed. Briefly, male swiss albino mice weighing 30-35gm were treated with 1:7 ratio CCl₄:olive oil mix intraperitoneally at the dosage of 1 µL/g body weight every 5 day for 4 weeks. The LFT and post imaging histopathology confirmed the fibrosis development in mice.

3.9.2 *In vivo* MRI measurements

Animal MRI studies were performed on a 1.5 T clinical magnet running a multisection T₂-weighted turbo spin echo sequence (TR 5780 ms; TE 125 ms; FOV 98 mm × 140 mm; slice thickness 3 mm; flip angle 90). Animals were anaesthetized using ketamine and xylazine at a dosage of 70 mg/kg and 5 mg/kg of body weight before MRI scan procedure.

The developed contrast agent were administered through tail vein at a dose of 2.17 mg/ml (0.04 mM) Fe/kg body weight. MRI scan was performed before and after 15 min of contrast agent administration. Signal intensity corresponding to pre and post contrast images was extracted and the percentage signal intensity change was calculated.

3.9.3 *In vivo* Optical Imaging

In vivo optical imaging was performed by the Xenogen IVIS spectrum *in vivo* optical imaging system having excitation filters in the range 430-780 nm and emission filters in the range 500-800 nm.

3.9.3.1 In vivo Optical imaging of multimodal nanoprobes.

For the diagnosis of liver fibrosis, mice were anesthetized and the multimodal nanoprobes (DSPION-AT, ASPION-AT & PSPION-AT) were injected independently intravenously through tail vein (200 µl) and images were taken after 20 min post injection. The excitation and emission filters corresponding to the excitation and emission of ATTO dye (675 and 720 nm respectively) were used for imaging.

3.9.3.2 In vivo optical imaging of Hybrid nanoprobes

For the diagnosis of liver fibrosis with carbon dot based hybrid nanoprobes, mice were anesthetized and the hybrid nanoprobes (ASPION-CDTS & PSPION-CDTS) were injected intravenously (200 µl) through tail vein and images were taken after 20 min of the injection. The excitation and emission filters corresponding to that of the excitation and emission of CDTS based probes were used (430 and 500 nm respectively).

3.9.4 Histological analysis.

In all the cases, animals were sacrificed after 2 h of nanoprobe injection and subsequent imaging to remove the liver for histological analysis. The tissues were fixed with 10% neutral buffered formalin and embedded in paraffin and sectioned. The sections were stained with haematoxylin–eosin (H&E) for histological analysis. Masson's trichrome (MT) and Pearls' Prussian blue (PB) staining were done to assess

the degree of fibrosis as exhibited by the collagen fibres and the presence of iron in the liver, respectively.

Chapter 4

RESULTS

4. RESULTS

This chapter includes the results of various studies carried out to fulfill the objective of the thesis. Results of the three major groups of nanoprobe considered in this study ie USPIONs, multimodal nanoprobe and hybrid nanoprobe with additional subheads categorizing them to specific groups are covered. The major heads under which the results are compiled includes synthesis, physico-chemical and magnetic characterization, biological evaluation and characterization *in vivo* and *in vitro* studies and hyperthermia.

4.1 Preparation of ironoxide based MR Contrast Agents

For using USPIONs as MR contrast agents, they have been modified with four different stabilizers for liver specific MR imaging, after synthesis. The detailed synthesis and characterization of all the nanoprobe are described in the following sections.

4.1.1 Synthesis of Ultra small Super Paramagnetic Iron Oxide nanoparticles (USPIONs)

The synthesized USPIONs were brownish black in colour and colloidal solution was not well dispersed. The dispersivity was also not stable and showed aggregation in two or three days. The bare USPIONs have greater chance to react with oxygen which indirectly will affect its physico-chemical and magnetic properties drastically. So to improve its properties and also for long term storage of USPIONs, surface modification was performed with a variety of agents.

4.1.2. Synthesis of Citrate stabilised SPIONs (C-SPIONs)

C-SPIONs prepared as a result of the hydroxyl interaction of TSC with Fe atom of USPIONs resulted in the formation of a stable colloid suspension of C-SPIONs. The colloidal suspension was found to be non-aggregated with improved magnetic properties compared to USPIONs which could be visualized with a rare earth magnet.

4.1.3. Synthesis of Carbohydrate polymer stabilised SPIONs

The electrostatic interaction of hydroxyl group of dextran with iron atom at the ambient conditions resulted in the production of D-SPIONs with optimum size. The D-SPIONs also remained as a highly stable colloidal suspension which will favour the improved shelf life of the contrast agent.

A-SPIONs were formed due to the electrostatic interaction of hydroxyl group of alginate. In this case the added advantage is that the carboxylic group present in the ASPIONs can be utilized for further modification of the nanoprobe. Alginate, an anionic polymer extracted from brown algae bears carboxylic acid groups that may introduce negative charge to the polymer at appropriate pH values. The stability of the A-SPIONs was excellent and further modification for a multimodal functionality can be appreciated.

The hydroxyl interaction of the pullulan with SPIONs resulted in the production of P-SPIONs. We approached a green route of synthesis in order to avoid complex formulations since the intended end use is the successful delivery of P-SPIONs as hepatocyte-specific MR contrast agent. The resulted suspension was found to be very

stable without any aggregation. The excellent influence of magnetic field was also visualized by a rare earth magnet.

4.1.4 Results of Physico-Chemical & Magnetic Characterization.

4.1.4.1 Determination of Particle Size

The particle size analysis was carried out using TEM and DLS techniques. The TEM micrograph indicates that all the surface modified and the bare USPIOs have narrow size distribution in the range 10–15 nm with an average diameter of 12 nm. Well dispersed pattern of particles is observed in the TEM of C-SPIOs, D-SPIOs, A-SPIOs and P-SPIOs compared to an aggregated pattern in USPIOs (Figure-14). The aqueous dispersivity is best in the case of A-SPIOs.

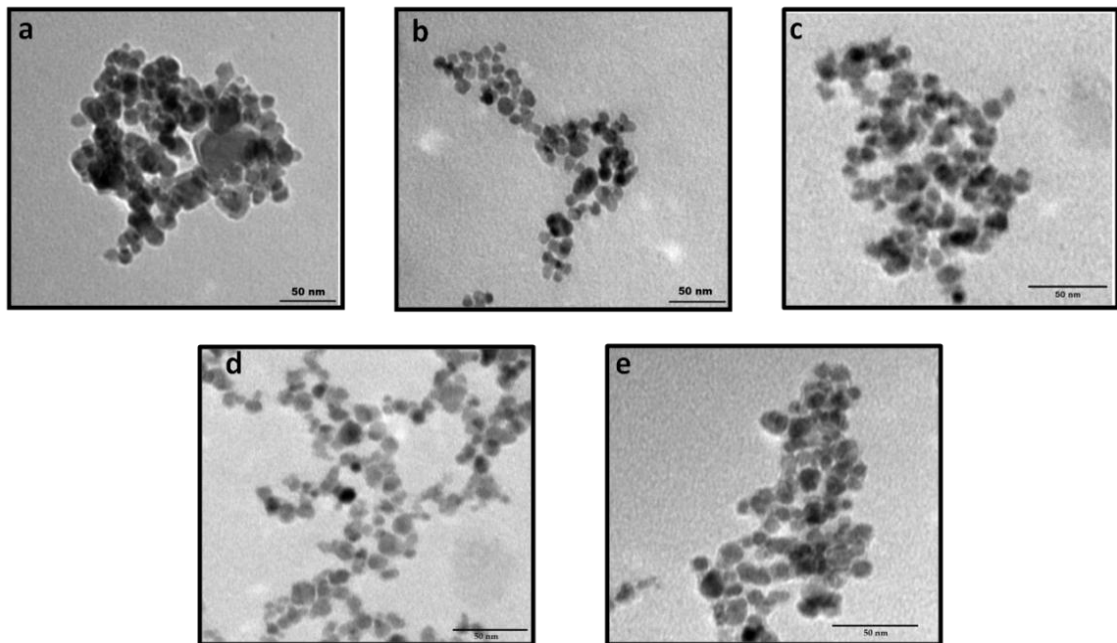


Figure - 14. TEM image of (a) bare USPIO (b) C-SPIO (c) D-SPIO (d) A-SPIO and (e) P-SPIO (all scale bars are 50nm)

DLS showed hydrodynamic diameter of 24 nm for USPIONs, 30 nm for C-SPIONs, 50 nm for D-SPIONs, 40 nm for A-SPIONs and 80 nm for P-SPIONs (Figure-15).

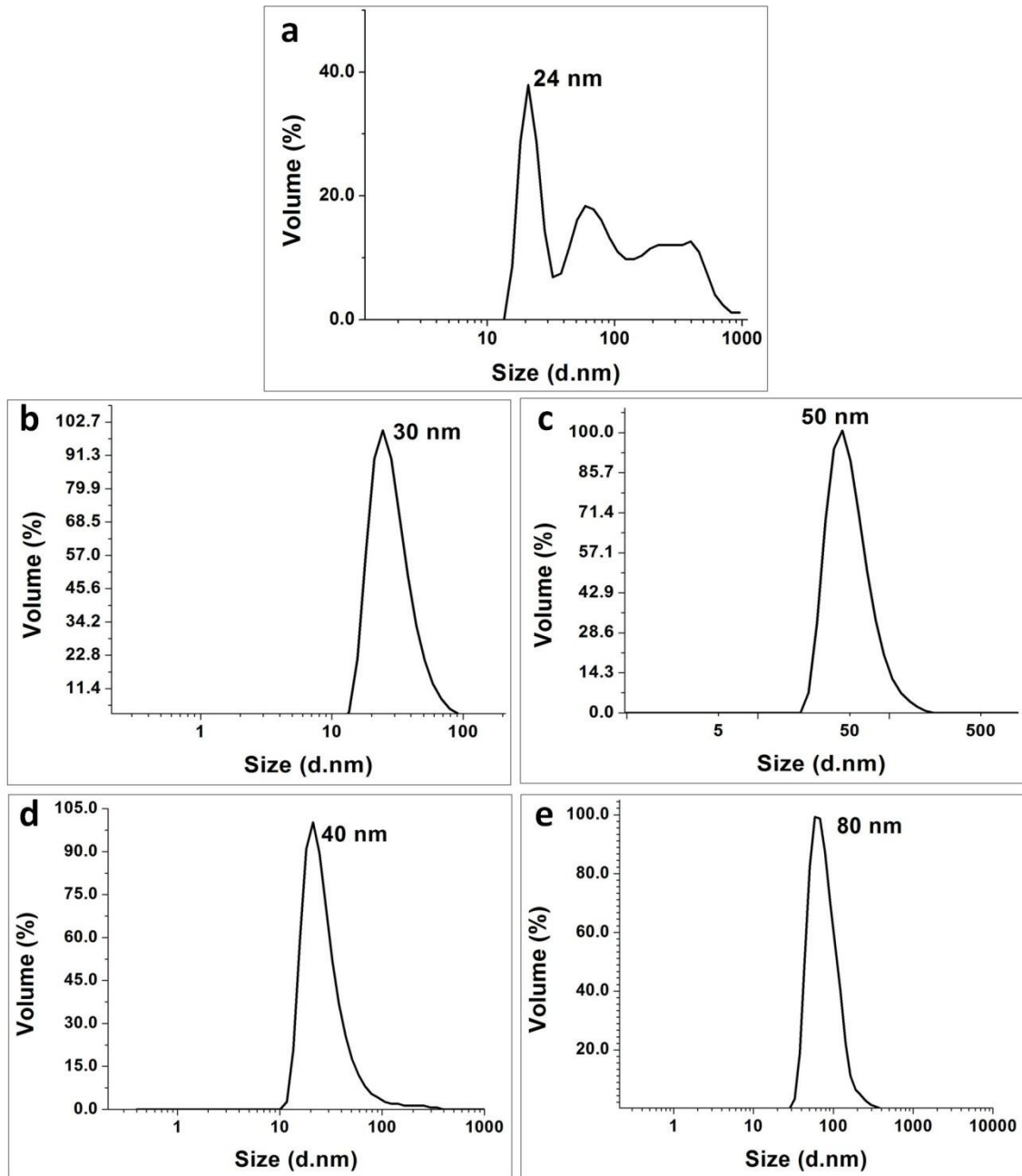


Figure - 15. Hydrodynamic size distribution of (a) bare USPION (b) C-SPION (c) D-SPION (d) A-SPION and (e) P-SPION.

4.1.4.2 Results of X-ray Diffraction studies (XRD)

The XRD pattern of USPIO (Figure - 16) reveals the inverse spinel structure of magnetite with the indices (1 1 1), (2 2 0), (3 1 1), (2 2 2), (4 0 0), (4 2 2), (5 1 1) and (4 4 0) as per the JCPDS Card No. 89-0691. The XRD patterns of C-SPIONs, D-SPIONs, A-SPIONs and P-SPIONs retained the magnetite phase.

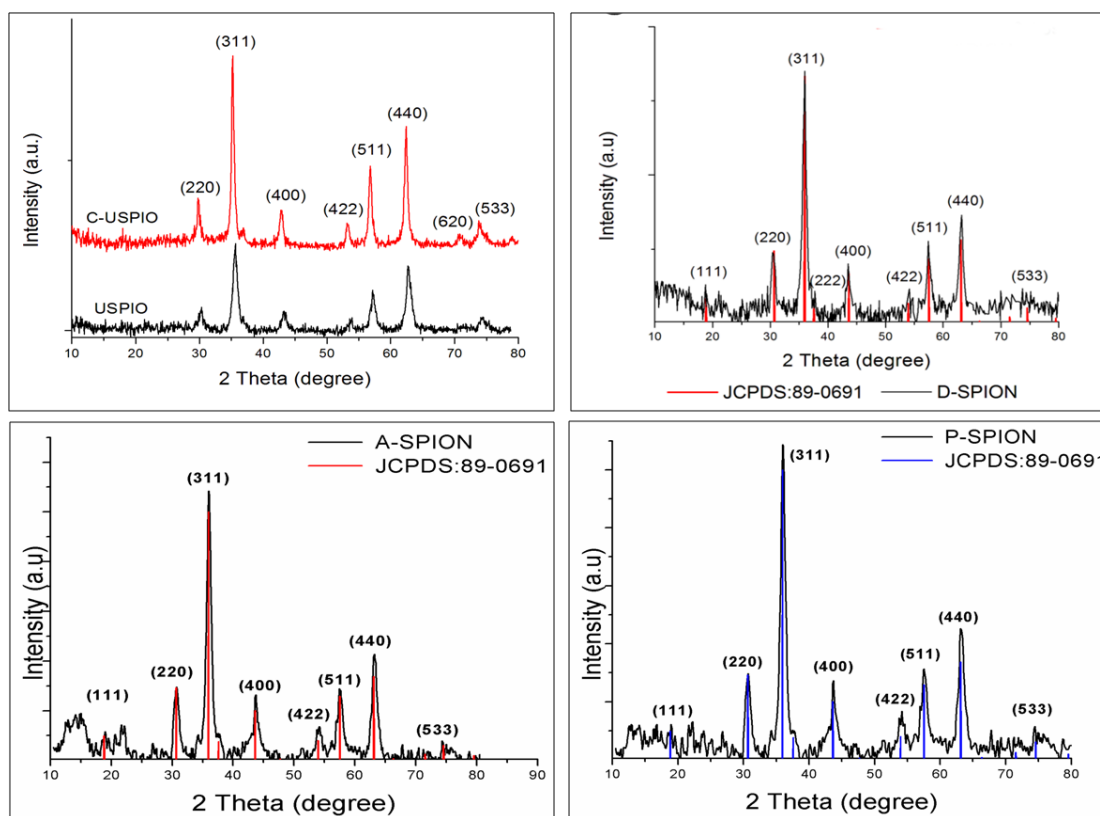


Figure - 16. XRD pattern of bare USPIOs, C-SPIONs, D-SPIONs, A-SPIONs and P-SPIONs

4.1.4.3 Fourier Transform Infra-red spectroscopy (FT-IR)

The FTIR spectra of USPIO showed prominent bands at 572 and 450 cm^{-1} corresponding to the vibrations of Fe-O. The prominent FTIR bands of TSC are

positioned at around 3264, 1605, 1397, 1314, 1283, 1148, 1075 and 961 cm^{-1} . The FTIR bands at 1618, 1397, 1065 and 597 cm^{-1} present in the C-SPIONs confirmed the citrate coating in the case of C-SPIONs (Figure-17b). The FTIR bands of dextran were found to be around 3501, 2926, 1652, 1460 and 1005 cm^{-1} which on conjugation with USPIONs exhibited slight shift and the distinct bands are observed around 3305, 2932, 1652, 1364, 1023 and 597 cm^{-1} for D-SPIONs (Figure-17c). Pure sodium alginate showed IR bands around 3389, 1611, 1413 and 1029 cm^{-1} whereas A-SPIONs exhibited bands around 3361, 1621, 1413, 1060 and 582 cm^{-1} . The corresponding bands of alginate with shift and Fe-O band at 582 cm^{-1} confirms the formation of ASPIONs. (Figure-17d) Pullulan have sharp vibrational modes near 3362, 2924, 1623, 1357, 1025 and 955 cm^{-1} . The P-SPION exhibited bands corresponding to that of pullulan and Fe-O at 3378, 1616, 1408, 1025, and 568 cm^{-1} (Figure-17e).

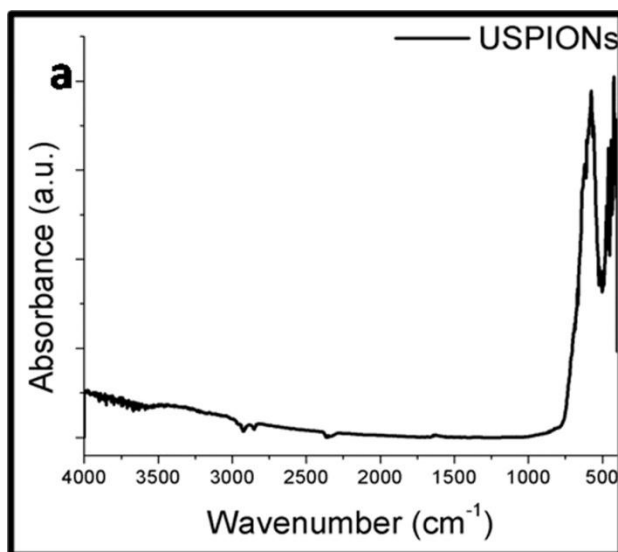


Figure - 17. FTIR spectrum of (a) bare USPION

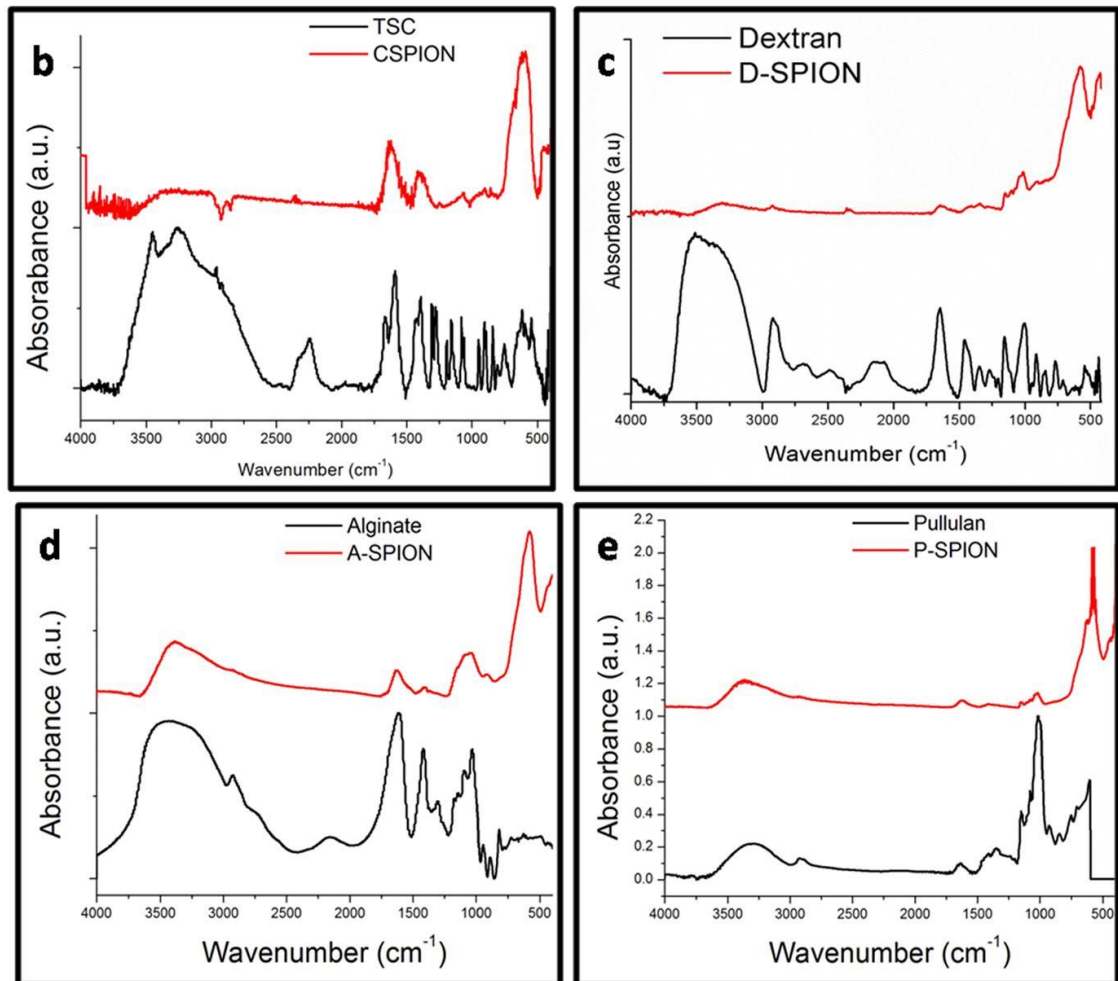


Figure - 17. FTIR spectra of (b) tri-sodium citrate and C-SPION (c) Dextran and D-SPION (d) Sodium Alginate and A-SPION and (e) Pullulan and P-SPION.

4.1.4.4 Thermo Gravimetric Analysis(TGA)

TGA plot of TSC shows four distinct stages of thermal decompositions around 171, 321, 557 and 1120°C corresponding to the total weight loss of 13.23, 26.52, 45.51, and 98.29% respectively (Figure-18a). TGA curve of C-SPIONs also show four similar stages of decomposition around 147, 315, 597 and 1188°C corresponding to the total weight loss of 2.3, 4.6, 5.7 and 7.1%. TGA studies of D-SPIONs and free dextran in the range 0–1200°C and the corresponding thermal decomposition curves are shown in

Figure-18b. Free dextran shows three distinct degradation stages at 118, 357 and 492°C with a corresponding total weight loss of 10, 77 and 100%. The TGA curve of D-SPIONs also shows corresponding stages of degradation around 120°C with a weight loss of 2.31% and around 320°C with a weight loss of 8.94%. At around 490°C a total weight loss is observed.

TGA curve of alginate showed decompositions at 85°C, 209°C and 268°C with a 50% weight loss. At the temperature around 788°C, a total weight loss of 77% was observed. The corresponding degradation of alginate in ASPIONs shows around 115°C, 189°C, 261°C and 794°C with a total weight loss of 24% (Figure-18c). From the TGA curve of pure pullulan, the sharp bends can be observed at 287°C and at 492°C. The thermal degradation of pullulan in P-SPIONs is observed at around 183°C with a weight loss of 4% and at 650°C with a total weight loss of 12% (Figure- 18d).

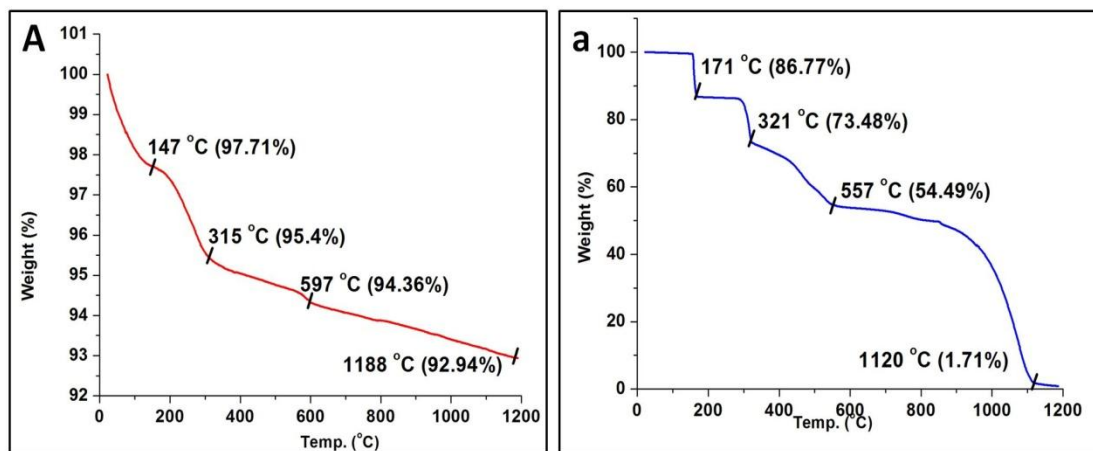


Figure - 18. TGA curves of C-SPION (A) and tri-sodium citrate (a),

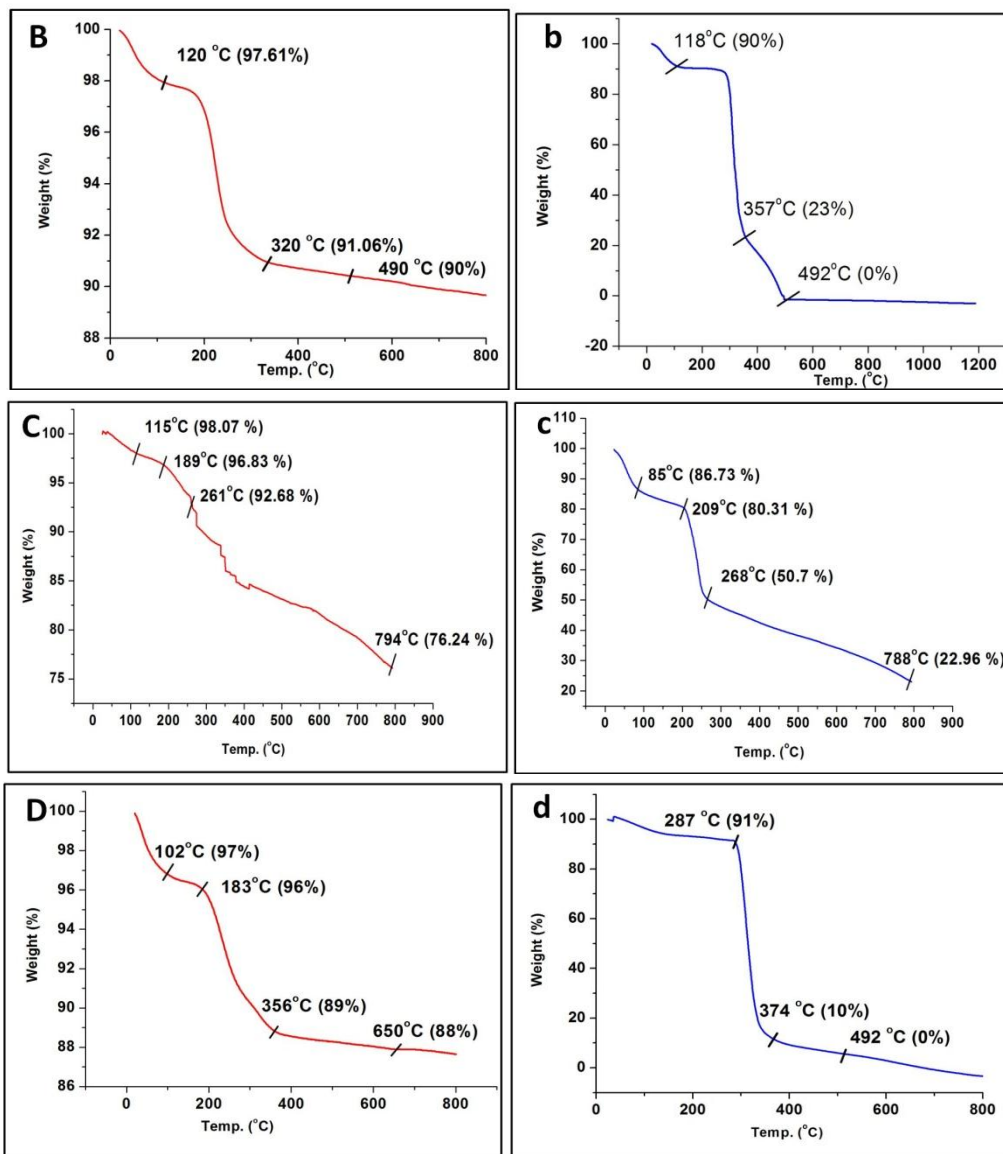


Figure - 18. TGA curves of D-SPION (B) and Dextran (b), A-SPION (C) and Sodium Alginate (c) and P-SPION (D) and Pullulan (d)

4.1.4.5 Magnetic Property

The magnetic nature and saturation magnetization of the USPIONs were evaluated using VSM technique. The hysteresis loop at room temperature showed zero coercivity (Figure - 19) for all the SPIONs which is a characteristic property of superparamagnetic materials. USPIONs showed high saturation magnetization of 62.7emu/g. On surface

modification, the C-SPIONs, D-SPIONs, A-SPIONs and P-SPIONs possessed a saturation magnetization of 57.5, 45.8, 53 and 24.9 emu/g respectively.

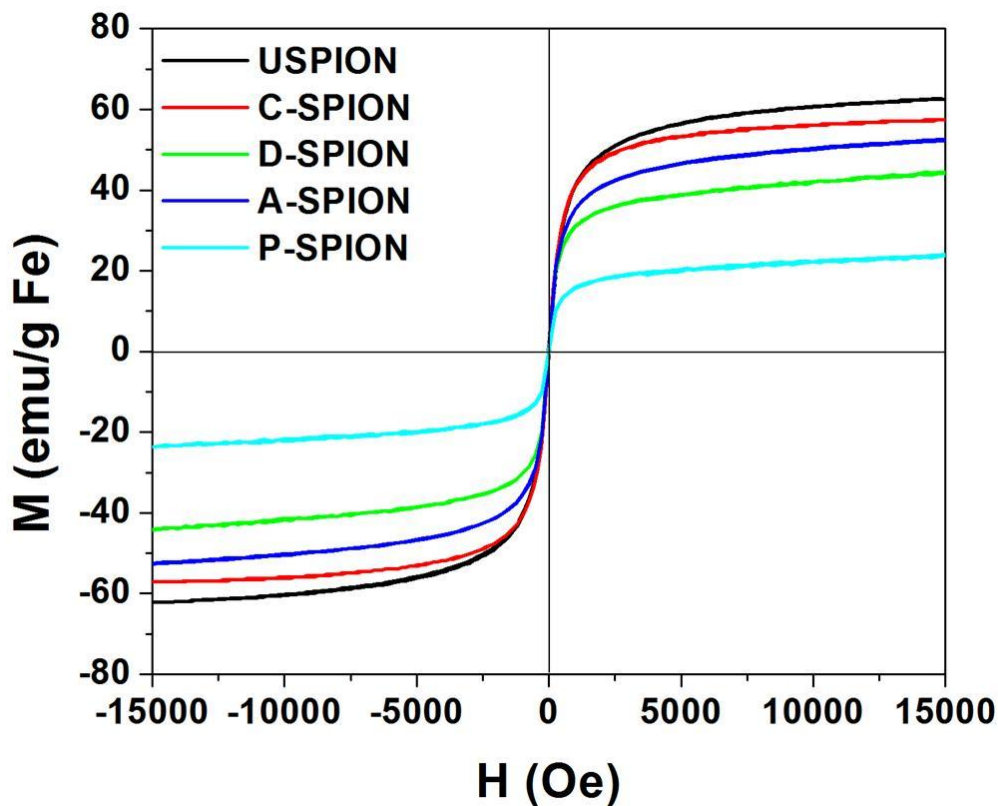


Figure - 19. M-H curve of (a) bare USPION (b) C-SPION (c) D-SPION (d) A-SPION and (e) P-SPION.

4.1.4.6 Magnetic Relaxivity measurements

Based on the pixel intensity expressions of the MRI images, longitudinal and transverse relaxivity (r_1 and r_2) of USPIONs were calculated. Increase in the concentrations of the particles resulted in the loss of signal intensity in the T_2 weighted MR images. Transverse relaxivity was calculated from the slope of linear plots of $1/T_2$ versus iron concentration. An r_2 value of $57 \text{ mM}^{-1}\text{s}^{-1}$ is achieved for USPIONs (Figure-20a). In T_1 weighted imaging, MR images showed increase in pixel intensity of the phantom images

with the increase in iron concentration. T_1 weighted MR images and r_1 values calculated by the linear fit shows an r_1 value of 1.53 for USPIOs.

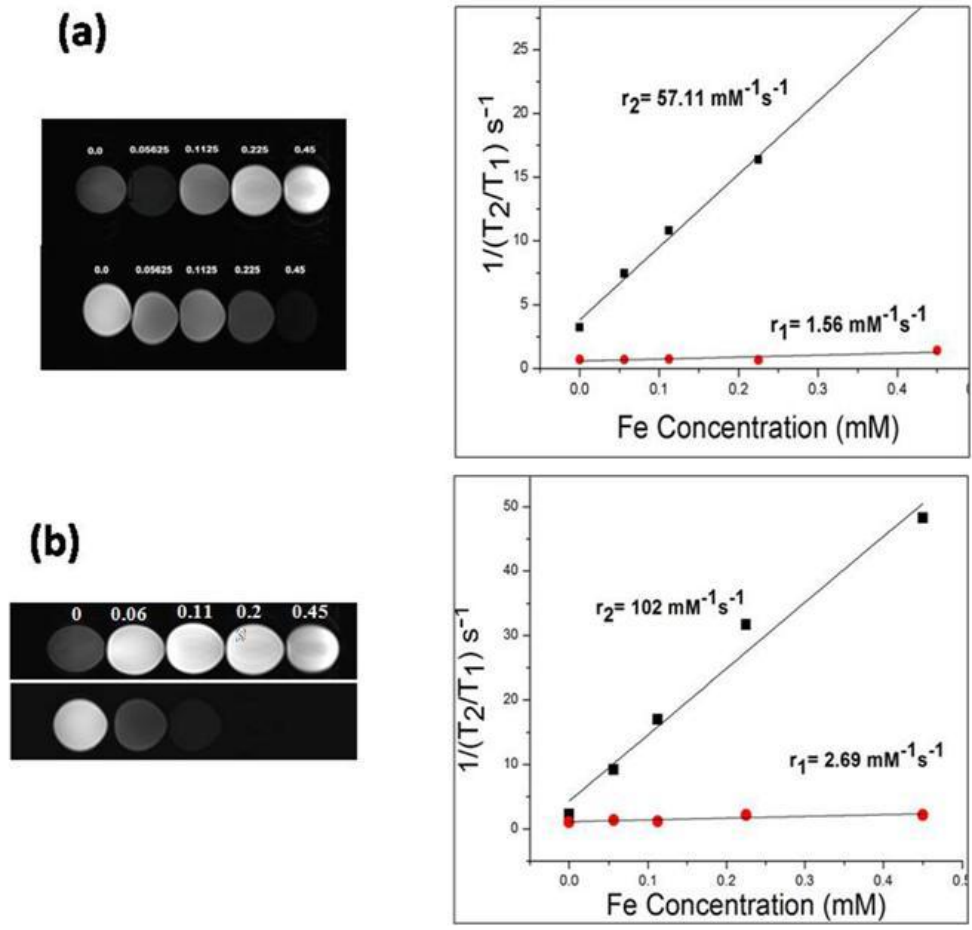
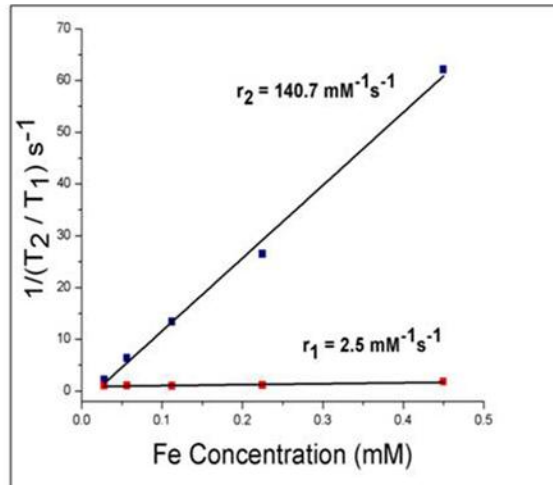
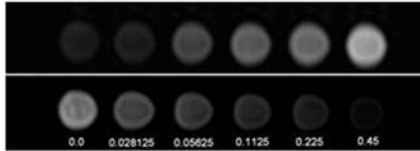
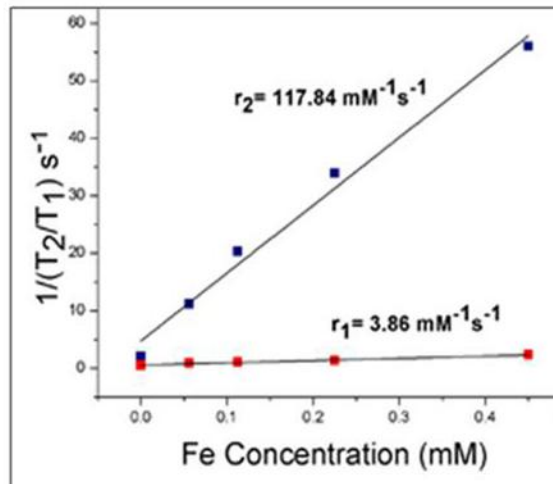
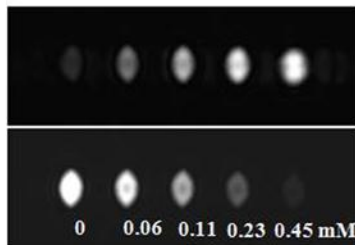


Figure-20. Figures on left side shows T_1 (upper) & T_2 (lower) weighted MR images for varying concentrations (0-0.45mM) and on right side shows Longitudinal (r_1) and Transverse relaxation rates (r_2) of (a) USPIO (b) C-SPION

(c)



(d)



(e)

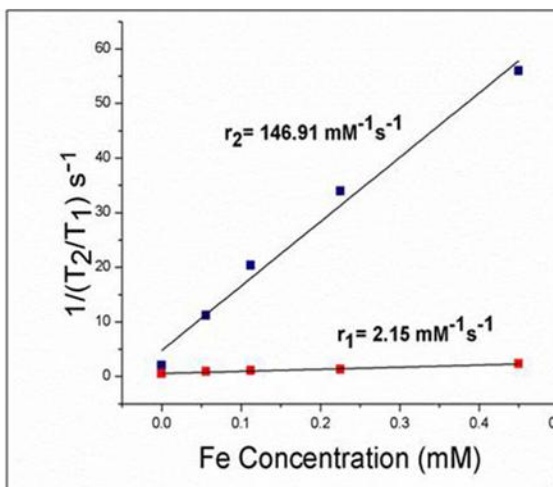
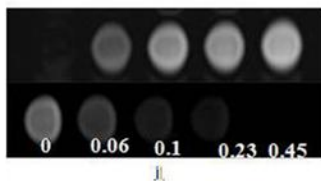


Figure-20. Figures on left side shows T_1 (upper) & T_2 (lower) weighted MR images for varying concentrations (0-0.45mM) and on right side shows Longitudinal (r_1) and Transverse relaxation rates (r_2) of (c) D-SPION (d) A-SPION and (e) P-SPION

Enhanced magnetic relaxivity values were observed in the T_1 and T_2 weighted images of the surface modified SPIONs also. The r_2 values obtained for C-SPIONs, D-SPIONs, A-SPIONs and P-SPIONs were 102, 140.7, 117.84 and 146.91 $\text{mM}^{-1}\text{s}^{-1}$ respectively. Calculated r_1 values were 2.69, 2.5, 3.86 and 2.15 $\text{mM}^{-1}\text{s}^{-1}$ respectively (Figure -20(b-e)).

4.1.4.7 Hyperthermia

The SPION samples were tested for heating effects and results are presented in Figure -21. The temperature of formulations is plotted as a function of time at the constant frequency of 275 kHz and the current changed from 200 to 400 A with an increment of 50 A. For the bare SPIONs, the temperature rise upto 55°C has been achieved on applying a current of 400A for 900 seconds. The temperature elevated to 40°C on applying a current of 300A in 6 minutes. At the same time, the C-SPION's, D-SPION's and A-SPION's temperature elevated to 40°C in 8 minutes by applying 300A current. P-SPIONs reached up to 40°C by the application of 400A for 8 min. All the SPIONs at a lower concentration of 5 mg/ml are capable of generating temperature of the order of 40°C on applying very low current for a short time duration proving them to be good candidates for hyperthermia.

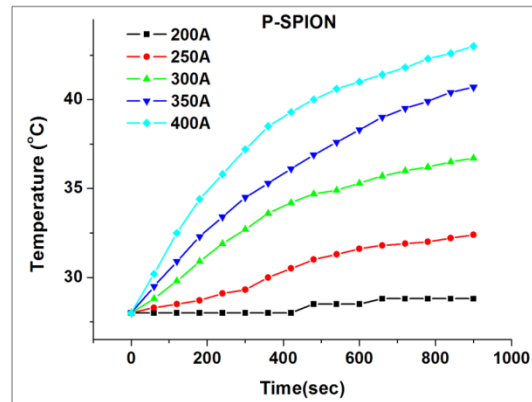
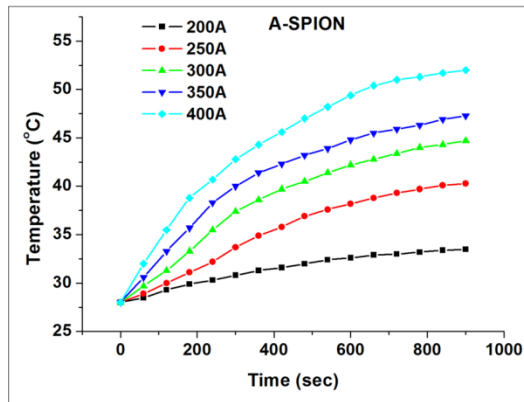
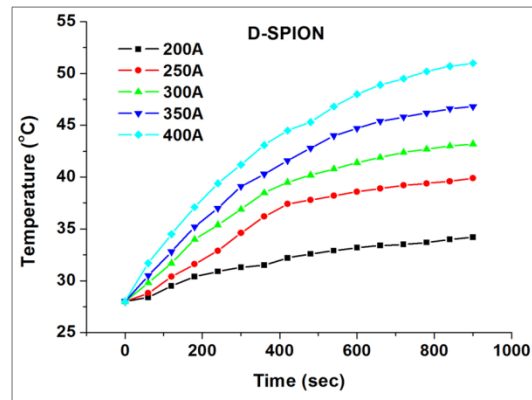
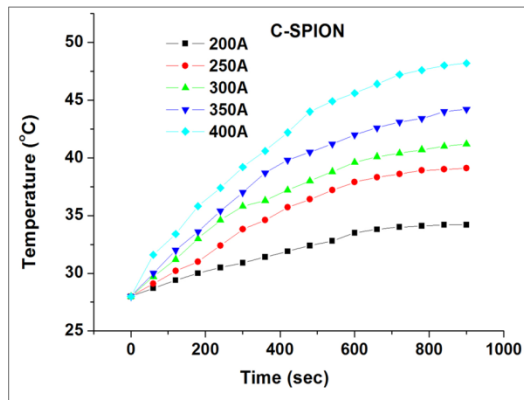
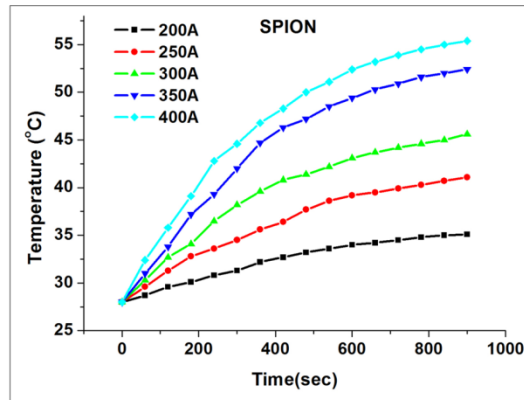


Figure-21. Time-Temperature plot of bare SPION, C-SPION, D-SPION, A-SPION and P-SPION on the application of varying current at a frequency of 275 KHz.

4.1.5 Hemocompatibility Evaluation

Aggregation study of all the SPIONs with human RBC, WBC and platelet did not show any aggregation or morphological change under microscopic view, compared to the positive control PEI in any of the cases (Figure-22). The results of percentage hemolysis analysis of 100 $\mu\text{g}/\text{ml}$ concentration of SPIONs showed no lysis when the particles were in contact with the erythrocytes. The percentage of lysis was found to be less than 1% with all the surface modified SPIONs.

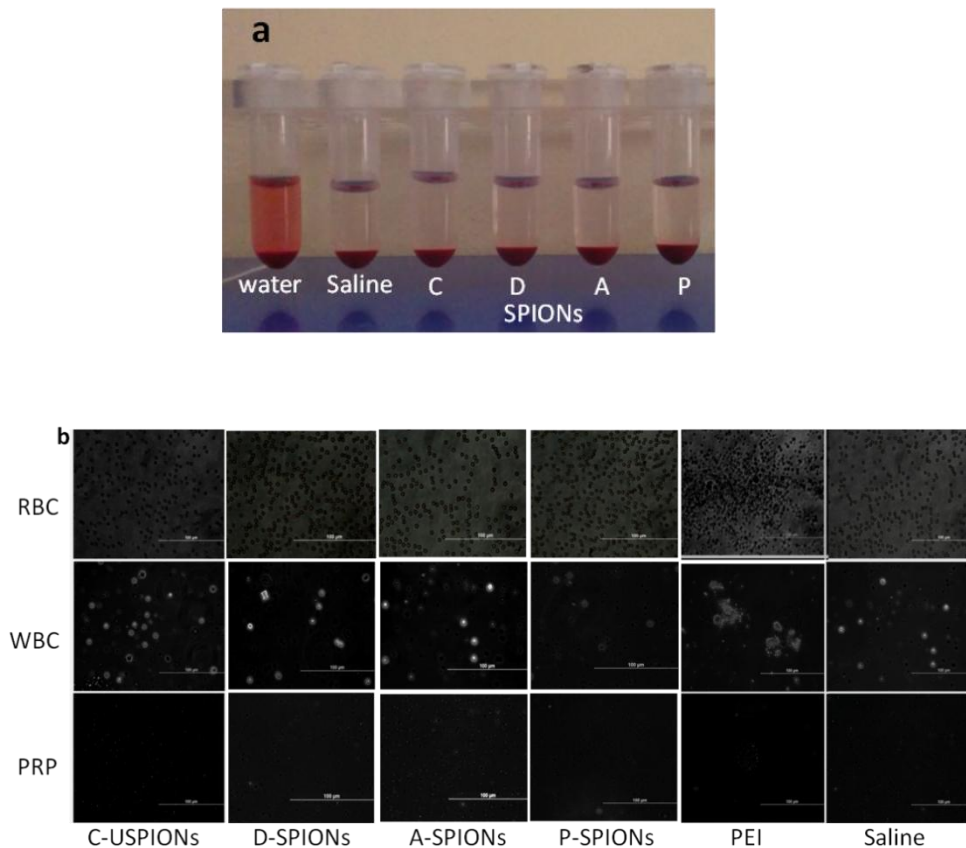


Figure - 22. (a) The photographic image of the hemolysis study of all SPIONs, water and saline. (b) Blood aggregation studies: RBCs, WBC's and platelets incubated with C-SPIONs, D-SPIONs, A-SPIONs, P-SPIONs, positive control, PEI and negative control, saline.

4.1.6 Cell culture studies

4.1.6.1 Cytotoxicity assessment

As the aim of the study is to use the developed nanoparticles as MR contrast materials for liver fibrosis, it is important to see the toxicity effect of the particles on liver cells. Hence, cytotoxicity of the bare USPIOs and the surface modified SPIONs were evaluated on human hepatocellular cells, HepG2 using MTT assay (Figure – 23). 76 - 85 % viability of cells was obtained for bare USPIOs for 100 – 25 $\mu\text{g/ml}$ concentrations respectively where as for coated USPIOs, the cell viability increased to 89 – 98.5% for C-SPIONs, 82 -100 % for D-SPIONs, 89 – 106 % for A-SPIONs and 91 – 113 % for P-SPIONs respectively for the same range of concentrations.

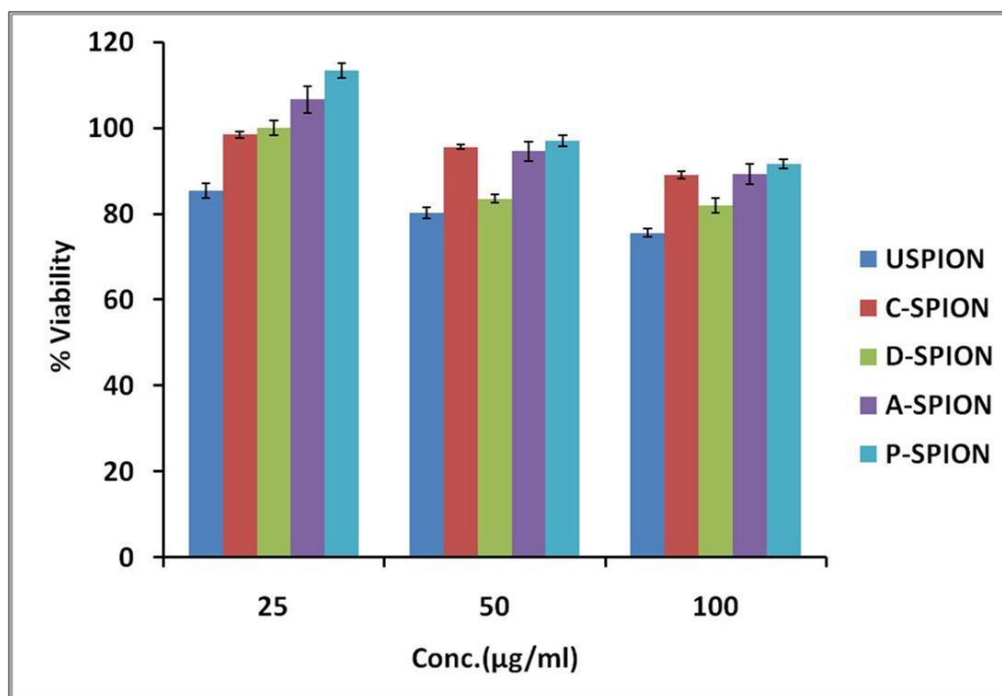


Figure - 23. Percentage cell viability determined by MTT assay against different concentrations.

4.1.6.2 Cell uptake efficiency

The cellular uptake and labeling efficiency of C-SPIONs, D-SPIONs, A-SPIONs and P-SPIONs are shown in Figure – 24(b-e) and is compared with the control without any particles (Figure – 24a). On iron specific PB staining, the SPIONs appears bluish in colour. Cell uptake of all the SPIONs are clear on PB staining. Moreover, the images gives an indication that the particles are mostly concentrated in the cytoplasm. The normal morphology of the cells were found to remain undisturbed on 24 hr incubation with the particles, indicating that all the SPIONs are cell friendly.

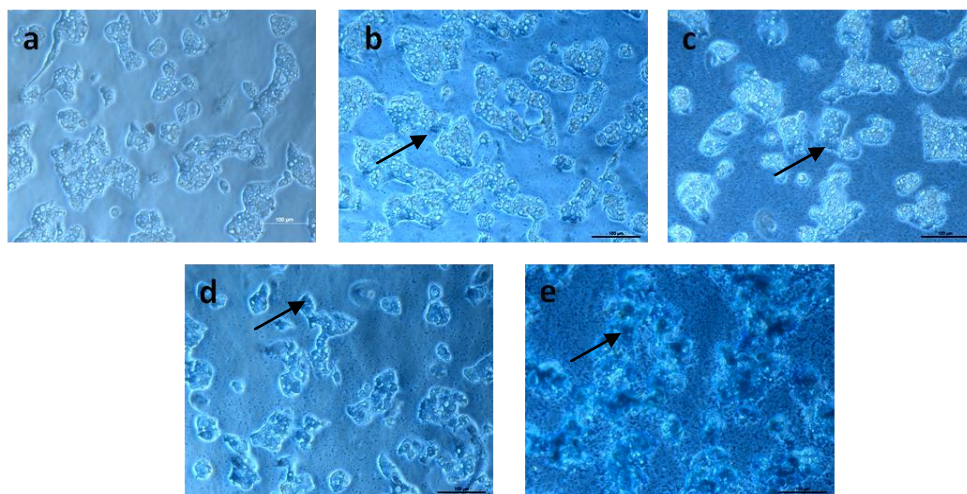


Figure - 24. Microscopic visualization of cell uptake of C-SPIONs, D- SPIONs, A-SPIONs, P-SPIONs (b-e) and control without USPIONs (a) on Prussian Blue staining.

The blue tinges represents the presence of SPION.

4.1.7 *In vivo* studies

4.1.7.1 *Animal Model Development for liver fibrosis*

For demonstrating *in vivo* liver uptake potential and MR imaging efficiency of all the surface modified SPIONs, animal model of liver fibrosis was developed in adult rats. The development of animal model for liver fibrosis was confirmed by monitoring the

liver transaminases SGPT and SGOT levels, which are biomarkers over expressed in the blood due to liver injury. At the end of sixth week, these markers were significantly high in fibrosis induced animals compared to control animals (Figure - 25) which confirmed the liver fibrosis model development.

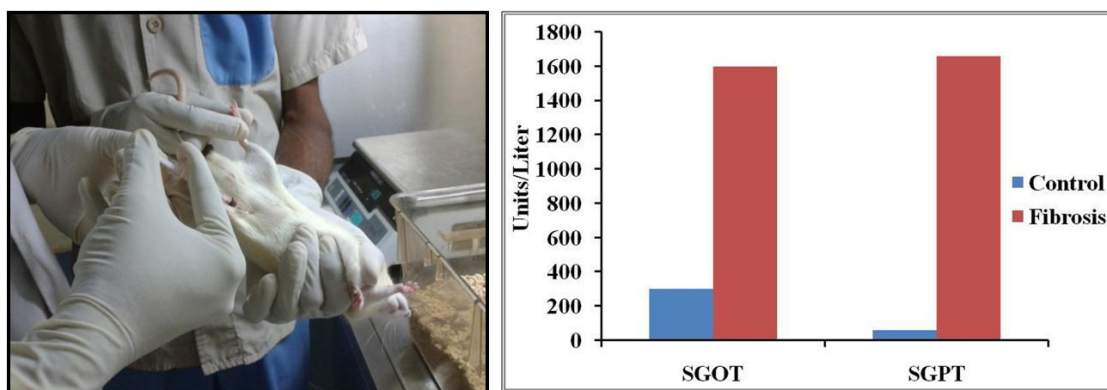
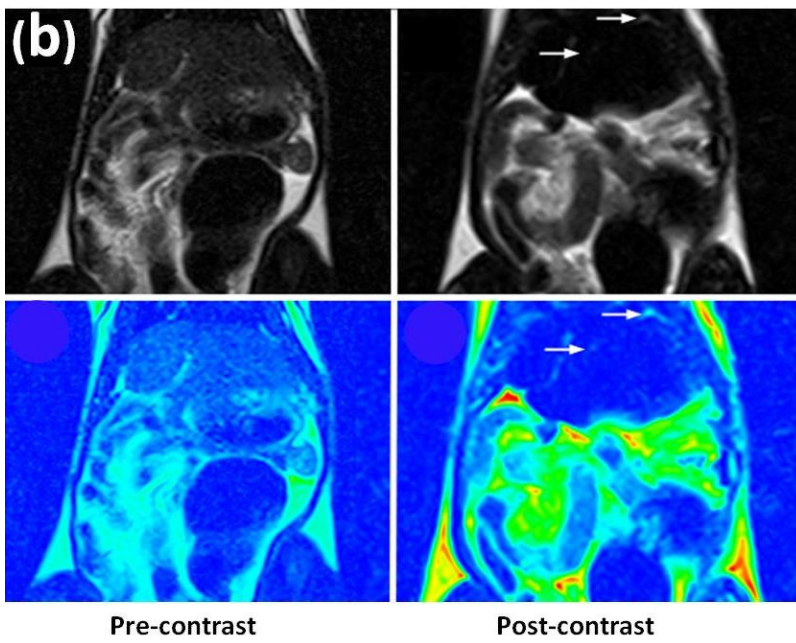
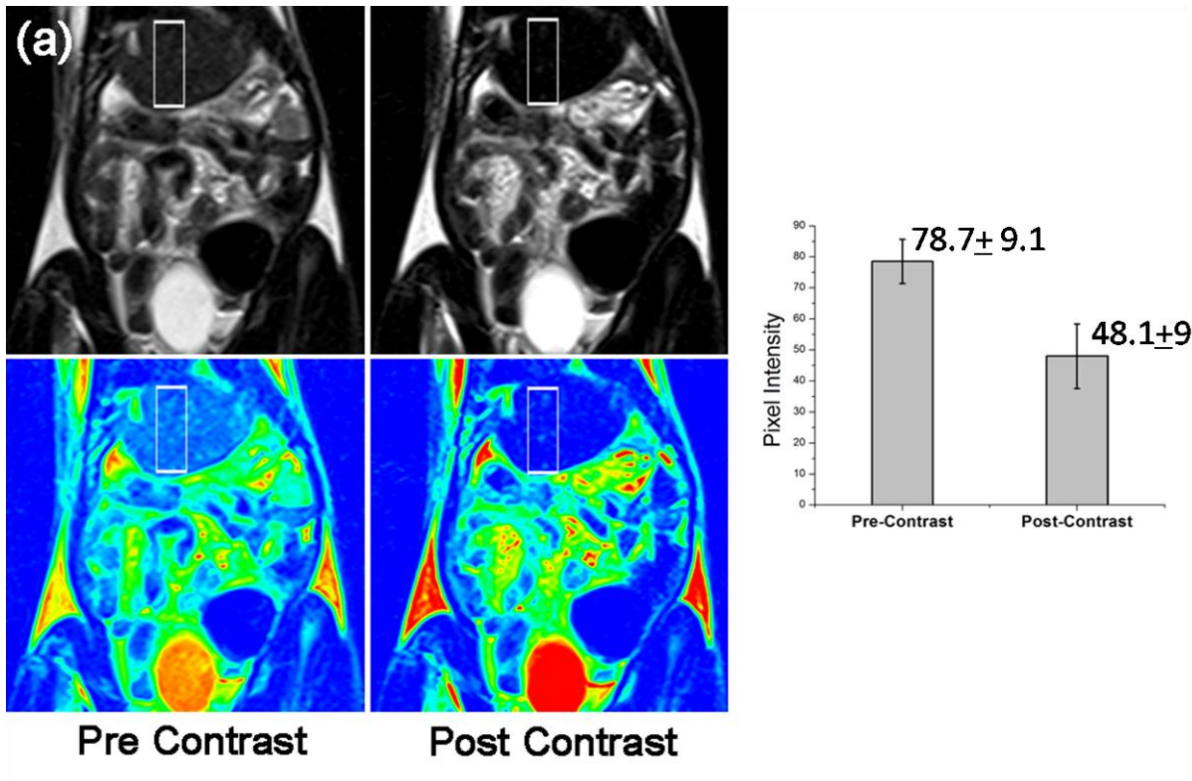


Figure – 25. Photograph of intraperitoneal administration of CCl_4 : Olive oil to induce liver fibrosis(left) and SGOT and SGPT levels of fibrosis induced and control rat model (right).

4.1.7.2 *In vivo* MRI measurements

Selected rodent models based on their SGOT and SGPT levels were anesthetized and imaged using a 1.5 T MRI scanner. Pre and post contrast T_2 weighted coronal images and corresponding pseudo coloured images of the liver fibrosis induced animals are shown in Figure – 26(a–d). All the four SPIONs based nanoprobe enhances the image contrast of tissues through considerable shortening of T_2 relaxation times. This shortening of T_2 relaxation leads to signal drop with the decrease in the pixel intensity at the sites where the SPIONs are accumulated. Average pixel intensity variation from the pre and post contrast liver also gives a remarkable difference between the two.



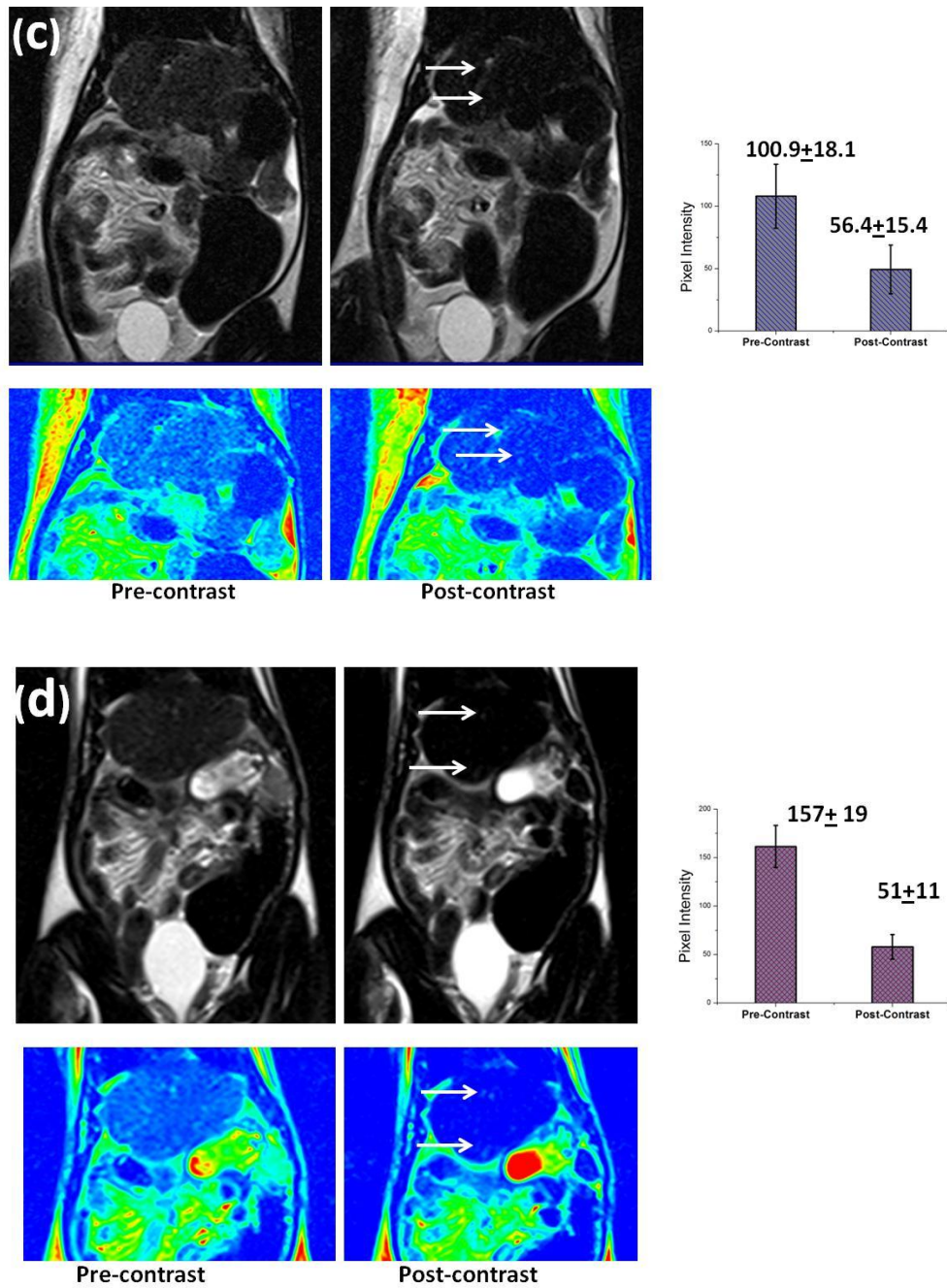


Figure – 26. Pre and post contrast *in vivo* MR images and corresponding pseudo coloured images (left) and the percentage signal intensity variation from pre to post contrast MR image (right) of liver fibrosis rat model administered with (a) C-SPIONs (b) D-SPIONs (c) A-SPIONs and (d) P-SPIONs.

Post-contrast MR images acquired within 10–15 min of the administration of respective SPIONs showed hypointense liver compared to pre-contrast images. The estimated average signal intensity in the MR images of the animals administered with C-SPIONs, was 78.89 ± 9.1 and 48.09 ± 9.5 respectively for pre- and post-contrast liver images with a decrease in percentage signal intensity of 39%. For D-SPIONs, the average signal intensity varied from 80.7 ± 11.6 for pre-contrast to 36.24 ± 9.44 for post-contrast images with a 55% decrease, which is very well appreciated with naked eye without any further image processing. A-SPION administration provided an average signal intensity variation from 100.9 ± 18.1 to 56.4 ± 15.4 for pre to post contrast MR images with 44% decrease. The average SI values varied from 157 ± 19 to 51 ± 11 for pre to post contrast images with 67% decrease providing a remarkable contrast enhancement on P-SPION administration. Under detailed inspection of the MR image, the presence of few streaky linear hyperintense areas can also be visualized in the hypointense liver indicating the fibrotic regions in the affected liver. The hypointensity observed in the post-contrast T₂ weighted MR image is due to the heavy uptake of SPIONs by the liver cells. Within the hypointense liver, hyperintense streaks visualized, represents the Kupffer's cell devoid fibrotic regions of the liver. Identification of this fibrotic lesions with the help of developed probes helps in the easy and early diagnosis of liver fibrosis using these nanoprobe as MRI contrast agents.

4.1.8 Histopathological Analysis

The fibrotic and normal liver sections were evaluated pathologically by H&E, MT and PB staining procedures. H&E stained sections of fibrosed liver reveals

moderate to severe necrosis of hepatocytes with infiltration of mononuclear cells, perlobular fibrosis and portal triad fibrosis. Collagen specific MT stained sections shows collagen fibres in the fibrosed areas (Figure – 27(a-e)) which ascertained the development of liver fibrosis in the rodent model. The presence of iron in the liver macrophages was clear on the iron specific PB stained images of liver sections (Figure – 28(a-e)).



normal liver



fibrosed liver

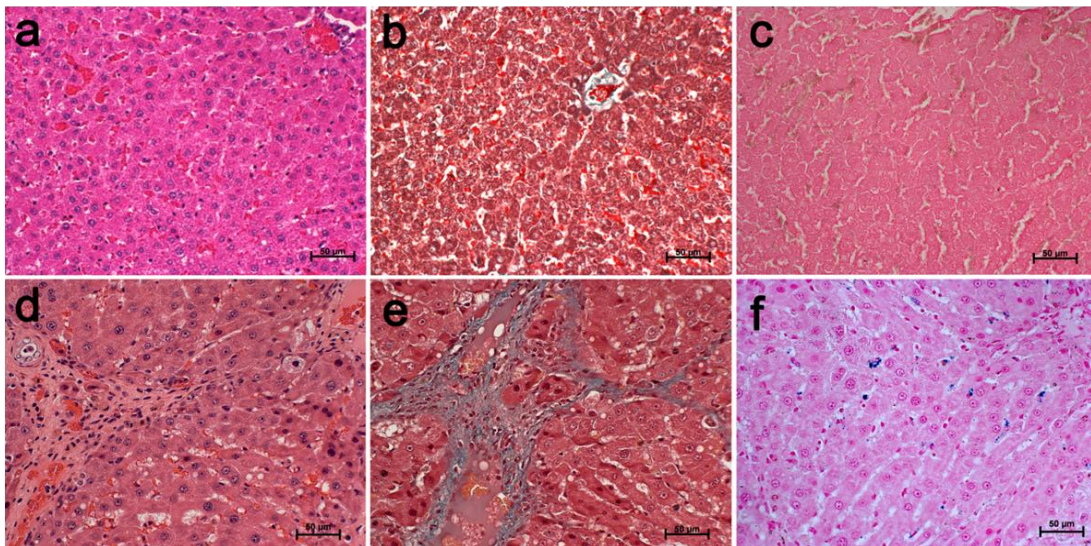


Figure – 27. H&E (a,d), MT (b,e) & PB (c,f) stained histopathological images of normal liver and fibrosed rat liver administered with SPIONs probe. Photograph of normal (left) and fibrosed (right) liver is shown on the top.

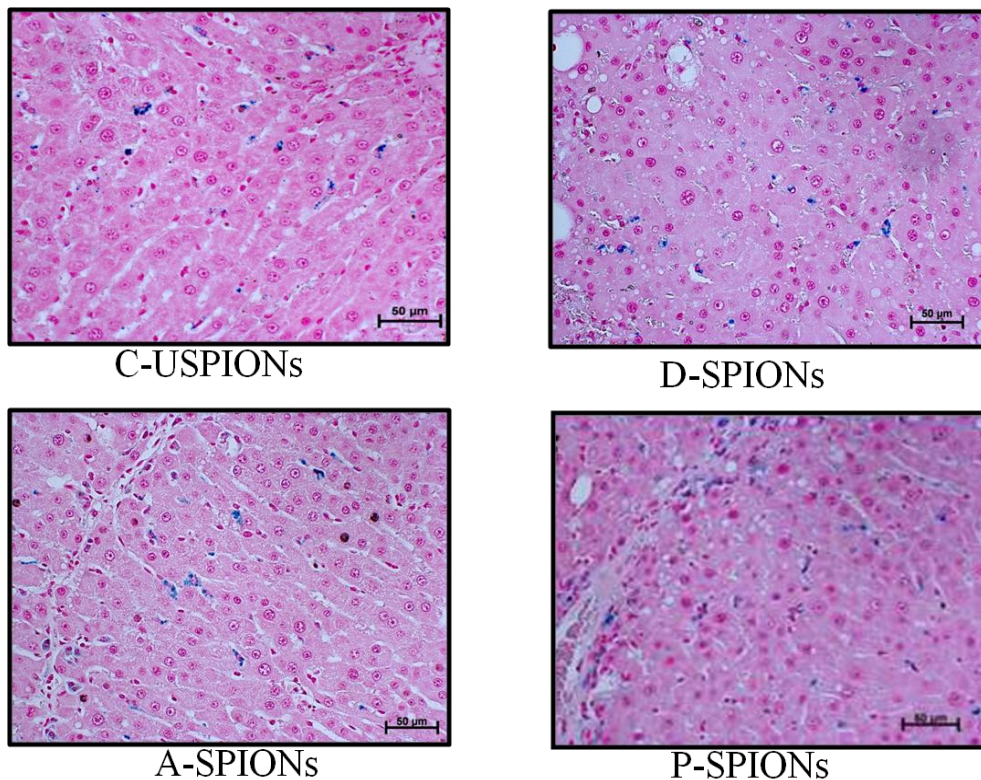


Figure – 28. PB stained histopathological images of fibrosed liver in the case of C-SPIONs, D-SPIONs, A-SPIONs and P-SPIONs administration.

4.2 Preparation of Multimodal nanoprobes

Multimodal nanoprobes were prepared by incorporating NIR emitting dye, Atto 700 with D-SPION, A-SPION and P-SPION by physical interaction. Simple electrostatic interaction of the hydroxyl groups of SPIONs and activated COO⁻ group of Atto 700 dye resulted in the DSPION-AT, ASPION-AT and PSPION-AT (Figure – 29).

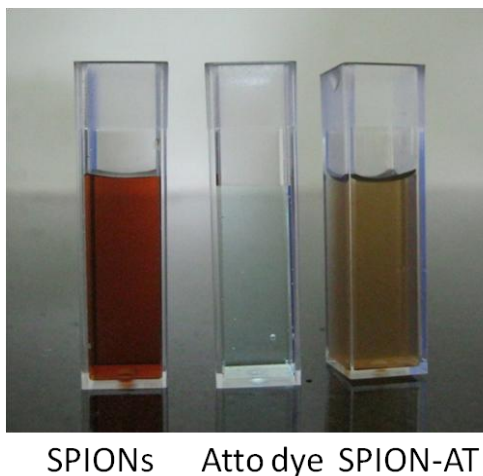
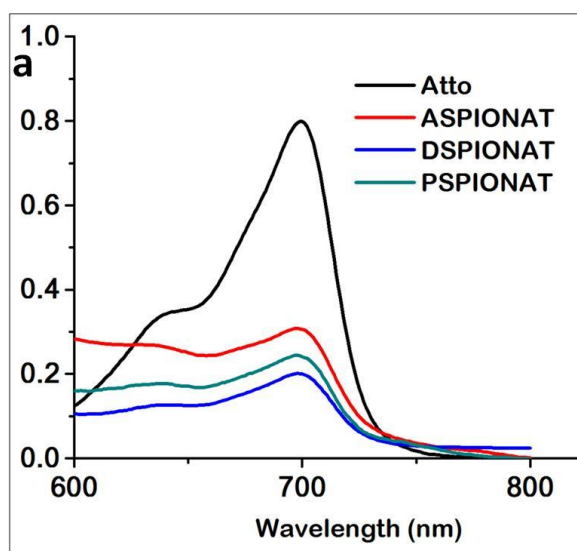


Figure - 29. Photographic image of SPION-AT in aqueous solution.
4.2.1 Optical Characterization

The UV-Vis spectra of DSPION-AT, ASPION-AT and PSPION-AT showed an absorption peak around 700 nm (Figure – 30a). The fluorescence spectra of DSPIONs-AT, ASPIONs-AT and PSPIONs-AT showed an excitation maxima at 680 nm and an emission maxima at 712 nm (Figure – 30b,c).



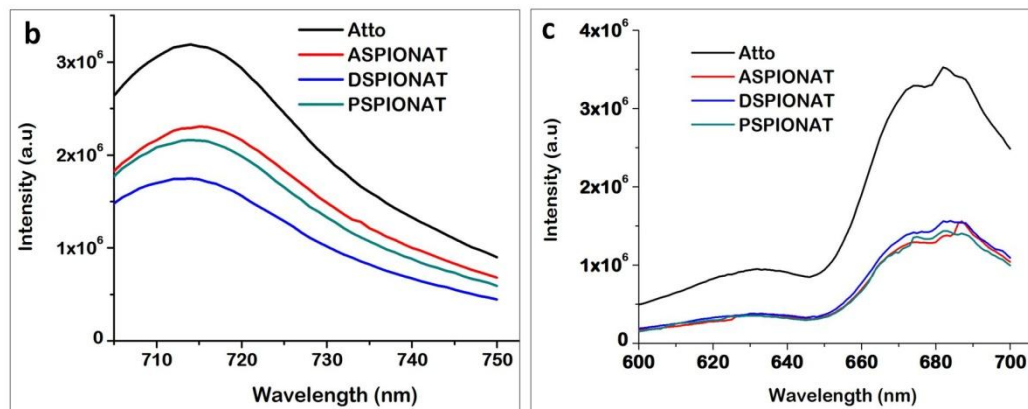


Figure - 30. Optical properties of multimodal nanoprobe: (a) UV-Vis absorption spectra (b) Excitation and (c) Emission Spectra of DSPION-AT, ASPION-AT and PSPION-AT compared with the Atto dye.

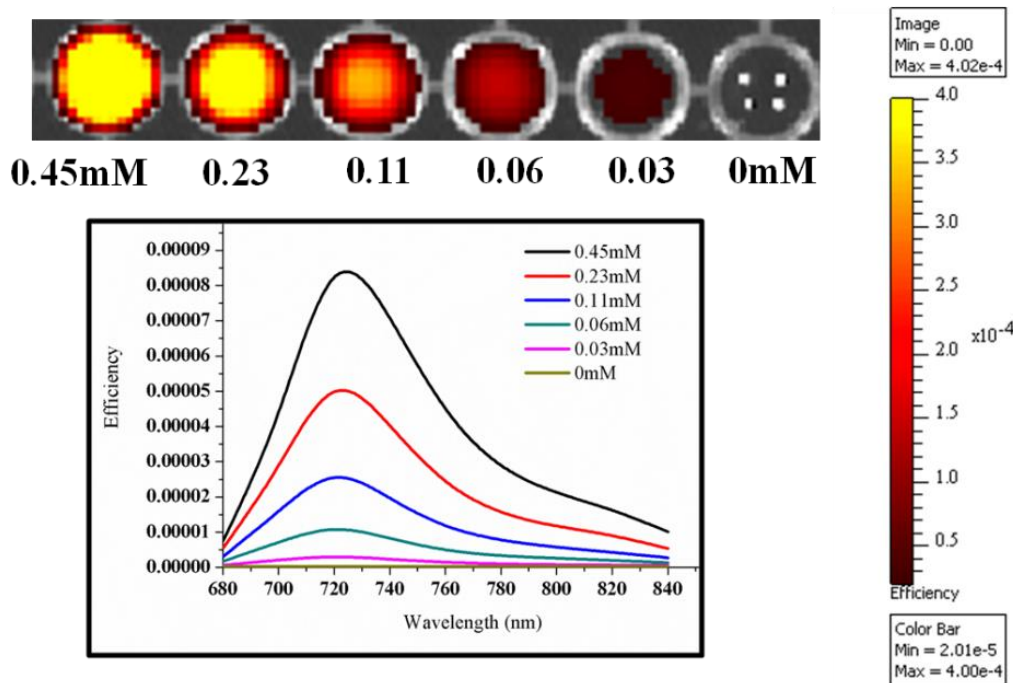


Figure - 31. Fluorescence images (above) and the corresponding spectra of DSPION-AT with varying concentration excited at 675 nm with emission at 710 nm. The bar on the right gives an indication about the efficiency of the probe

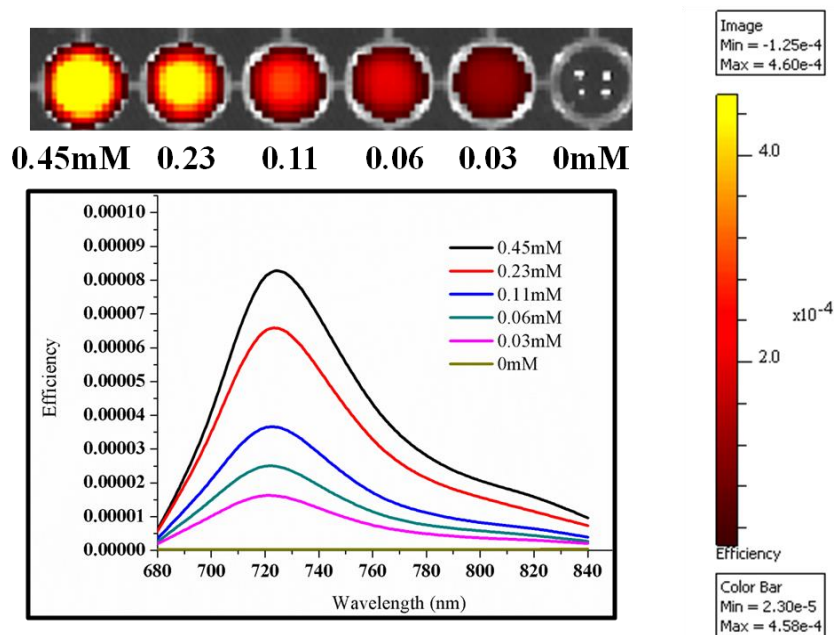


Figure - 32. Fluorescence images (above) and the corresponding spectra of ASPION-AT with varying concentration excited at 675 nm with emission at 710 nm. The bar on the right gives an indication about the efficiency of the probe

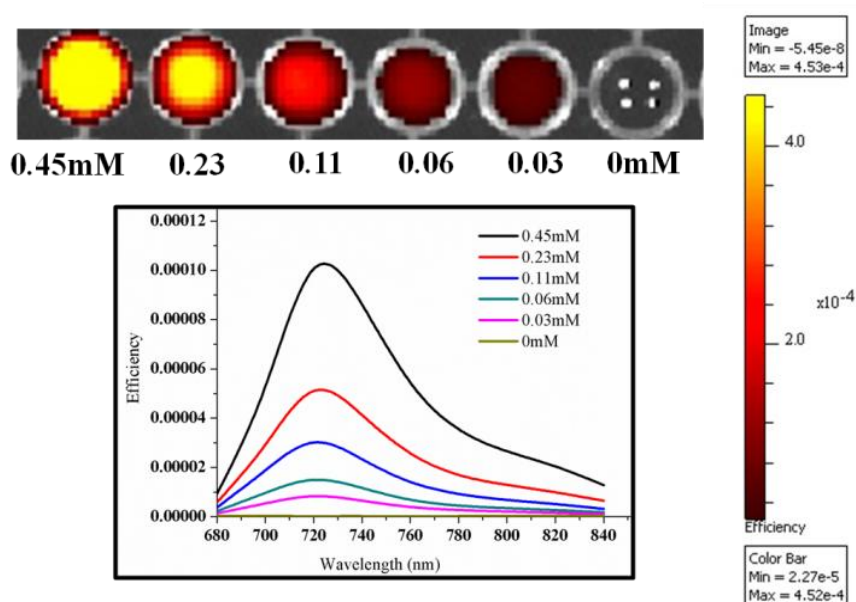


Figure - 33. Fluorescence images (above) and the corresponding spectra of DSPION-AT with varying concentration excited at 675 nm with emission at 710 nm. The bar on the right gives an indication about the efficiency of the probe

The concentration dependent optical imaging efficiency of DSPION-AT, ASPION-AT and PSPION-AT using *in vivo* optical imaging system are shown in Figure – (31-33). The excitation - emission – efficiency contour plots for the corresponding excitation – emission imaging are also shown in Figure – 34.

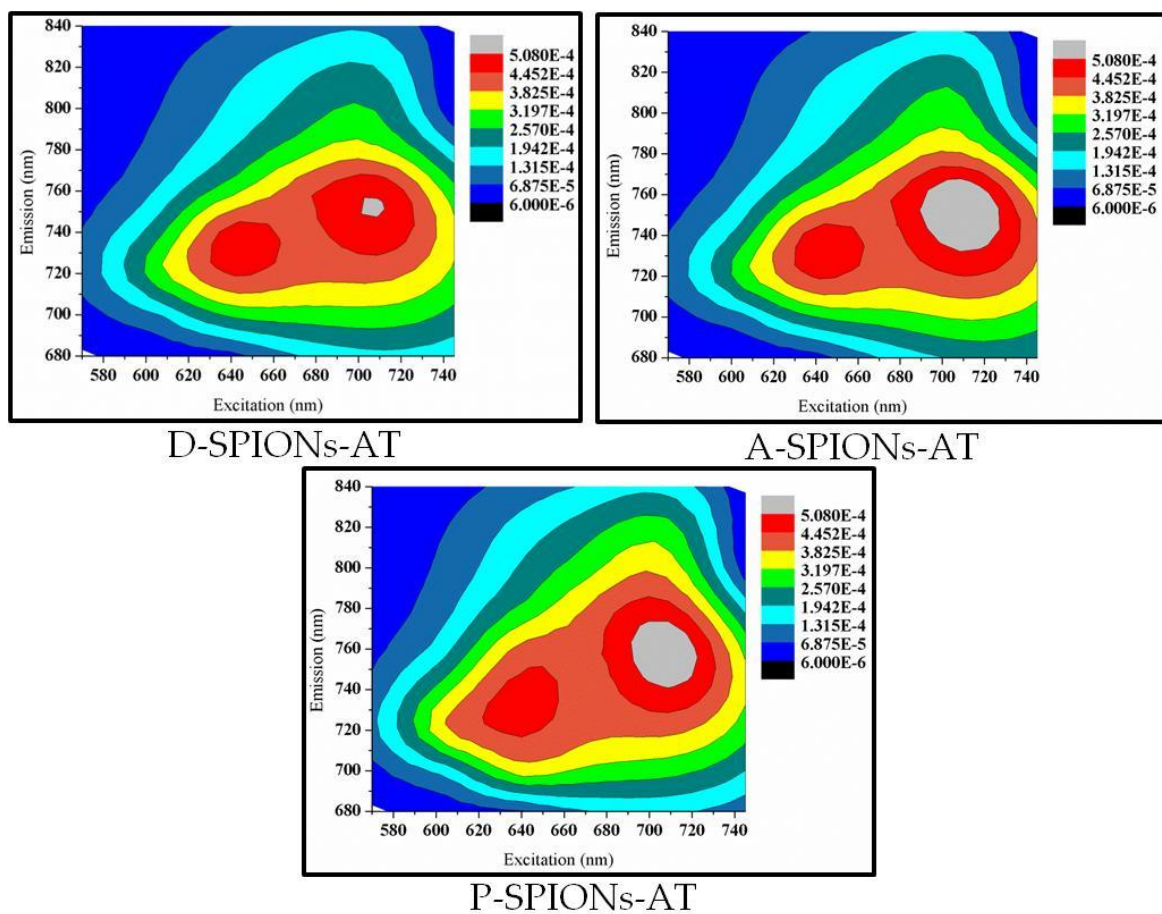


Figure – 34. Excitation-Emission-Efficiency contour plots of DSPION-AT, ASPION-AT and PSPION-AT. The bar on the right gives an indication about the efficiency of the probe.

The contour plots showed the maximum fluorescence efficiency around 720 – 760 nm emission range when excited at 720 nm. Considering all the three plots, ASPION-AT

showed maximum efficiency in the wide range of excitation-emission, indicated by the area of the grey region at the center of the plot whereas, DSPION-AT showed maximum efficiency in a narrow emission range around 750 nm.

4.2.2 *In vivo* Optical imaging of multimodal nanoprobe.

The imaging efficiency of the developed multimodal nanoprobe were evaluated in the mouse model of liver fibrosis. Development of liver fibrosis was indicated by the LFT and the animals with elevated level of liver specific enzymes, SGOT and SGPT corresponding to the fibrosed state were selected for imaging (Figure-35).

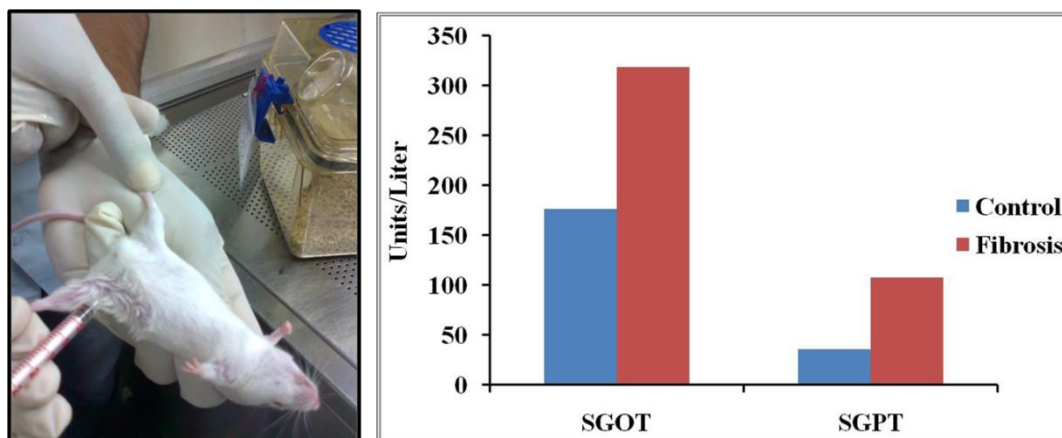
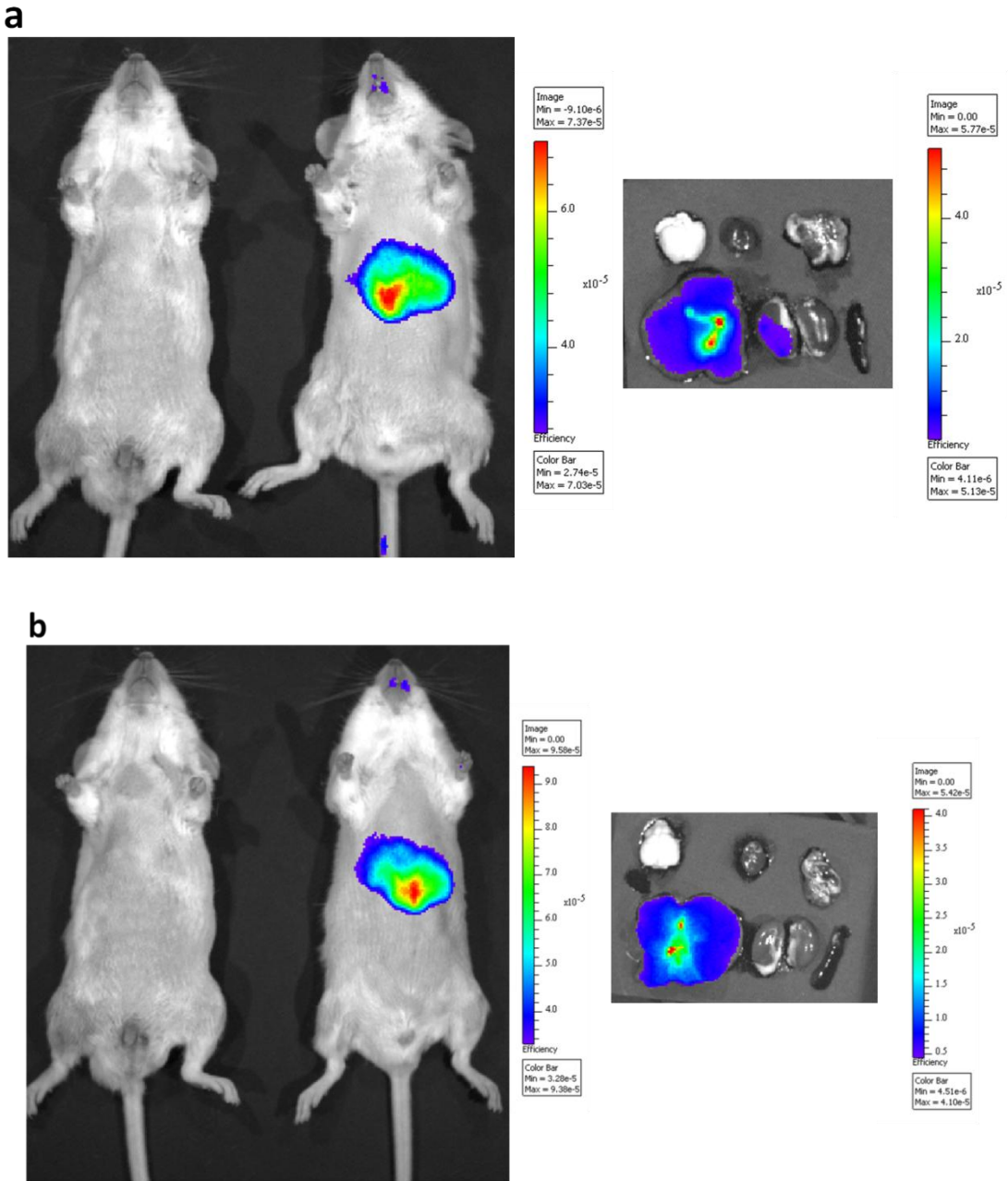


Figure – 35. Photograph of intraperitoneal administration of CCl₄ : Olive oil to induce liver fibrosis (left) and SGOT and SGPT levels of fibrosis induced and control mice model (right).

DSPION-AT, ASPION-AT and PSPION-AT administered rodents were imaged after 20 minutes of intravenous administration. In each case, an elevated fluorescence signal intensity was observed from the liver of the fibrosis induced mice compared to the control mice kept aside for comparison. The organs of each mouse were excised after 1 hr for visualizing the biodistribution of the nanoprobe and have seen high fluorescence

intensity in the liver (Figure – 36(a-c)). Mild signal is also observed from the kidney in the case of DSPION-AT indicating the quicker clearance of this probe compared to the other two.



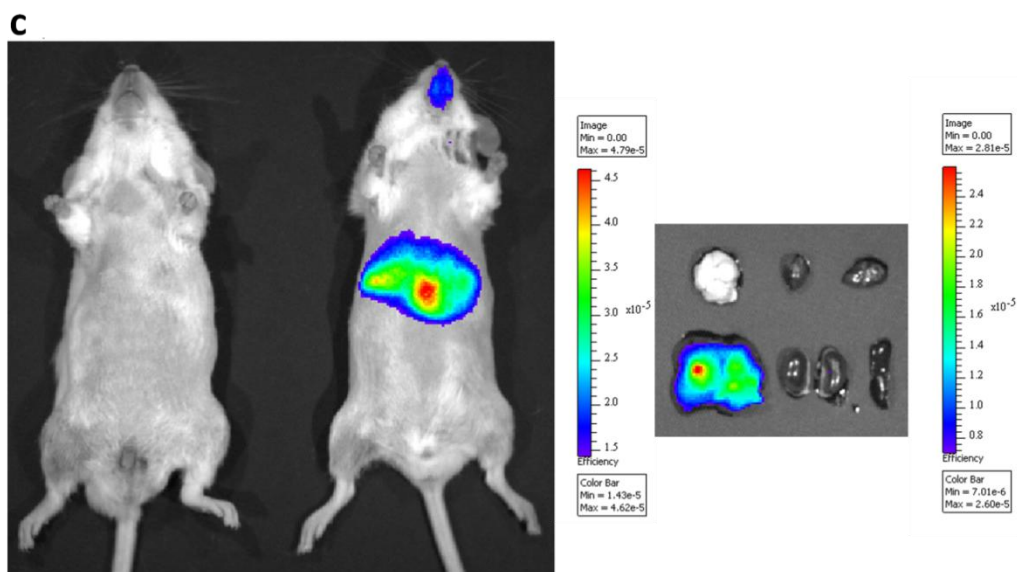


Figure – 36. *In vivo* optical images of control and fibrosis induced mice model administered with (a) DSPION-AT, (b) ASPION-AT and (c) PSPION-AT. The *ex vivo* fluorescence images of the organs on the right. The bar on the right gives an indication about the efficiency of the probe

4.3 Hybrid nanoprobes using Gold Clusters and SPIONs

4.3.1 Synthesis of Hybrid Nanomaterial (ASPION-Au)

BSA stabilized gold nanocluster was conjugated to ASPIONs taking advantage of the additional functional groups available for conjugation in this case. The Au cluster with amine groups was then conjugated with ASPIONs through EDC chemistry resulting in ASPION-Au.

4.3.2 Physico-Chemical & Magnetic Characterization.

4.3.2.1 Determination of Particle Size

The uniform size distribution and nearly spherical morphology of the Au clusters with a size distribution of around 1-2 nm is observed from the TEM micrograph (Figure – 37a).

The ASPION-Au showed an average particle size of around 20 nm (Figure – 37b).

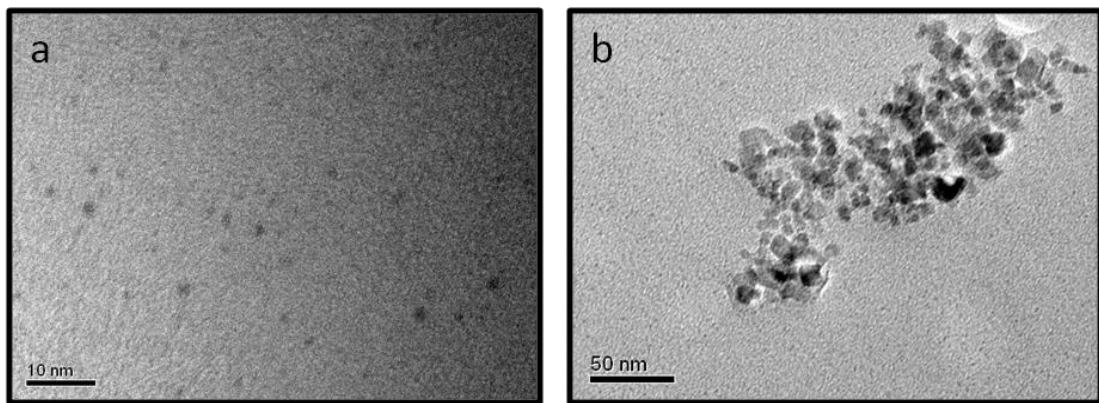


Figure-37. TEM Micrograph of (a) Au cluster and (b) ASPION-Au.

4.3.2.2 Results of X-ray Diffraction studies (XRD)

A broad band is observed at 44.15° (2θ) in the XRD pattern of Au clusters. The ASPION-Au XRD pattern showed both the inverse spinel structure of magnetite with the indices (1 1 1), (2 2 0), (3 1 1), (2 2 2), (4 0 0), (4 2 2), (5 1 1) and (4 4 0) as per the JCPDS Card No. 89-0691 along with the broadness of Au clusters (Figure – 38).

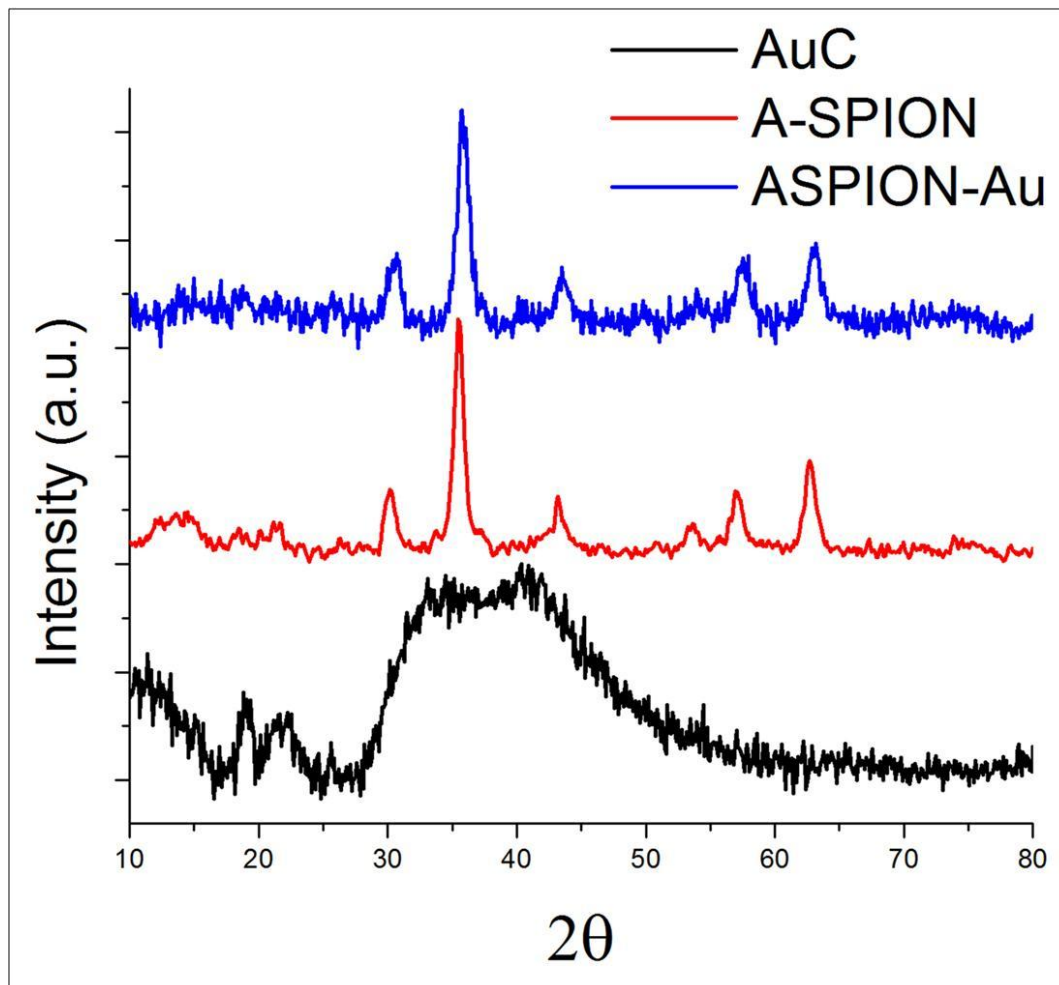


Figure - 38. XRD pattern of ASPION-Au, ASPION and Au cluster.

4.3.2.3 Fourier Transform Infra-red spectroscopy (FT-IR)

The FTIR spectra of BSA Au cluster showed bands at 3451 cm^{-1} , 1653 cm^{-1} and 1393 cm^{-1} . A-SPIONs exhibited bands around 3361 , 1621 , 1413 , 1060 and 582 cm^{-1} . The FTIR spectra of ASPION-Au showed both the vibrations of Au-BSA and the Fe-O bond with minor shifts in the corresponding bands (Figure – 39).

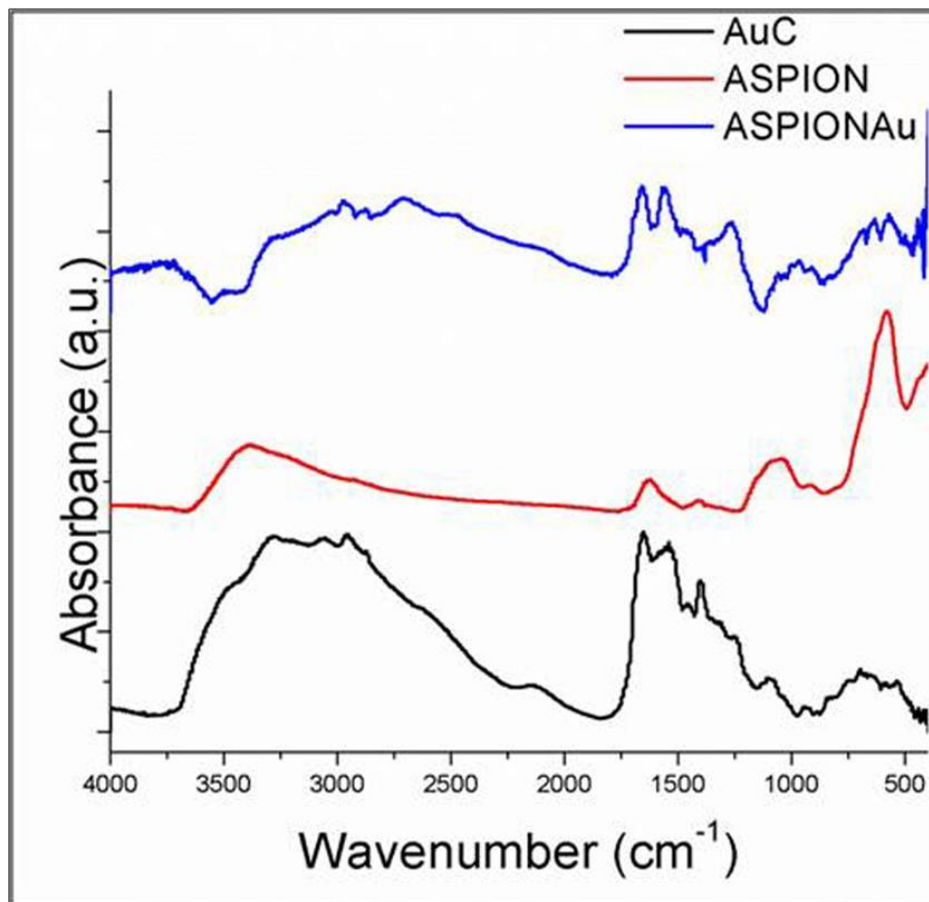


Figure - 39. FTIR spectra of ASPION-Au compared with ASPION and Au cluster.

4.3.2.4 Magnetic Property

The magnetic hysteresis loop of ASPIONs-Au retained the superparamagnetic property of the SPIONs with a decrease in the magnetic saturation to 4.9 emu/g (Figure – 40). The decrease in the saturation value may be due to the presence of BSA stabilized Au cluster whose magnetic properties are expected to be very weak (Qin *et al.*, 2014).

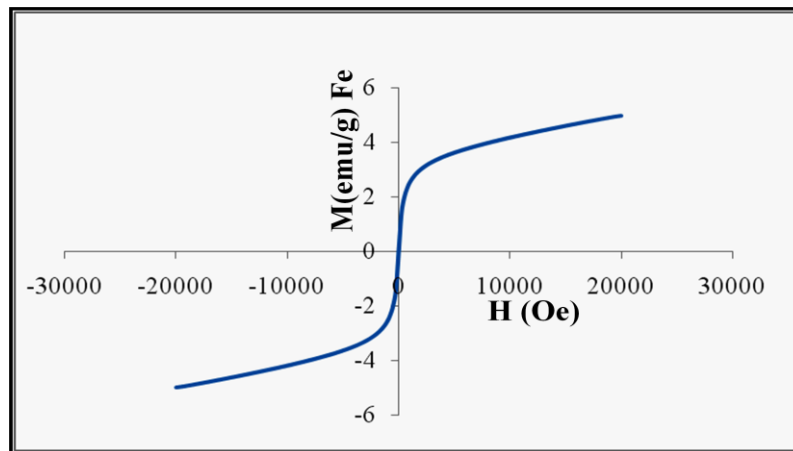


Figure - 40. Magnetization curve (M-H) of ASPION-Au.

4.3.2.5 Magnetic Relaxivity

The effect of ASPION-Au on the T_1 and T_2 proton relaxation was evaluated and the r_1 and r_2 relaxation rates were calculated from the relaxation plots. The r_2 and r_1 values were found to be 4.673 and 0.9084 $\text{mM}^{-1}\text{s}^{-1}$ respectively (Figure – 41). Thereby the relaxation ratio, r_2/r_1 falls to 5.1. This notably small r_2/r_1 ratio is not fully understood; perhaps the architecture of the ASPION-Au may have contributed to this phenomenon.

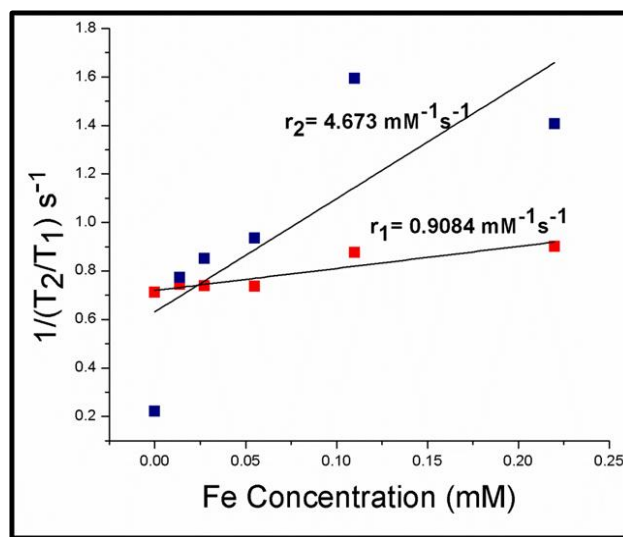


Figure -41. Longitudinal (r_1) and Transverse relaxation rates (r_2) of ASPION-Au.

4.3.3 Optical Characterization

Au cluster as well as ASPION-Au showed absorbance around 510 nm and 552 nm respectively. The emission was found to center at 675 nm with a shoulder at 640 nm on 510 nm excitation with slight shift in the ASPION-Au spectra (Figure – 42).

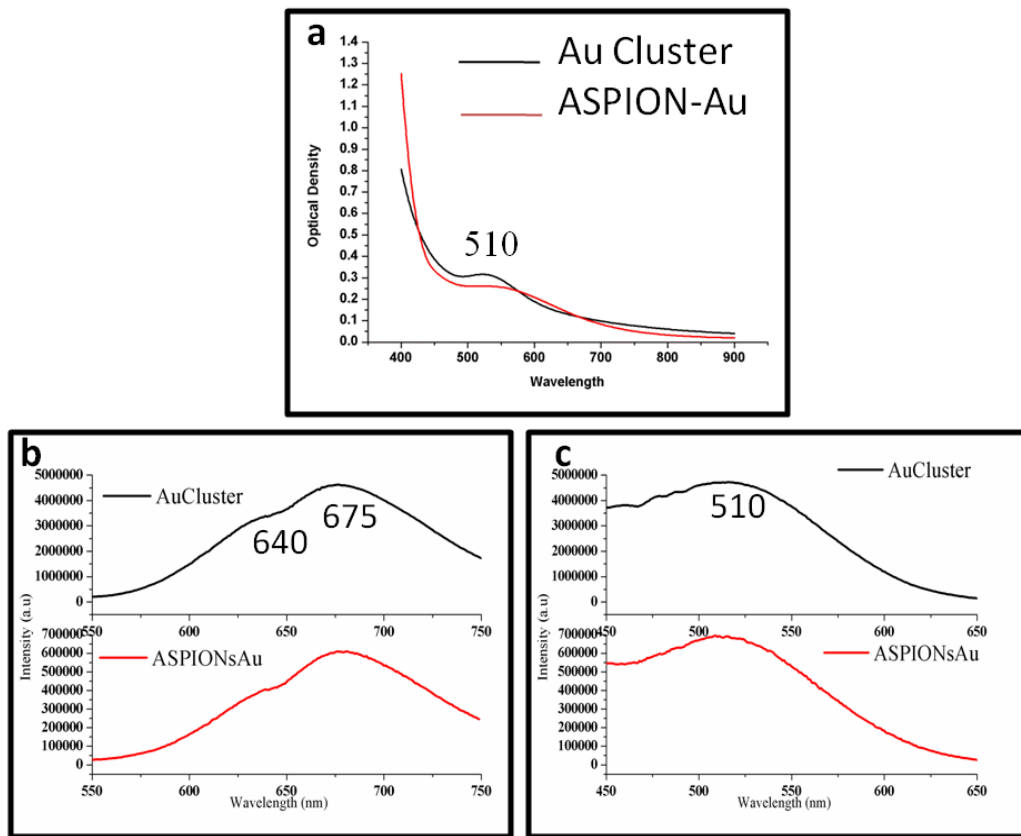


Figure- 42. Optical properties of Hybrid nanoprobe, ASPION-Au: (a)UV-Vis absorption spectra (b) Excitation and (c) Emission Spectra compared with Au cluster. The optical imaging efficiency of Au clusters and ASPION-Au evaluated using the Xenogen IVIS system has shown an efficiency of 1.49×10^{-4} and 1.27×10^{-5} (Figure – 43). The excitation-emission-efficiency contour plots for the corresponding excitation–emission imaging are shown in Figure – 44. The efficiency difference of Au clusters and

ASPION-Au to the power of ten restricts the comparison of both contours. But the shift in the highest efficiency emission range from 660-710 nm to 710-760 nm showed the ASPION-Au conjugation.

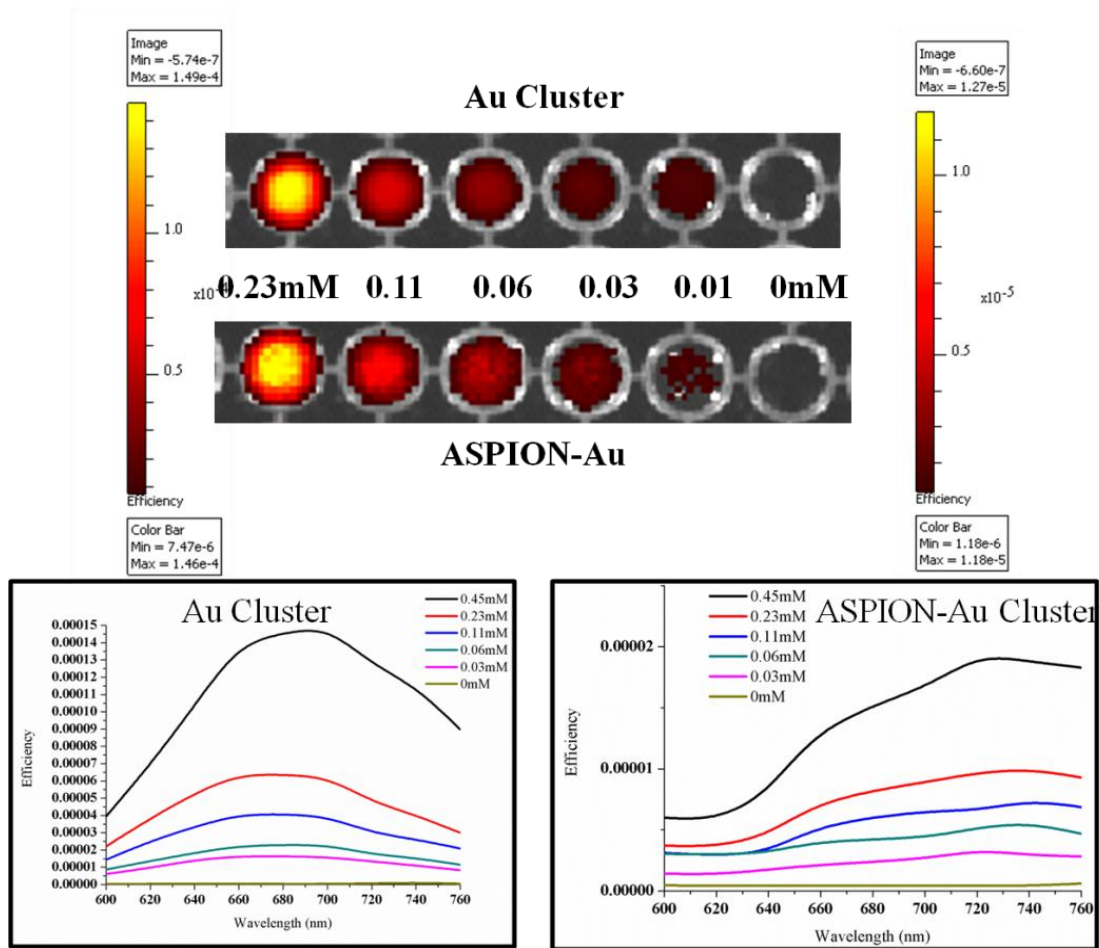


Figure-43. Fluorescence images and the corresponding spectra of ASPION-Au and Au cluster with varying concentrations (Excitation at 465 nm and Emission at 680 nm). The bar on the right(Au cluster) and left (ASPION-Au) gives an indication about the efficiency of the probe.

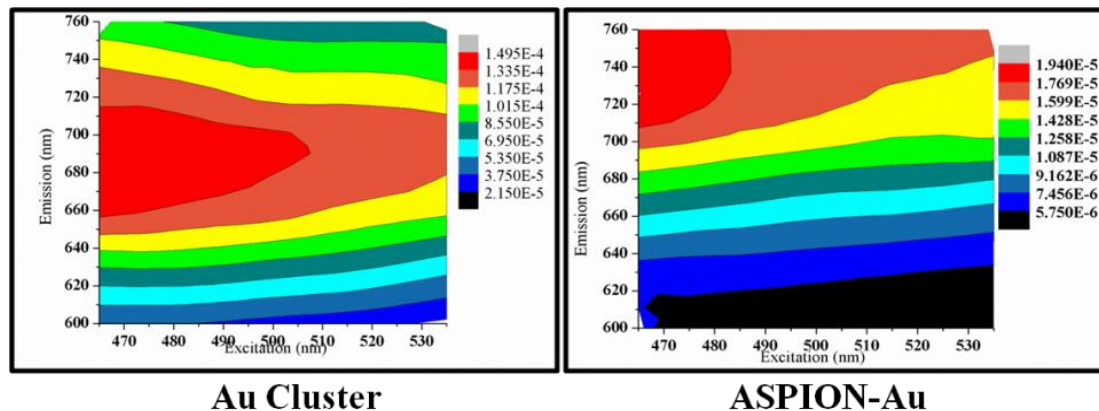


Figure – 44. Excitation-Emission-Efficiency contour plots of ASPION-Au and Au cluster. The bar on the right gives an indication about the efficiency of the probe.

4.3.4 Hemocompatibility Evaluation

The aggregation and hemolysis study of AuC and ASPION-Au proved the hemocompatible nature of the particles (Figure-45). No aggregation was observed when compared to the positive control PEI. Lysis was also in the acceptable range of less than 1%.

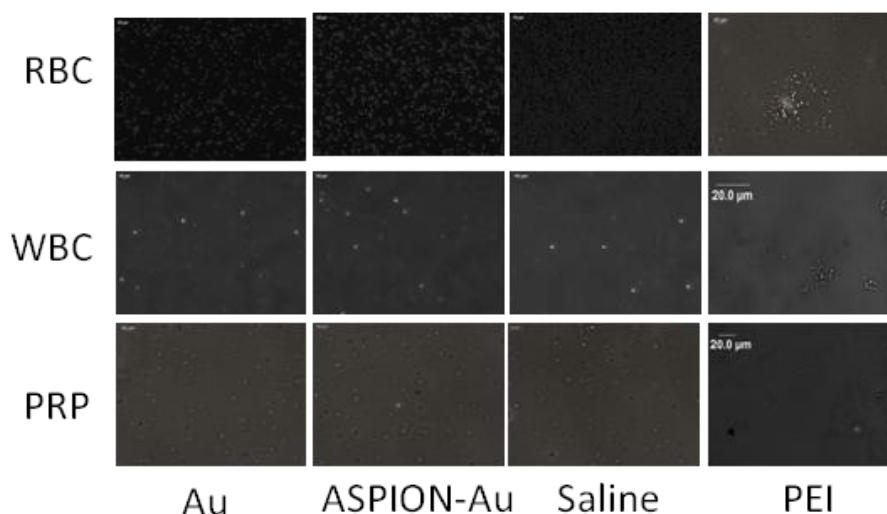


Figure -45. Blood aggregation studies: RBCs, WBC's and platelets incubated with ASPION-Au, Au cluster, positive control, PEI and negative control, saline.

4.3.5 Cell culture studies

4.3.5.1 Cytotoxicity assessment

The cytotoxicity evaluation of the Au cluster and ASPION-Au resulted in 97 -110 % and 91 -101 % viability for concentrations ranging from 100 – 25 $\mu\text{g/ml}$ (Figure-46). The cytocompatibility of the hybrid nanoprobe is evident from the percentage viability of cells which was found to be greater than 90% for a higher concentration of 100 $\mu\text{g/ml}$.

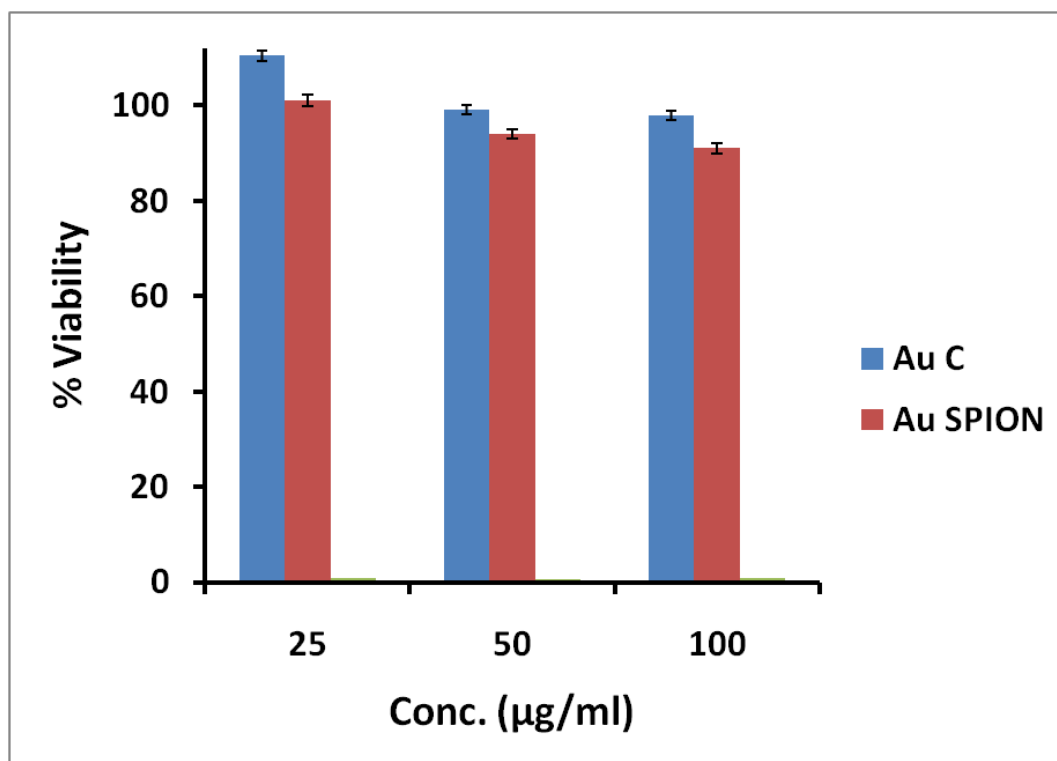


Figure - 46. Percentage viability of cells against different concentrations determined by MTT assay.

4.4 Hybrid nanoprobes using Carbon dots and SPIONs

4.4.1 Synthesis of Hybrid Nanomaterial (ASPION-CDTS & PSPION-CDTS)

Carbon dots (CDTS) were prepared by the carbonization process through the self catalytic reaction of AC, P₂O₅ and water. The as prepared CDTS were diluted and centrifuged and conjugated with ASPIONs and PSPIONs separately. The ASPION-CDTS were prepared by the conjugation of COO⁻ group of ASPIONs with one of the NH⁺ group of diamino PEG. The excess NH⁺ group of diamino PEG was then conjugated to the COO⁻ group of CDTS. The PSPION-CDTS were prepared by the electrostatic interaction of PSPIONs and CDTS. The ASPION-CDTS and PSPION-CDTS prepared served as hybrid nanoprobes for multimodal imaging.

4.4.2 Physico-Chemical & Magnetic Characterization.

4.4.2.1 Determination of Particle Size

The TEM images demonstrated spherical morphology with an average particle size of 7 nm for CDTS. A honeycomb like architecture and an average size of 20 and 90 nm was observed for ASPION-CDTS and PSPION-CDTS respectively (Figure – 47). The core-shell like structure can be visualized in the TEM images of ASPION-CDTS and PSPION-CDTS.

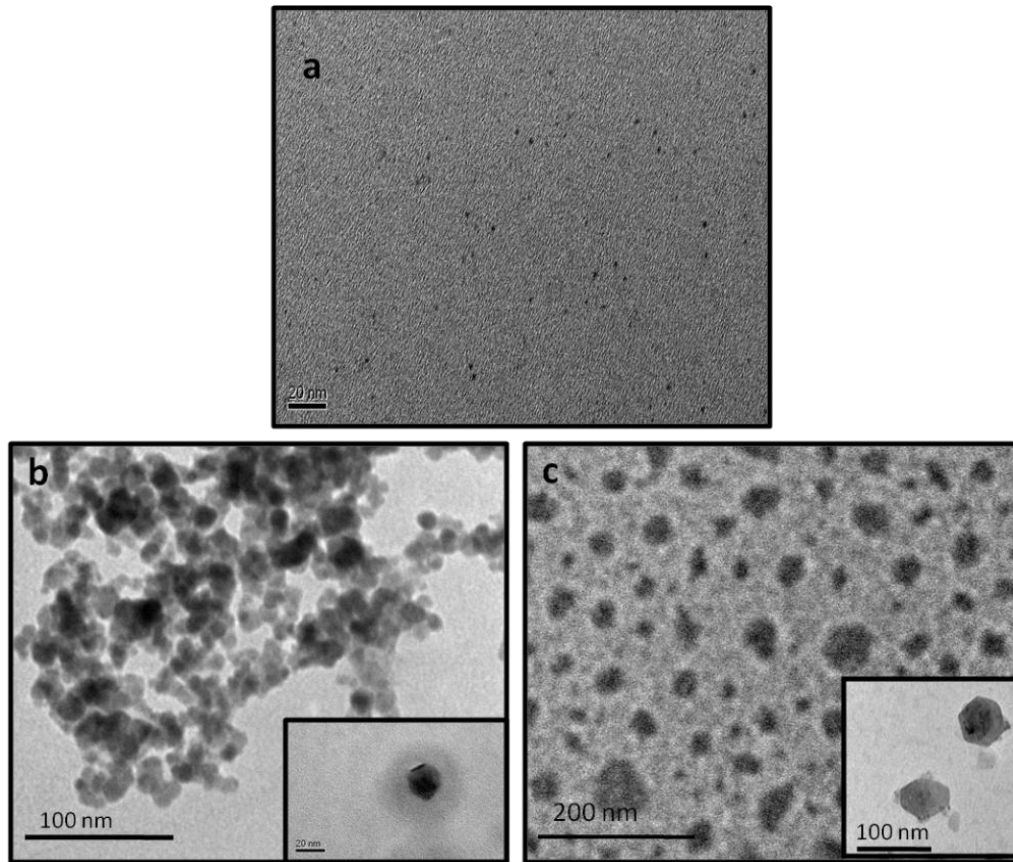


Figure - 47. TEM Micrographic images of (a) CDTS (scale bar – 20 nm) (b) ASPION-CDTS(scale bar – 100 nm) and (c) PSPION-CDTS(scale bar – 200 nm).

4.4.2.2 Results of X-ray Diffraction studies (XRD)

The XRD pattern of the CDTS reflects one diffraction peak at 24.6° corresponding to (002) plane. The XRD patterns of PSPION-CDTS and the ASPION-CDTS exhibits all the corresponding diffraction peaks of PSPIONs and ASPIONs along with the peak of CDTS with slight broadening (Figure – 48).

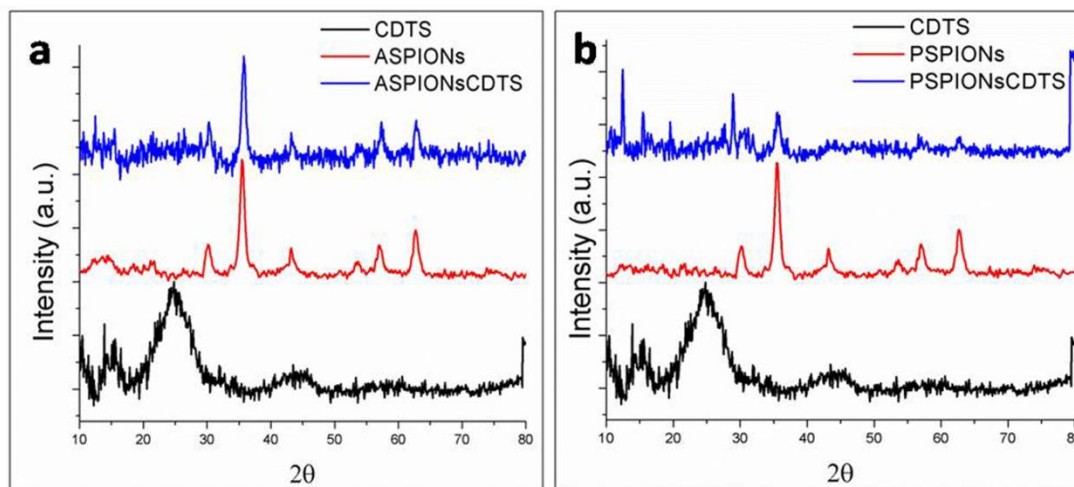


Figure - 48. XRD pattern of (a) ASPION-CDTS, ASPION and CDTS and (b) PSPION-CDTS, PSPION and CDTS.

4.4.2.3 Fourier Transform Infra-red spectroscopy (FT-IR)

FTIR spectra of CDTS showed bands around 3067, 1653, 1581, 1391 and 998 cm^{-1} whereas A-SPIONs exhibited bands around 3361, 1621, 1413, 1060 and 582 cm^{-1} and P-SPIONs at 3378, 1616, 1408, 1025, and 568 cm^{-1} . On conjugation with ASPIONs the corresponding IR bands of ASPION-CDTS were observed at around 3399, 2818, 1605, 1512, 1408, 1296, 1046, 890 and 567 cm^{-1} and PSPION-CDTS at 3098, 1653, 1591, 1404, 1061 and 520 cm^{-1} (Figure – 49). The shift in the corresponding bands can be observed in the ASPION-CDTS and PSPION-CDTS on comparison with the bands of ASPIONs, PSPIONs and CDTS.

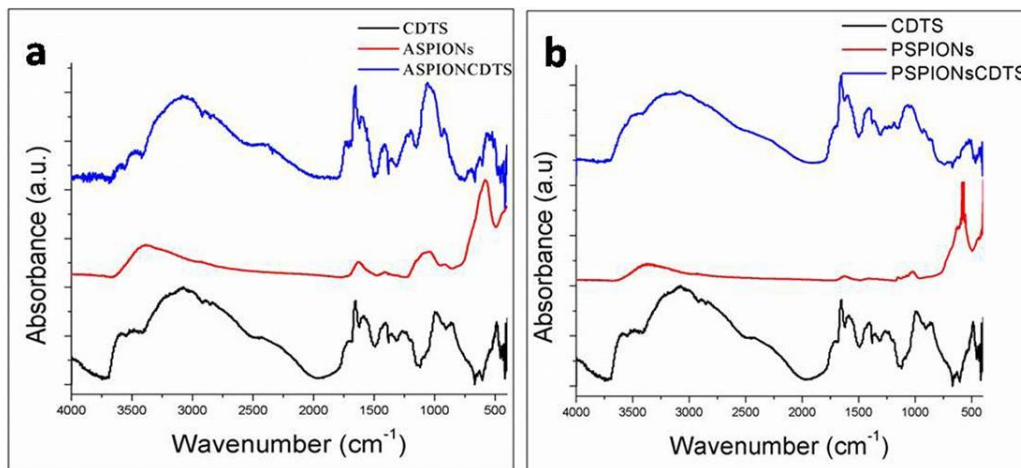


Figure - 49. FTIR spectra of (a) ASPION-CDTS, ASPION and CDTS and (b) PSPION-CDTS, PSPION and CDTS.

4.4.2.4 Magnetic Property

Magnetic hysteresis measured from VSM measurements divulges the superparamagnetic nature of PSPION-CDTS and ASPION-CDTS. The magnetic saturation values were found to be 42 emu/g for ASPION-CDTS and 3.17 emu/g for PSPION-CDTS (Figure – 50). The M_s values of A-SPIONs and P-SPIONs were decreased on conjugation with CDTS in both the cases with PSPION-CDTS experiencing drastic reduction.

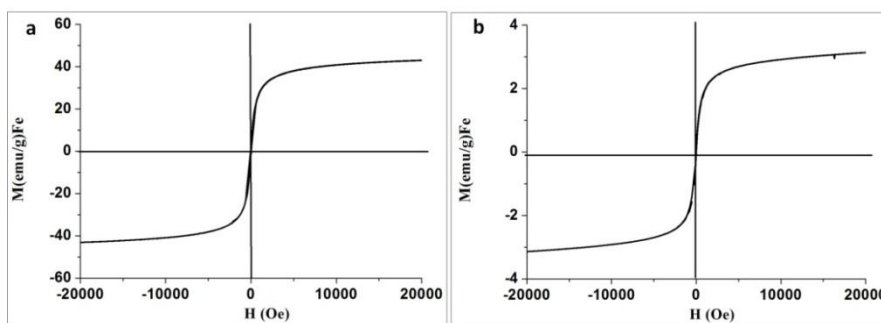


Figure - 50. Magnetic hysteresis curve (M-H) of (a) ASPION-CDTS and (b) PSPION-CDTS.

4.4.2.5 Magnetic Relaxivity

T_1 and T_2 relaxation of different concentrations of ASPION-CDTS and PSPION-CDTS were evaluated and the corresponding relaxation rates were calculated. For ASPION-CDTS, the r_2 and r_1 values were found to be 21.70 and 4.03 $\text{mM}^{-1}\text{s}^{-1}$ respectively with the r_2/r_1 ratio of 5.38. Likewise, for PSPION-CDTS, the r_2 and r_1 values were found to be 70.9 and 5.27 $\text{mM}^{-1}\text{s}^{-1}$ respectively with the r_2/r_1 ratio of 13.45 (Figure – 51).

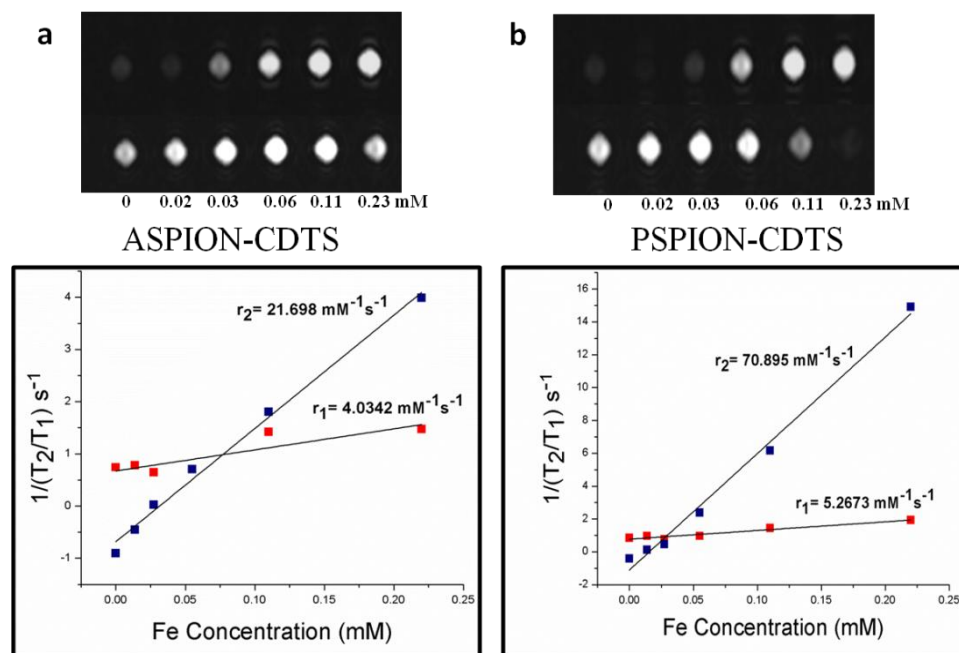


Figure -51. T_1 (upper) & T_2 (lower) weighted MR images for varying concentrations (0-0.23mM Fe) and Longitudinal (r_1) and Transverse relaxation rates (r_2) of (a) ASPION-CDTS and (b) PSPION-CDTS.

4.4.3 Optical Characterization

The UV-Vis spectra showed an absorption peak around 400 nm for CDTS and 415 nm for both ASPION-CDTS and PSPION-CDTS (Figure – 52a). The fluorescence spectra showed an excitation maxima at 405 nm for CDTS, 430 nm for ASPION-CDTS and

PSPION-CDTS and an emission maxima at 500 nm for CDTS, 492 nm for ASPION-CDTS and PSPION-CDTS (Figure – 52b,c).

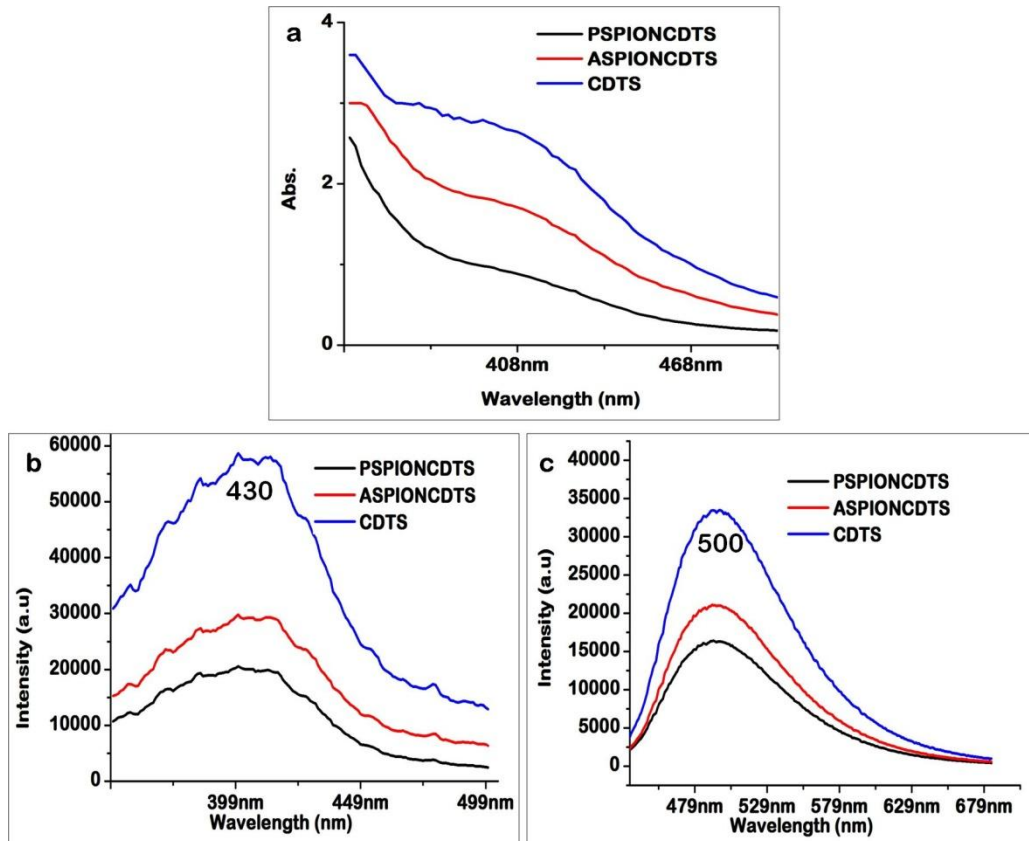


Figure- 52. Optical properties of CDTS based Hybrid nanoprobe, (a)UV-Vis absorption spectra (b) Excitation and (c) Emission Spectra of ASPION-CDTS, PSPION-CDTS and CDTS.

The concentration dependent optical imaging efficiency of CDTS, ASPION-CDTS and PSPION-CDTS evaluated using the Xenogen IVIS system has shown appreciable optical emission properties for the hybrid materials which could be used for optical imaging (Figure- (53-55)).

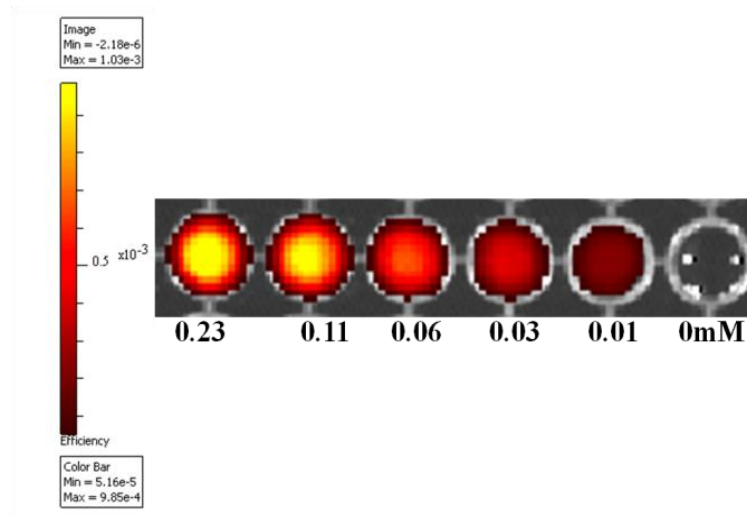


Figure-53. Fluorescence images of CDTS with varying concentration (Excitation at 430 nm and Emission at 500 nm). The scale bar on the left gives an indication about the efficiency of the probe.

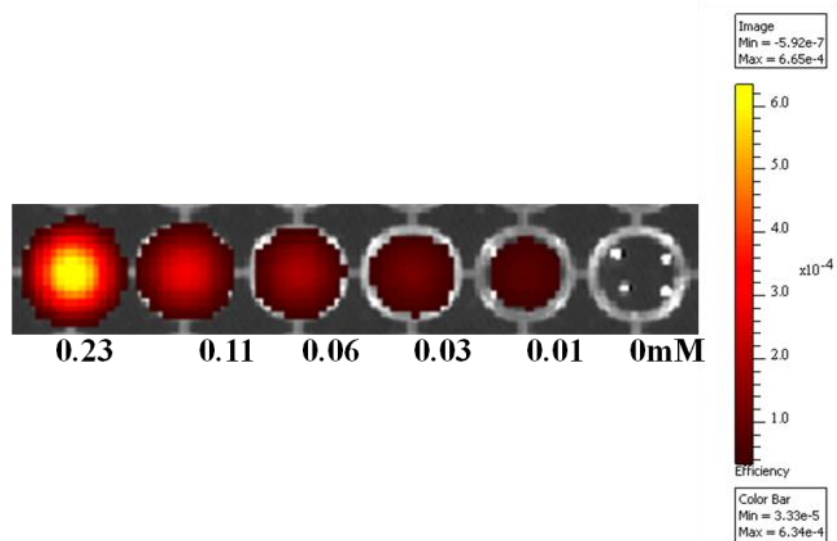


Figure-54. Fluorescence images of ASPION-CDTS with varying concentration (Excitation at 430 nm and Emission at 500 nm). The bar on the right gives an indication about the efficiency of the probe.

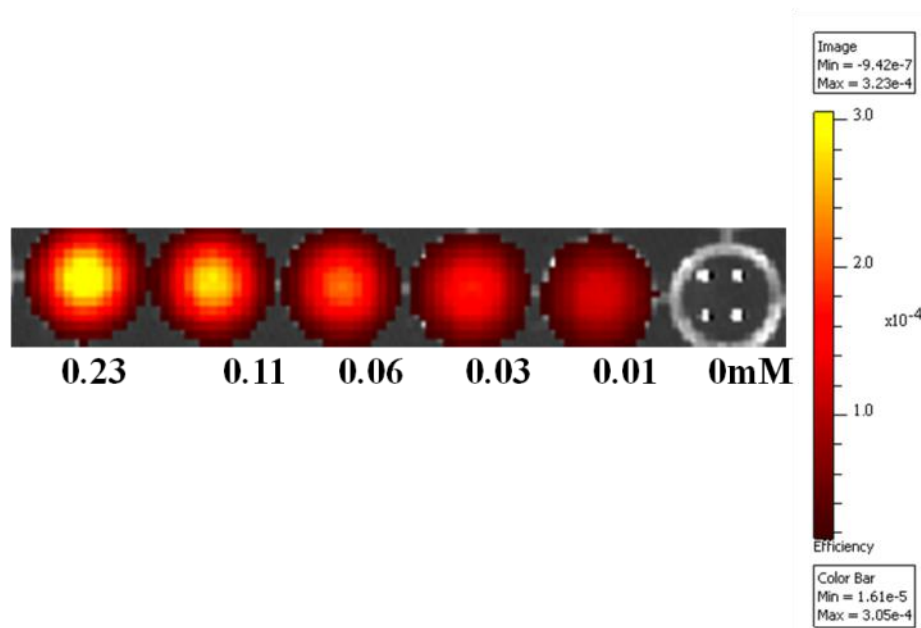


Figure-55. Fluorescence images of PSPION-CDTS with varying concentration (Excitation at 430 nm and Emission at 500 nm). The bar on the right gives an indication about the efficiency of the probe.

The excitation-emission – efficiency contour plots for the corresponding excitation – emission imaging was shown in Figure - 56(a-c). The contour extracted the spectral information of higher efficiency of ASPION-CDTS in the excitation and emission range around 430-450 nm and 500-550 nm. In this case, the contour plots are incomplete because the lowest excitation filter available in the optical imaging system coincides with the excitation wavelength of CDTS.

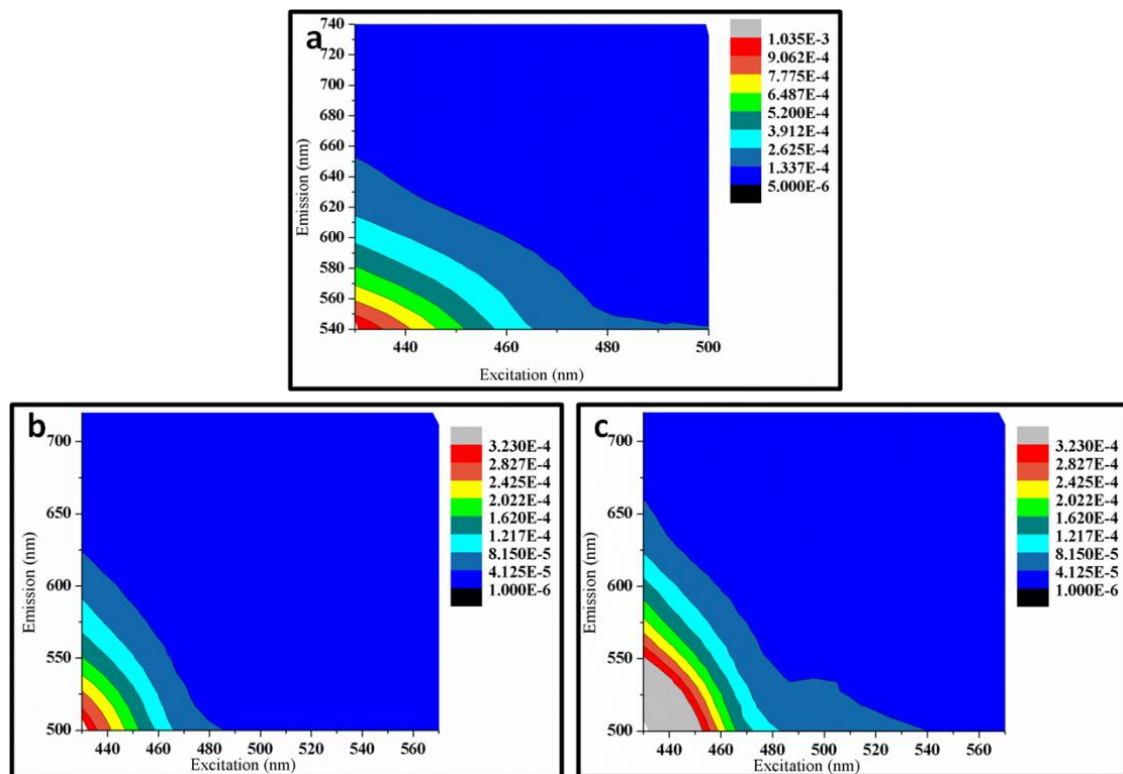


Figure-56. Excitation-Emission-Efficiency contour plots of (a) CDTs (b) ASPION-CDTs, and PSPION-CDTs. The bar on the right gives an indication about the efficiency of the probe.

4.4.4 Hemocompatibility Evaluation

Aggregation study of the CDTs samples with human RBC, WBC and platelet did not show any aggregation or morphological change under microscopic view, compared to the positive control PEI in any of the cases (Figure-57). Results of percentage hemolysis analysis also showed no lysis when the particles were in contact with the erythrocytes. The percentage of lysis was found to be less than 1% with all the CDTs samples.

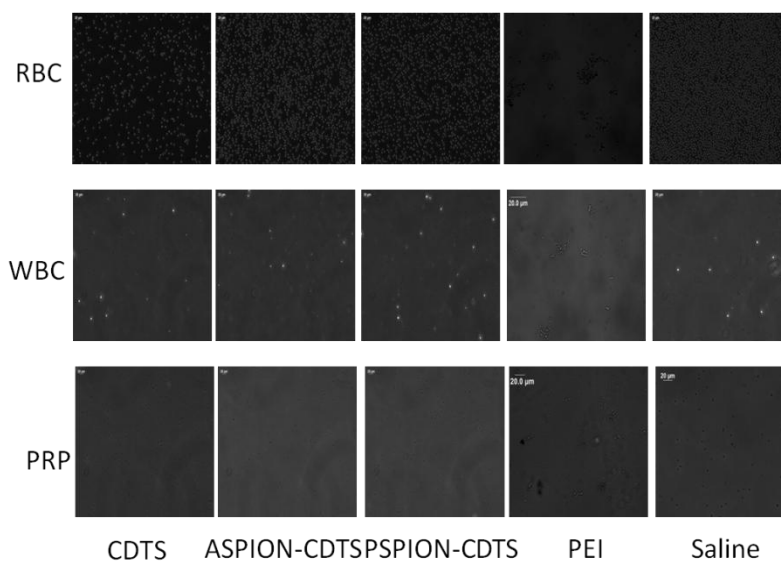


Figure - 57. Blood aggregation studies: RBCs, WBC's and platelets incubated with ASPION-CDTS, PSPION-CDTS, positive control, PEI and negative control, saline.

4.4.5 Cell culture studies

4.4.5.1 Cytotoxicity assessment

Cytotoxicity of the CDTS, ASPION-CDTS and PSPION-CDTS were evaluated on human hepatocellular cells, HepG2 using MTT assay (Figure – 58). Cell viability was of the order of 70-85 % for CDTS for concentrations ranging from 100 – 25 $\mu\text{g/ml}$ where as for SPION-CDTS nanoprobe, the cell viability was found to be increased. ASPION-CDTS hybrid nanoprobe showed 83-100 % viability and PSPION-CDTS showed 84-98 % for the same range of concentrations.

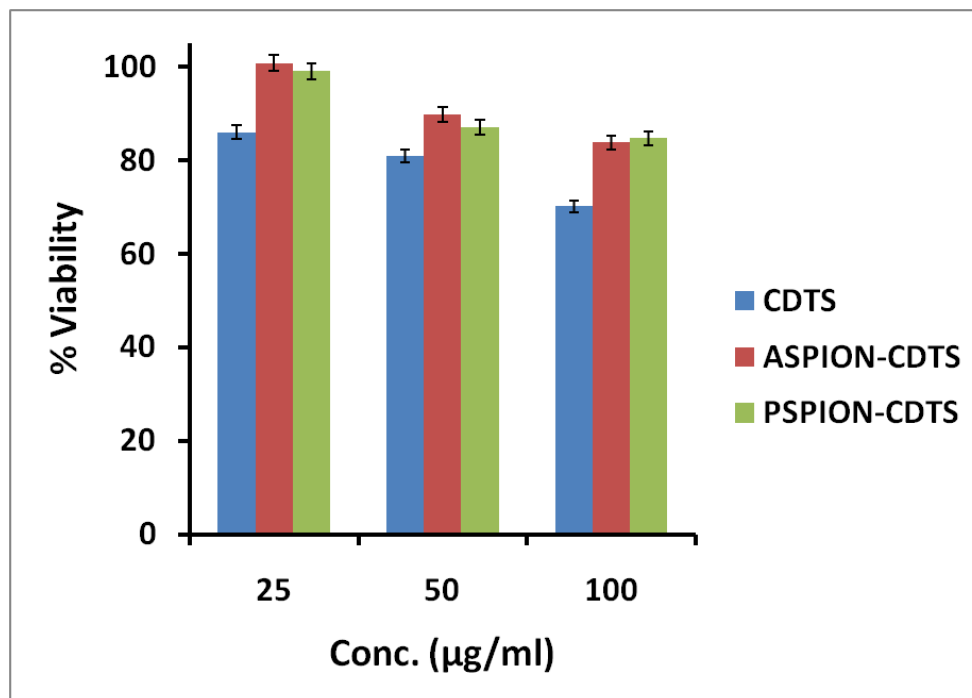


Figure - 58. Percentage cell viability of CDTS, ASPION-CDTS and PSPION-CDTS determined by MTT assay.

4.4.5.2 Cell uptake efficiency

The cellular uptake and labeling efficiency of ASPION-CDTS and PSPION-CDTS are shown in Figure - 59.

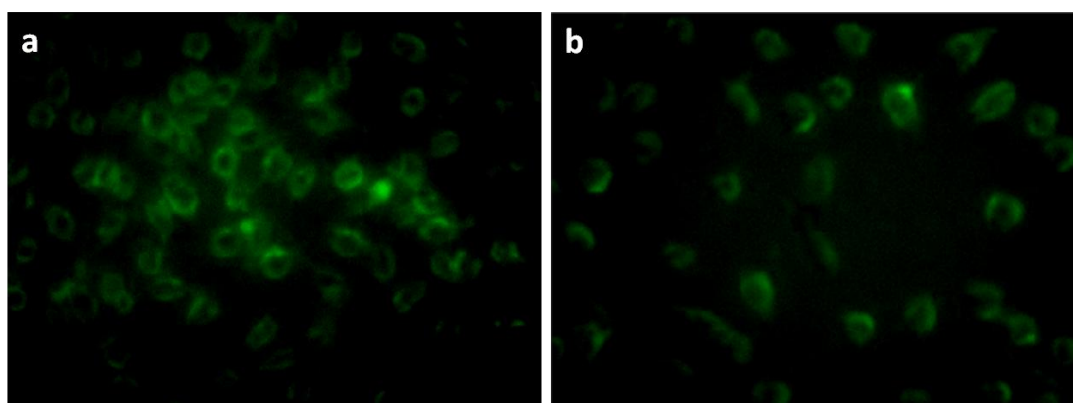


Figure - 59. Fluorescence microscopic images of L929 cells on incubation with (a) ASPION-CDTS and (b) PSPION-CDTS.

Green fluorescence of the CDTS corresponding to the emission of 500 nm of CDTS can be visualized from the fluorescent microscopic images of the cells incubated with the hybrid nanoprobe. Cell uptake of the ASPION-CDTS and PSPION-CDTS gives an indication that the particles are mostly concentrated in the cytoplasm. The normal morphology of the cells were found to remain undisturbed on 24 hr incubation indicating that the materials are cell friendly.

4.4.6 *In vivo* studies

4.4.6.1 *In vivo* Optical imaging of Hybrid nanoprobe.

The imaging efficiency of the developed hybrid nanoprobe were evaluated in the mouse model of liver fibrosis. Development of liver fibrosis was indicated by the LFT and the animals with elevated level of liver specific enzymes, SGOT and SGPT corresponding to the fibrosed state were selected for imaging. ASPION-CDTS and PSPION-CDTS administered rodents were imaged after 20 minutes of intravenous administration. In both the cases, increase in fluorescence intensity was observed from the liver of the fibrosis induced mice (Figure – 60 (a & b)). Even though the *in vivo* application showed low fluorescence, the organs harvested after 1 hr of post intravenous administration showed remarkable fluorescence efficiency in the liver indicating the hepatic uptake of the ASPION-CDTS and PSPION-CDTS. The fluorescence emission of the CDTS in the visible region which interfere with the autofluorescence of the body is the reason for less fluorescence signal observed in the wholebody imaging.

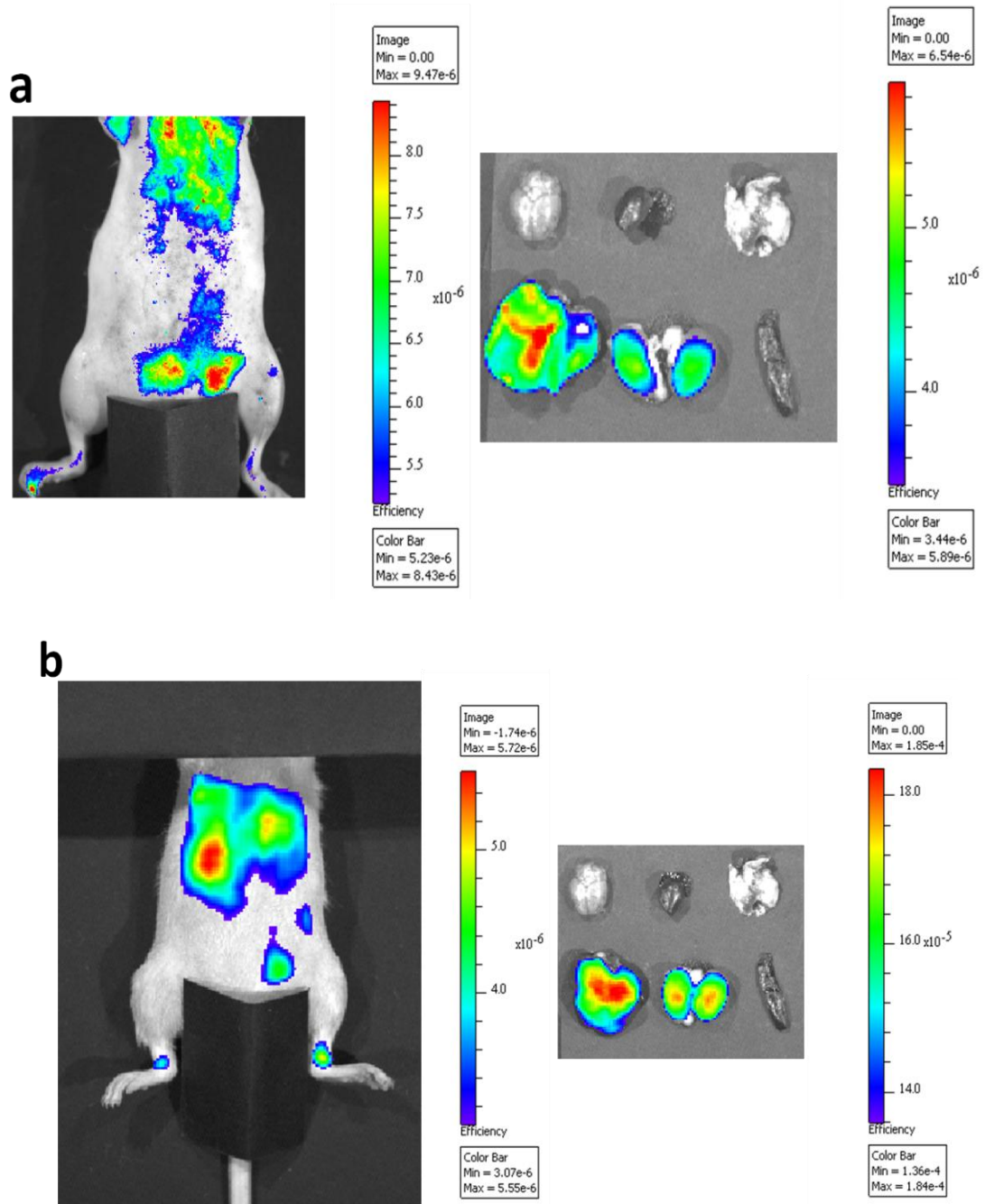


Figure – 60. *In vivo* optical images of fibrosis induced mice model administered with (a) ASPION-CDTS and (b) PSPION-CDTS. The bar on the right gives an indication about the efficiency of the probe.

The optical images of the organs extracted from the respective mice model show the biodistribution of the nanoprobe with an increased fluorescence in the liver.

4.4.7 Histopathological Analysis

Histopathological evaluation of the CCl₄ induced mice liver revealed moderate to severe necrosis of hepatocytes with infiltration of mononuclear cells in liver sections (Figure-61). The beginning of compartmentalization can also be visualized in the HE stained liver sections. MT stained images indicates the early stage of fibrosis. The presence of iron in the liver was visualized as blue tinges in PB stained sections indicating the uptake by the hepatocytes.

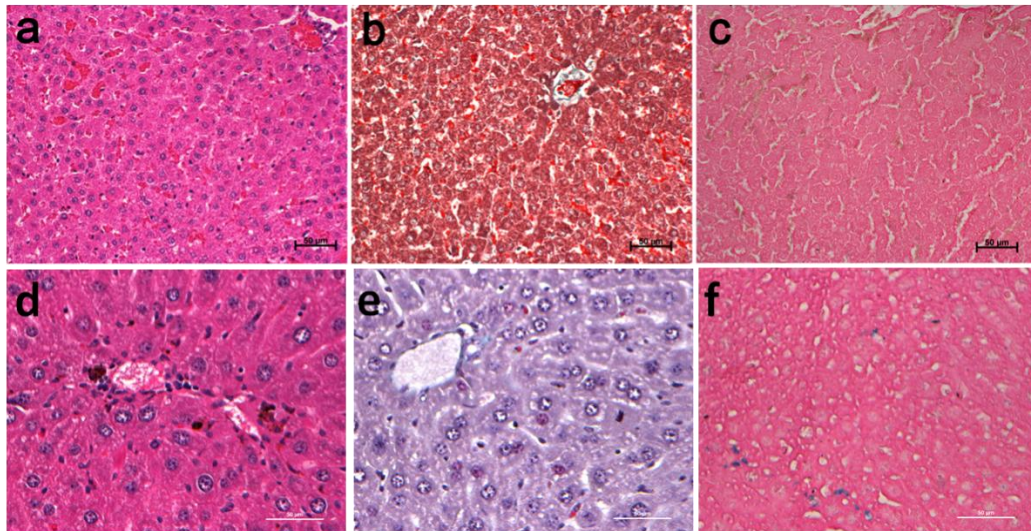


Figure – 61. H&E (a&d), MT (b&e) and PB (c&f) stained histopathological images of (a-c) normal liver and early stage fibrosis of mice liver (d-f).

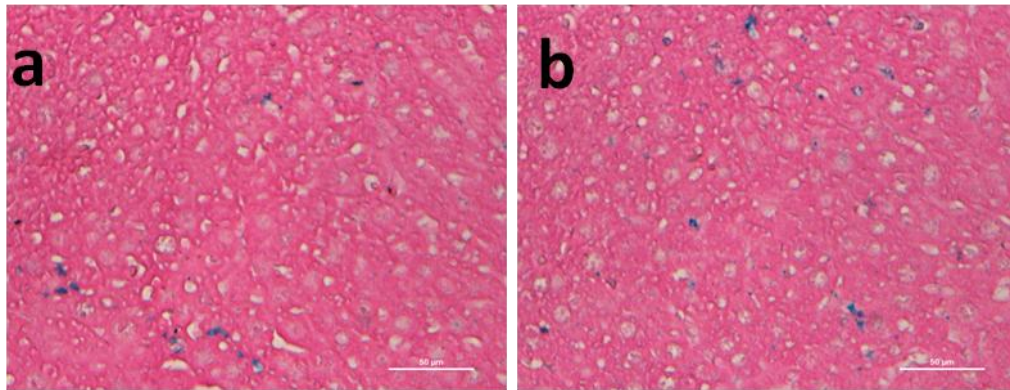


Figure – 62. PB stained histopathological images of fibrosed rat liver administered with ASPION-CDTS and PSPION-CDTS.

The PB stained images of the diseased liver administered with ASPION-CDTS and PSPION-CDTS can be observed in Figure – 62. The blue tinges represent the presence of iron.

Chapter 5
DISCUSSIONS

5. DISCUSSIONS

This chapter discusses in detail the results of the thesis listed in chapter 4. This includes the discussion on the results of synthesis of the nanoprobes, physico-chemical and magnetic characterization, hyperthermia, biological evaluation and characterizations including *in vivo* and *in vitro* studies. Separate discussions based on the results of the different USPIONs, multimodal nanoprobes and hybrid nanoprobes under the above mentioned heads are provided.

5.1 Preparation of ironoxide based MR Contrast Agents

Considering the safety profile and the suitability of the organ specific imaging of the contrast agents, ironoxide based agents are preferred over Gd based agents (Laurent *et al.*, 2008). Especially for the diagnosis of diseases affecting liver and lymph nodes, IONs based MR contrast agents are found to be more useful because of the increased T₂ response of the fat deposits in liver. In this study, the main focus was for the development of IONs based MR contrast agents for the diagnosis of liver diseases. Utilizing the overexpression of carbohydrate recognition domain in the disease condition of liver, the surface of SPIONs was modified with carbohydrate polymers and compared.

5.1.1 Synthesis of Ultra small Super Paramagnetic Iron Oxide nanoparticles (USPIONs)

USPIONs with a size of 12 nm were prepared by adopting the method of co-precipitation of iron salts with NaOH. For USPIONs, those having hydrodynamic

diameter less than 50 nm, there will be an increase in the circulation and blood half-life time (Berry *et al.*, 2003). The as prepared USPIOs were stabilized and surface modified with citrate, dextran, alginate and pullulan with an intention to optimize the particle size and magnetic properties simultaneously. Initially, TSC was chosen to stabilize the USPIOs. Since the final application hypothesized being the liver imaging, later three different carbohydrate polymers showing varying liver affinity have been chosen for surface stabilization.

5.1.2. Synthesis of Citrate stabilised USPIOs (C-SPIOs)

C-SPIOs were prepared by choosing TSC as stabilizing agent, which favoured the particle dispersivity without compromising the overall particle size. The coating agents with small ligands are reported to give high magnetic properties with less particle size (Kim *et al.*, 2011). Selection of TSC as the coating agent and the optimized coating thickness reduced the particle aggregation and preserved the magnetic properties to a great extent. Ambient conditions were maintained for the covalent attachment of the TSC with USPIOs to generate enhanced magnetic relaxivity and highly dispersed colloidal suspension which was stable over a period of six months.

5.1.3. Synthesis of Carbohydrate Polymer Stabilised SPIOs

The surface modification of SPIOs with carbohydrate polymers favours the MR contrast agent for liver imaging and so three different carbohydrate polymers modified SPIOs were prepared, first being the dextran modified SPIOs. Most of the previous reports based on SPIOs based on dextran stabilized SPIOs were mainly using low molecular weight polymer (Simberg *et al.*, 2009; Weinstein *et al.*, 2010). It is

reported that dextran with molecular weights below 60 kilodalton will easily filter through the glomerulus and cause osmotic nephropathy which leads to chronic renal failure (Feest, 1976; Morgan, Little & Evans, 1966). So in this study, dextran of molecular weight 70 kilodalton has been used for modification.

Sodium alginate, which is a renewable and biodegradable natural carbohydrate polymer, was the second candidate considered for the surface functionalization of SPIONs. Apart from being a polysaccharide, alginate stabilization increased the ease of further functionalization of ASPIONs. Only very few studies have been reported on alginate functionalized magnetic nanoparticles (Ma *et al.*, 2006) and none extended the same to *in vivo* application.

SPIONs stabilized by pullulan, P-SPIONs, have been developed as a contrast agent to improve the sensitivity of MRI in the early stage detection of hepatocellular carcinoma. Pullulan, having the inherent property of high liver affinity, on conjugation with SPIONs enhances the accumulation and retention time of SPIONs in the liver. The electrostatic interaction of pullulan with SPIONs was preferred for the stabilization of SPIONs in order to retain the liver targeting capacity of pullulan. Eventhough many reports have commended on the significance of pullulan in biomedical application, there was no effort to study extensively in this direction for utilizing this favourable property of pullulan (Gao *et al.*, 2010).

5.1.4 Physico-Chemical & Magnetic Characterization

5.1.4.1 Determination of Particle Size

TEM micrograph indicated the average core size of the SPIONs as 12 nm irrespective of the surface functionalization with four different stabilizers whereas the hydrodynamic diameter varied from one another (Figure-14 & 15).

For the smallest ligand citrate, C-SPIONs possessed the lowest hydrodynamic diameter of 30 nm, whereas the bare USPIONs showed an aggregating nature and had a diameter of 24 nm. With the increase in the outer shell's size, the hydrodynamic diameter also increased with a maximum of 80 nm for P-SPIONs. The high dispersivity observed in the surface stabilized SPIONs compared to USPIONs is attributed to the hydroxyl interaction of outer shell molecules to the surface of iron oxide nanoparticles, which reduces the inter particle interaction considerably, compared to that of the USPIONs. Previous reports on SPIONs favours the hydrodynamic diameter in the range similar to that of this study (Laurent *et al.*, 2008).

5.1.4.2 X-ray Diffraction (XRD) Studies

XRD pattern of bare and the surface modified SPIONs showed the inverse spinel structure of the magnetite irrespective of the outer shell. The sharpness of the XRD peaks in C-SPIONs, D-SPIONs, A-SPIONs and P-SPIONs comparable to that of USPIONs indicates that there is no significant change in the crystallinity of the materials after the surface modification (Figure-16). Magnetite phase of the materials have been confirmed in comparison with the earlier reported works (Nigam *et al.*, 2011) and JCPDS card No. 89-0691.

5.1.4.3 Fourier Transform Infra-red spectroscopy (FT-IR)

The FTIR bands of USPIONs at 572 and 450 cm^{-1} correspond to the vibrational modes of Fe-O vibrations of tetrahedral and octahedral sites of magnetite respectively. The FTIR bands of TSC at 1605 with shoulder at 1680 cm^{-1} corresponding to the carboxylate ion and 1075 cm^{-1} corresponding to the C-OH group were found to get shifted to 1618 and 1065 cm^{-1} with the absence of shoulder peak on surface stabilization. Apart from this, 1397 cm^{-1} band corresponding to the CH_2 group remained without shift in both the spectra. The overall inference revealed the hydroxyl interaction with the NPs surface. The shifts corresponding to the asymmetric and symmetric stretching of carboxyl group confirms the binding of citrate in C-SPIONs. The FTIR spectra of dextran exhibited distinct bands around 1652 due to the bending modes of water molecules. 2926 and 1460 cm^{-1} are assigned to C-H vibrational modes and 1005 cm^{-1} due to C-O vibrations and the bands at 916, 852 and 764 cm^{-1} corresponding to α -glucopyranose ring deformation modes. The D-SPIONs showed shifts in corresponding bands of C-H and C-O group regardless of the non-shift of bending vibrations of water molecule which indicates the interaction of dextran with SPIONs (Figure-17). The presence of Fe-O band around 580 cm^{-1} also confirmed the dextran interaction with iron (Bautista *et al.*, 2005).

Pure sodium alginate exhibited IR bands around 3361, 1621, 1413 and 1060 cm^{-1} corresponding to the O-H, C-O, C-H and C-C vibrations. Shifts in the O-H, C-O and C-C bands along with the undisturbed C-H vibration mode of alginate and the presence of Fe-O band at 582 cm^{-1} confirms the formation of A-SPIONs. Likewise, Pullulan

exhibited sharp absorption bands near 3362(O-H stretch), 2924 (–CH₂ stretching vibrations), 1623 (C-O stretching), 1409 (C-H bending), 1020 (C-CO stretching) and 955 cm⁻¹ (–CH out-of-plane bending). The P-SPIONs also exhibited all these bands with diminutive shifts except for 1020 cm⁻¹ band in addition to the parent SPION formulation.

5.1.4.4 Thermo Gravimetric Analysis (TGA)

The four distinct stages of thermal decompositions of TSC around 171, 321, 557 and 1120°C corresponding to the total weight loss of 13.23, 26.52, 45.51, and 98.29% represents the elimination of bound water, exothermic phase transition, endothermic phase transition and linear degradation respectively (Srivastava *et al.*, 2011). TGA curve of C-SPIONs also show four similar stages of decomposition around 147, 315, 597 and 1188°C corresponding to the total weight loss of 2.3, 4.6, 5.7 and 7.1% (Figure-18). TGA curve of free dextran shows three distinct degradation stages at 118, 357 and 492°C with a corresponding total weight loss of 10, 77 and 100%. The decomposition starts with elimination of bound water at around 118°C followed by the breakdown of organic skeleton around 357°C and a complex degradation process in the temperature range of 257–492°C resulting in the complete degradation of dextran indicating total weight loss at 492°C. The TGA curve of D-SPIONs also shows corresponding stages of degradation around 120°C with a weight loss of 2.31% and around 320°C with a weight loss of 8.94%. At around 490°C a total weight loss is observed, which in turn indicates the complete dissociation of dextran from the magnetite. Carp *et al* have reported similar

decomposition pattern in an extensive thermal decomposition study of dextran coated magnetite nanoparticles (Carp *et al.*, 2010).

TGA curve of Alginate shows decomposition by dehydration at 85°C followed by degradation at 209°C and 268°C with a 50% weight loss (Soares *et al.*, 2004). At the temperature around 788°C, a total weight loss of 77% was observed. The corresponding degradation of alginate in ASPIONs is around 115°C, 189°C, 261°C and 794°C with a total weight loss of 24%. From the TGA curve of pure pullulan, the rapid thermal decomposition can be observed at 287°C with a complete dissociation at 492°C which agrees well with the report of Karim *et al.* (Karim *et al.*, 2011). The thermal degradation of pullulan in P-SPIONs is shifted to 183°C with a weight loss of 4% and the complete dissociation was observed after 650°C with a total weight loss of 12%.

In all the cases, it can be observed that the degradation temperature of surface modified SPIONs got shifted to a lower temperature on comparison with that of the pure stabilizers showing an early decomposition. This shift observed in the decomposition temperature is due to the effect of catalytic behaviour of iron oxide nanoparticles in the system.

5.1.4.5 Magnetic Property

The magnetic property of the particles depends upon their structure, size, shape and chemical phase. Superparamagnetic property of all the SPION based nanoprobe was clearly demonstrated by the zero coercivity. This property is a prerequisite for the particles to demonstrate relaxivity property suitable for T₂ contrast agents. It is also reported that superparamagnetic property helps in the uniform dispersion of the particles

in solution without the occurrence of severe aggregation that ferromagnetic nanoparticles usually suffer from (Manju *et al.*, 2011). Hence superparamagnetic property, which is highly influenced by the size of the particles, is important for smooth circulation of the material through the blood. Saturation magnetization of the SPIONs was found to be 62.7 emu/g and that of C-SPIONs, D-SPIONs, A-SPIONs and P-SPIONs as 57.5, 45.8, 53 and 24.9 emu/g respectively (Figure - 19). In all the cases, a reduction in the saturation magnetization was observed due to surface modification. But the variation was most noticeable in the fourth case. The remarkable change in the magnetic saturation value of P-SPIONs to 24.8 emu/g from 62.7 emu/g on pullulan stabilization retaining the superparamagnetic nature substantially proves the influence of surface modification of SPIONs on the magnetic properties. The TGA result also favours this observation. This result confirms the preservation of magnetic properties of surface modified SPIONs even after the surface coating with the respective stabilizers. The observed pattern of the hysteresis curve is an indication of the particle's single domain existence with only one orientation of magnetic moment. Here, the magnetization reduces from plateau region to zero on removal of the magnetic field. This further supports the magnetite phase of the developed material (Gupta & Wells, 2004).

5.1.4.6 Magnetic Relaxivity measurements

The T_1 & T_2 relaxation rates of citrate coated iron oxide nanoparticles as well as uncoated ironoxide nanoparticles were evaluated by varying the Fe concentration (mM). The intensity of the MR images of the solutions of different Fe concentration decreased

as the Fe concentration within the sample is increased for T₂ weighted imaging. This shows the typical nature of T₂ contrast agents. Likewise, the MR image intensities were found to increase with the increase in Fe concentrations for T₁ weighted imaging. The less relaxivity values of the bare USPIOs compared to the surface modified ones indicate that the surface modification plays an important role in the magnetic relaxivity of the material which is crucial for T₁ or T₂ weighted imaging.

The relaxivity measurements under a 1.5T MRI scanner resulted in high T₂ relaxation rate for the citrate coated USPIOs, which is an essential property for implementing the action of the particle as T₂ contrast agent. The decrease in the intensity of the images with the increase in Fe concentration of the sample reveals the T₂ effect of both bare and citrate coated USPIOs. The use of 1.5 T MRI scanner also gives a clear idea of the relaxivity values when used in clinical application. The relaxivity values increased up to 102 mM⁻¹s⁻¹ for citrate coated USPIOs which was 57.1 mM⁻¹s⁻¹ for uncoated USPIOs (Figure - 20). This increase in relaxivity depends mainly on the effect of the delay in relaxation of the proton bound to the citrate coated USPIO system and the water protons. Compared to other iron oxide based contrast agents of similar sizes, r₂ of 102 mM⁻¹s⁻¹ and relaxivity ratio of 37.91 obtained in this study for C-SPIONs are found to be very high which is a clear indication for using the same as a more efficient T₂ contrast agent. In our study, the r₂ values varied in the increasing order for C-SPIONs, A-SPIONs, D-SPIONs and P-SPIONs with the highest r₂/r₁ ratio of 68.33 for P-SPIONs. A very high T₂ relaxation value of 160 mM⁻¹s⁻¹ observed for P-SPIONs among all the systems considered makes it the most efficient

contrast agents out of the four different USPIO based probes considered in this study. The reason for the elevated relaxation rate of P-USPIOs may be due to the profusion of hydroxyl groups of pullulan, which resulted in the increase in the local density of surrounding water molecules and its diffusion around the particle. (Yim *et al.*, 2011) Such attachments may accordingly enhance the r_2 relaxivity of the contrast agent.

The use of USPIO nanoparticles having dimensions in the range <50 nm as MR contrast agents improved the long blood half life period and diminished the chance of accumulation in reticuloendothelial system. The commercially available USPIOs based contrast agents like Sinerem and Combidex with size in the range 20-40 nm and coated with dextran reports r_1 & r_2 relaxivities as $22.7 \text{ mM}^{-1} \text{ s}^{-1}$ and $53.1 \text{ mM}^{-1} \text{ s}^{-1}$ respectively (Geraldese *et al.*, 2009). Among the reported magnetic relaxivity studies of USPIOs the core Fe_3O_4 nanoparticles with different coatings showed different relaxivity values. Most commonly reported USPIOs were coated with Dextran, Citrate, PEG, and Silica. The average hydrodynamic diameter of PEG-g-PEI coated ironoxide nanoparticles of 10 & 30 nm shows r_2 values as 39.8 & $93.3 \text{ mM}^{-1} \text{ s}^{-1}$ (Duan *et al.*, 2008). The average hydrodynamic diameter of PEI coated ironoxide nanoparticles of 10 & 30 nm shows r_2 values as 75.2 & $107.3 \text{ mM}^{-1} \text{ s}^{-1}$. The average hydrodynamic diameter of PMO coated ironoxide nanoparticles of 10 & 30 nm shows r_2 values as 27.2 & $70.5 \text{ mM}^{-1} \text{ s}^{-1}$ with the applied magnetic field of 1.5T. (Dwan *et al.*, 2008) The MR relaxivity studies of silica-coated USPIO particles of size 10 nm reported in the study by Zhang *et al* shows the highest T_2 relaxivity, r_2 of $339.80 \text{ s}^{-1} \text{ mM}^{-1}$ in 1.5T applied field. (Zhang *et al.*, 2003) Eventhough the application of polymeric stabilizers increase the

relaxivity values, the coating thickness will have an adverse effect on the magnetic saturation value of the overall particle. In order to minimize the coating thickness, the use of citrate stabilizer will be more effective. The relaxivity studies of citrate coated superparamagnetic iron oxide nanoparticles of hydrodynamic diameter 25 nm shows r_1 & r_2 values as 35.45 & 51.808 $\text{mM}^{-1}\text{s}^{-1}$ with the applied 3T magnetic field. The saturation magnetization of the citrate coated nanoparticle showed 62emu/g (Srivastava *et al.*, 2011). In a similar study by Kotsmar C *et al* the magnetic saturation value of citrate stabilized ironoxide nanoparticles of diameter 12nm was 41 emu/g. (Kotsmar *et al.*, 2010). The citrate coated ironoxide (VSOP-C184) which is under Phase-II clinical development is having r_2 relaxivity value 37.1 $\text{mM}^{-1}\text{s}^{-1}$ (MICAD research team, 2006). The size reduction of ironoxide nanoparticles to less than 4 nm increases the possibility of using the probe as T_1 contrast agent and is reported by Kim *et al* (Kim *et al.*, 2011). Pullulan and alginate coated ironoxide nanoparticles have not been reported so far as MRI contrast agents with remarkable relaxivities.

5.1.4.7 Hyperthermia

USPION showed an increase in temperature upto 55°C in an alternating electric field of 400 A for 15 min which on surface modification decreased to 48°C for C-SPIONs, 50.9°C for D-SPIONs, 52°C for A-SPIONs and 43°C for P-SPIONs (Figure - 21). For the temperature based therapy, hyperthermia, a much lower temperatures of ~40°C–43°C is sufficient for effective cell death in the case of cancer (Huang H S & Hainfeld J F, 2013). All the developed SPIONs of the current study showed this property with sufficient temperature hike within 8-15 min proving their candidature in

therapeutic application. Different groups have reported the *in vitro* studies which increased cell lysis on raising the temperature up to 42°C for 30 min (Silva *et al.*, 2011). C-SPIONs, D-SPIONs and A-SPIONs raised its temperature to 40°C in 8 min on applying a 300 A current. In a clinical scenario, a rapid increase from the body temperature to the order of 43°C will favour efficient cancer cell death without destructing the surrounding normal cells. The hyperthermic effect of pullulan acetate coated IONPs on KB cells by Gao *et al* showed excellent therapeutic efficacy (Gao *et al.*, 2010). Citrate capped MNPs by Cheraghipour *et al*, also showed remarkable heating effect with a specific absorption rate of 16.74 w/g, during the application of a magnetic field (Cheraghipour *et al.*, 2012).

5.1.5 Hemocompatibility Evaluation

For the safe administration of the particle through the blood stream, absence of aggregation of hematocytes and hemolysis are important. No aggregation was observed for any of the blood cells on incubation with 100 µg/ml of all of the surface modified SPIONs in this study (Figure-22). The percentage of lysis was less than 1% for 100 µg/ml of the surface modified SPIONs which is well within the acceptable limits [Murthy *et al.*, 1999; Nimi *et al.*, 2011]. These results confirm the blood compatible nature of surface modified SPIONs which was further proven to be ideal during the *in vivo* experiments when all of them could be administrated intravenously to blood stream safely for MR imaging.

5.1.6 Cell culture studies

5.1.6.1 Cytotoxicity assessment

The behaviour of the cells expressed by its metabolic activity on interacting with different concentrations of the particles was evaluated. Clinically approved admissible dose for MR imaging is 25 µg/ml for a human of average body weight. Previously a maximum cell viability of 80% only has been reported at this concentration (Kim *et al.*, 2003; Zhang *et al.*, 2009). As the aim of the study is to prove the suitability of the developed nanoparticles for its use as MR contrast materials for liver fibrosis, it is important to see the toxicity effect of the particles on liver cells. For this, cytotoxicity of the nanoparticles was evaluated on human hepatocellular cells (HepG2) using MTT assay. All materials of the study, C-SPIONs, D-SPIONs, A-SPIONs and P-SPIONs showed more than 80% of viability at a higher concentration of 100 µg/ml (Figure – 23). Perhaps, this property of the present system can very well address the previously reported issues of iron oxide based MRI contrast materials which had been withdrawn from the market due to reasons related to safety concerns.

5.1.6.2 Cell uptake efficiency

Cell uptake of all the surface modified SPIONs are clear on PB staining which gives an indication that the particles are mostly concentrated in the cytoplasm (Figure – 24). The normal morphology of the cells remains undisturbed after 24 hr incubation with the particles indicating the cytocompatibility of the materials. Internalization of the particle without any targeting moiety is also achieved due to the local neutralization effect of cell membrane to the repulsive interaction with the anionic particles in all the

cases of SPIONs. The enhanced liver affinity of P-SPIONs also accounts for the increased cell uptake in this case. This is an added advantage of the system and is clear from the supremacy of the developed SPIONs over commercially available contrast agents like Resovist and Endorem in the cell internalization.

5.1.7 *In vivo* MRI studies

Contrast enhancement, marginal delineation and early disease diagnosis are the current vital factors of concern in the field of MRI and in the diagnosis of cancer. In the current study, we tried to address the issue by developing hepatocyte targeted MR contrast agent for the diagnosis of early stage liver abnormality. The intravenous administration of all the SPIONs with the different surface modifications, namely C-SPIONs, D-SPIONs, A-SPIONs and P-SPIONs demonstrated good contrast enhancement in the T₂ weighted MR images of fibrotic liver in rodent model (Figure - 26). The hypointensity observed in the post-contrast T₂ weighted MR image is an indication of heavy uptake of SPIONs by the liver cells. Within the hypointense liver, hyperintense streaks are visualised, which represents the Kupffer's cell devoid fibrotic regions of the liver. There is an excessive accumulation of extracellular matrix in fibrosed liver and hence a decrease in the Kupffer's cell density. The amount of collagen increases and the ratio of fibro-connective tissue verses liver cells increases at the fibrosed sites (Albanese *et al.*, 2012; Bovenkamp, 2007). In the case of C-SPION administration, normally, the probe reaches liver through normal opsonization process and will be taken up by the Kupffer's cells. The negative surface charge of C-SPIONs also favours the internalization through the cationic sites of plasma membrane of the

liver cells (Verma *et al.*, 2010). In the case of D-SPIONs, A-SPIONs and P-SPIONs, the carbohydrate polymer coatings facilitates the receptor mediated endocytosis. The spectacular enhancement in the MR contrast in the case of P-SPIONs may be due to the high affinity of pullulan towards liver, especially in the diseased condition. In addition to the normal opsonization process of SPIONs by the liver macrophages, Kupffer's cells, the polysaccharide recognized by receptors such as asialoglycoprotein receptors (ASGP-R) favoured the increased accumulation of P-SPIONs in the liver (Kaneo *et al.*, 2001). In comparison with citrate, dextran and alginate as stabilizing agents, the targeting efficiency of P-SPIONs are well proven with the highest percentage signal intensity (PSI) value of 67%. Increase in the signal intensity calculated from the ROIs of P-SPIONs compared with the C-SPIONs, D-SPIONs and A-SPIONs administered T₂ weighted MR images indicates the enhanced liver uptake capacity of pullulan via ASGPR. The iron uptake of Kupffer's cells remains almost constant since the concentrations of the four SPIONs administered were kept constant. So the drastic contrast enhancement in the liver image corresponding to the intravenous administration of P-SPIONs rely mainly on the systemic circulation and strong binding of pullulan to the ASGPR with high affinity, resulting in the internalization of the bound molecule to the hepatocyte via receptor mediated endocytosis.

But in a fibrosed condition, due to decrease in the density of Kupffer's cells, the SPIONs uptake will be less, and hence appear as hyperintense streaks, which are clearly visible in the MR images. A better diagnosis through visualization of the extent of fibrosis is possible from the pseudo coloured image (Figure - 26). During the

pathogenesis of liver fibrosis, the devastation of normal liver architecture occurs due to the over activation of multiple cells present in the hepatic sinusoid. This triggers the overproduction of extracellular matrix and deposition of collagen fibers along with the mutilation of degradation process resulting in the excessive accumulation of scarred fibrotic tissue in the liver. The fibrotic accumulation will lead to the formation of nodules which subsequently results in the diminution of Kupffer cell density at the site (Talwalkar *et al.*, 2008). The foreseen pathological information on the progress of liver fibrosis has been observed in the T₂ weighted MR image also. The hyperintense streaks observed in the hypointense fibrotic liver represents the fibrosis specific areas within the liver. The diminution of Kupffer cell density at the localized areas of fibrous accumulation is the reason for the lack of uptake of SPIONs. This drastic contrast variation in the MR image helps to visualize the fibrous bridges that initiate the compartmentalization of liver during the progression of liver fibrosis which helps in determining the degree of extend of fibrosis. Accordingly, all the developed SPIONs serve as MR contrast agent, of which, P-SPIONs is identified as the most efficient and more hepato-specific MR contrast agent for the early diagnosis of liver abnormalities.

5.1.8 Histopathological Analysis

H&E and MT stained images of normal liver revealed lobular architecture with central vein and radiating hepatic cords. Likewise, the fibrotic liver revealed pronounced morphological alterations evidenced by disruption of the tissue architecture, moderate to severe necrosis of hepatocytes with infiltration of mononuclear cells and accumulation

of fibers in perilobular and portal triad areas. The excessive accumulation of collagen fibres are very well distinguished in the MT stained sections (Figure – 27). Based on the H&E and MT staining procedures, the fibrous bridges dividing the liver into rounded islands of hepatic parenchyma resulting in the nodular formation surrounded by fibrous tissue has been observed in the liver. These histopathological observations reconfirm the development of fibrotic stage of liver in the rat model (Constandinou *et al.*, 2005; Le Naour *et al.*, 2012). The iron uptake by the liver macrophages which was responsible for the hypointense MR image of the liver has been confirmed by PB staining.

5.2 Preparation of Multimodal nanoprobes

Multimodal nanoprobes prepared using ATTO dye having emission in the NIR range retained both the magnetic properties of SPIONs and the optical properties of ATTO dye. The electrostatic interaction is preferred in order to retain all the ASGPR targeting property of the DSPIONs, ASPIONs and PSPIONs.

5.2.1 Optical Characterization

Atto dye was chosen for its NIR emission property as this will avoid interference from the autofluorescence during the *in vivo* application. The excitation emission maxima at 680 nm and 712 nm overruled the interference of autofluorescence from the animal body. Previous studies report the use of Cy5.5 dye conjugated to IONs (Kircher *et al.*, 2003). Fluorescence imaging of the three SPIONs-AT complex for its optical property showed remarkable fluorescence efficiency which suits for the *in vivo* application. The excitation-emission contour extracted the spectral information of

higher efficiency for ASPIONs-AT in the excitation and emission range around 700-720 nm and 720 - 740 nm (Figure 30-34) compared to the other systems.

5.2.2 *In vivo* Optical imaging of multimodal nanoprobles.

In vivo imaging using the hybrid materials by the intravenous tail vein administration of DSPION-AT, ASPION-AT and PSPION-AT showed highest fluorescent signal intensity from the liver of the animals (Figure - 36). This finding supports the hypothesis of using the developed material for multimodal imaging in the case of liver based diseases, especially liver fibrosis. The organs harvested and imaged after 1 hr of iv administration also showed highest fluorescence efficiency in the liver showing the maximum uptake of the SPIONs-AT by the liver tissue. The NIR emitting SPION-AT probes further reduced the interference from autofluorescence of the mice and the images can be very well distinguished without any further post processing. The significant increase in fluorescence at the fibrosed liver is attributed to targeting of the SPIONs in the liver due to overexpression of ASGPR and hence is useful in the diagnosis of the progression of liver abnormalities.

5.3 *Hybrid nanoprobles using Gold Clusters and SPIONs*

5.3.1 Synthesis of Hybrid Nanomaterial (ASPIONs-Au)

The fluorescent Au BSA clusters were prepared by the procedures reported earlier with slight modifications (Xie *et al.*, 2009; Durgadas *et al.*, 2011). The carboxyl functionality of ASPION was used to conjugate with the amino group of Au-BSA through EDC chemistry thereby forming the hybrid moiety with optical and magnetic properties.

5.3.2 Physico-Chemical & Magnetic Characterization.

5.3.2.1 Determination of Particle Size

The TEM image showed an average particle size of 2 nm for Au clusters and 20 nm for ASPION-Au hybrid system respectively (Figure – 37). The increase in the particle size from 12 nm to 20 nm represents the BSA-Alginate linkage within the Au-SPION hybrid system.

5.3.2.2 X-ray Diffraction Studies (XRD)

The broad band observed at 44.15° (2θ) in the XRD pattern of Au clusters can be attributed to the (200) crystallographic plane as per the JCPDS card no. 4-0784. The XRD pattern of the combined system, ASPION-Au showed both the inverse spinel structure of magnetite with the indices (1 1 1), (2 2 0), (3 1 1), (2 2 2), (4 0 0), (4 2 2), (5 1 1) and (4 4 0) as per the JCPDS Card No. 89-0691 along with the broadness indicating the conjugation of ASPIONS with Au clusters (Figure – 38).

5.3.2.3 Fourier Transform Infra-red spectroscopy (FT-IR)

The characteristic FTIR bands of Au BSA cluster (Figure – 39) at 3451 cm^{-1} can be attributed to the –NH stretching, 1653 cm^{-1} corresponding to the α -helix structure of amine group, 1393 cm^{-1} corresponding to the C-C stretching vibrations of BSA (Xie *et al.*, 2009). A-SPIONs exhibited bands around 3361 , 1621 , 1413 , 1060 and 582 cm^{-1} . The shift in the bands corresponding to the NH stretching of Au cluster and the carboxyl group of ASPION in the FTIR spectra of ASPION-Au well supports the conjugation and the formation of the hybrid system.

5.3.2.4 Magnetic Property

The superparamagnetic nature of the ASPIONs was retained on conjugation with the Au clusters. But the magnetic saturation value of 53 emu/g of A-SPIONs have significantly reduced to 4.9 emu/g in ASPION-Au hybrid system. (Figure – 40). This variation may be due to the lesser inductive effect offered by the Au cluster (Das *et al.*, 2011).

5.3.2.5 Magnetic Relaxivity.

The relaxivity measurements showed variation in the interaction of the ASPIONs with Au clusters in the modified form of ASPION-Au. The relaxation rates experienced a radical reduction and this also may be due to the inductive effect in the hybrid system (Figure – 41). Au being more electronegative than iron, it will experience local charge transfer due to inductive effect which in turn will cause variation in the magnetic property of the SPIONs. Along with this, the paramagnetic nature of Au cluster also influences the superparamagnetic nature of SPIONs, which reduced the relaxation rates to a lower value.

5.3.3 Optical Characterization

The NIR emission range of Au cluster and the ASPION-Au probes does not cause much interference from the tissue autofluorescence of the animal body, which is an advantage in using the probe for *in vivo* application (Figure- 42 - 44). But because the Au cluster are less efficient emitters in term of quantum yield, when compared to commercial dyes like Atto or Cy 5.5, optical images of ASPION-Au demonstrated low fluorescence efficiency of the orders of 10^{-5} .

5.3.4 Hemocompatibility Evaluation

The aggregation and hemolysis study of AuC and ASPION-Au proved the hemocompatible nature of the particles. The results were compared with the earlier reported works and are within the tolerable limit of < 1 % [Murthy *et al.*, 1999; Nimi *et al.*, 2011].

5.3.5 Cell culture studies

5.3.5.1 Cytotoxicity assessment

The % viability of the cells incubated with ASPION-Au increased to about 8 % on comparison with ASPIONs at 100µg/ml. The enhanced non cytotoxic effect of the ASPION-Au may be assigned to the presence of more biocompatible BSA covering over Au which could act as a protein shell over the SPION surface (Figure-46). This enhancement in the viability of the cells can be observed in the previous reported works also (Das *et al.*, 2011). On account of the less fluorescence efficiency of ASPION-Au hybrid system, *in vitro* and *in vivo* imaging experiments were not carried out with this system.

5.4 Preparation of Hybrid nanoprobes using Carbon dots and SPIONs

5.4.1 Synthesis of Hybrid Nanomaterial (ASPION-CDTS & PSPION-CDTS)

The CDTS was prepared based on the previous report with slight modifications (Fang *et al.*, 2012). This method of synthesis has its own advantages like, ease of synthesis, less time consumption and high yield. The prepared CDTS on interaction with amine functionalized ASPIONs yield covalently bonded ASPION-CDTS, which increased the stability and conserved optical and magnetic properties. Considering the enhanced liver targeting capacity of pullulan, without distressing the structural

uniqueness of pullulan, the electrostatic interaction between CDTS and PSPIONs is favoured.

5.4.2 Physico-Chemical & Magnetic Characterization.

5.4.2.1 Determination of Particle Size

TEM micrograph indicates the morphological variation of ASPION-CDTS and PSPION-CDTS from the parental ASPIONs and PSPIONs. TEM image of a single ASPION-CDTS showed the core-shell structure with an average particle size of 20 nm. The earlier reports on hybrid ironoxide and carbon dots also showed the core-shell structure with carbon shell (Wang *et al.*, 2013).The PSPION-CDTS has a honeycomb architecture with an increase in particle size to 90nm (Figure- 47). On close observation of the TEM image, it is clear that the remarkable increase in the particle size of PSPION-CDTS can be attributed to the cluster formation of CDTS over the PSPIONs.

5.4.2.2 X-ray Diffraction Studies (XRD)

The XRD peak at 24.6° corresponding to (002) plane can be indexed to the reflections of graphite (Zhang *et al.*, 2013) and the broadness is due to the smaller particle size of CDTS (Figure-48). The indices of SPIONs along with (002) plane of CDTS present in the diffraction pattern of ASPION-CDTS and PSPION-CDTS favoured the confirmation of the formation of SPION-CDTS hybrid system.

5.4.2.3 Fourier Transform Infra-red spectroscopy (FT-IR)

FTIR Spectra of CDTS showed absorption bands around 3088 cm^{-1} and 992 cm^{-1} corresponding to the –OH stretching and C-H out of plane bending band, 1658 cm^{-1} corresponding to the C=O group and 1356 cm^{-1} corresponding to C-C stretch. The

amine conjugation of ASPIONs and conjugation with CDTS are evident from the FTIR spectra. The bands at 3399 cm^{-1} , 1512 cm^{-1} and 1200 cm^{-1} corresponding to the stretching and bending modes of -NH groups and C-N stretching along with the shift in the Fe-O and C=O band of CDTS indicates the conjugation of ASPION-CDTS. PSPION-CDTS also showed shifts in the Fe-O band of PSPIONs and the -OH band of CDTS indicating the interaction of PSPIONs and CDTS (Figure – 49).

5.4.2.4 Magnetic Property

The superparamagnetic nature of the ASPIONs and PSPIONs were retained on conjugation with the CDTS without any transition. ASPION-CDTS experienced a reduction in the saturated magnetization from 53 to 42 emu/g on conjugation with CDTS. But, a much remarkable reduction is observed in the case of PSPION-CDTS where the magnetic saturation value decreased from 24 to 3.17 emu/g (Figure – 50). This variation may be due to the inductive effect offered by the CDTS (Das *et al.*, 2011). Since the electronegativity of the carbon is higher than iron, the inductive effect played by the carbon will contribute to the decrease in the magnetic property of the hybrid system.

5.4.2.5 Magnetic Relaxivity

The T_2 relaxation rates of both the hybrid systems, ASPION-CDTS and PSPION-CDTS were found to decrease whereas T_1 relaxation rates increased, when compared with the ASPIONs and PSPIONs (Figure – 51). The decrease in the r_2 values and the increase in r_1 values resulted in the reduction of r_2/r_1 ratio. The reason for this may be due to the inductive effect of the more electronegative atom, carbon and its

interaction with ironoxide nanoparticles. Along with this, the deviation in the architecture also might have contributed to this particular result. Carbon being more electronegative atom, on combination with iron atoms, inductive effect can transfer more electron to the iron atom which can cause more shielding effect to the nuclear response of the atoms. This may be the reason for the reduced T_2 effect and increased T_1 effect of the hybrid system. The dual contrast property can be visualized in SPION-CDTS hybrid system which is an added advantage. The simultaneous use of T_1 and T_2 weighted sequences in MR imaging employing the same contrast agent will considerably improve detection accuracy. The dual contrast imaging with monodispersed water-soluble and biocompatible ultrasmall magnetic iron oxide nanoparticles with 3.3 nm diameter generated from a high temperature co-precipitation route were successfully demonstrated by Li and coauthors (Li *et al.*, 2012). The Fe-C hybrid system reported by Wang *et al.*, got high r_2 values where the system was ferromagnetic in nature. (Wang *et al.*, 2014).

5.4.3 Optical Characterization

The optical property of CDTS exhibited an excitation and emission maximum at 405 nm and 500 nm, which provides green emission. Most of the reported carbon based nanoprobes emit in the blue-green range and very few are there with red emission (Anilkumar *et al.*, 2011). ASPION-CDTS and PSPION-CDTS showed high fluorescence intensity at 492 nm emission on exciting at 430nm. The optical imaging efficiency of CDTS remained stable even after conjugation with SPIONs (Figure – 52-56). The very high quantum yield of 20 % determined by the relative method also

favours the *in vitro* and *in vivo* application of the particles. The excitation-emission – efficiency contour plots for the corresponding excitation – emission imaging couldn't extract the full range due to the excitation cut off limitation of the imaging system used.

5.4.4 Hemocompatibility Evaluation

Both the ASPION-CDTS and PSPION-CDTS are found to be hemocompatible in nature, which is a very important property as far as a contrast agent is concerned (Figure – 57). Most of the carbon based nanoprobe reported so far are hemocompatible (Wang *et al.*, 2014).

5.4.5 Cell culture studies

5.4.5.1 Cytotoxicity assessment

The cytocompatibility of SPIONs was maintained on conjugation with CDTS and the % viability of the cells on incubation with ASPION-CDTS and PSPION-CDTS showed a decrease of about 6-7 % only when compared with the respective SPION probes at 100µg/ml (Figure – 58). Previous studies also have reported cell viability of this order (Fang *et al.*, 2012)

5.4.5.2 Cell uptake efficiency

The ASPION-CDTS and PSPION-CDTS showed better uptake efficiency in the confocal images of the L929 cells incubated with the particles for 24 hrs (Figure – 59). The hybrid nanoprobe were found to appear in the cytoplasm of the cells. The result illustrated the prospect of the hybrid probes for cell labeling, cell targeting and cell separation applications. The uptake studies carried out in HEK 293, HepG2, A549 cell

lines by other groups also yielded similar results (Fang *et al.*, 2012; Li *et al.*, 2014) The green fluorescence obtained in the cellular level with high quantum yield recommended the probes for *in vivo* application also.

5.4.6 *In vivo* studies

5.4.6.1 *In vivo* Optical imaging of Hybrid nanoprob.

In vivo imaging on intravenous injection of ASPION-CDTS and PSPION-CDTS showed interference from the autofluorescence emission of the animal study. On extracting the organs, liver had the highest fluorescence, which confirms the hepatic uptake. The relatively high fluorescence in the harvested liver was an indication of high accumulation level of the ASPION-CDTS and PSPION-CDTS (Figure – 60). Since the optical imaging can track the area of concentration of the abnormality at this level, the extend of fibrosis and the iron affinity of Kupffer's cells can only be evaluated through MRI. So the feasibility of the use of ASPION-CDTS and PSPION-CDTS individually as a single probe contrast agent for multimodal imaging has been demonstrated in liver fibrosis model. The studies reported with the green emitting carbon nanoprob demonstrated the *in vivo* image of the subcutaneous administration. For intravenous administration, the fluorescence was observed at the kidneys and in the bladder (Yang *et al.*, 2009). In our study, since the urine in the bladder also give emission in this range, the bladder area was covered during imaging to avoid the undesired signals. Of both the probes used, PSPION-CDTS was found to give better signal *in vivo and ex vivo* which may be due to the highest liver uptake of the probes with the targeting moiety, pullulan.

5.4.7 Histopathological Analysis

The pathological information revealed the early stage of fibrosis in mice model and disruption of the normal nomenclature of the liver through H&E and MT staining (Figure-61). The presence of iron in the liver sections was verified through PB staining procedure. Hepatocyte necrosis and infiltration of mononuclear cells along with extensive nodular formation can be observed in the H& E stained section, which predicts the initial stage of fibrosis. The blue colouration in the MT stained sections substantiates the accumulation of excessive collagen near the central vein which is the indication of the preliminary stage development of hepatic fibrosis.

Chapter 6
SUMMARY & CONCLUSIONS

6. SUMMARY & CONCLUSIONS

6.1 Summary

The advent of nanotechnology in biomedical research contributes the most in the accurate and reliable methods of disease diagnosis. The need of multimodal imaging with a single probe for contrast enhancement of the image is an advanced way for better accuracy in diagnosis. Disease diagnosis at the pertinent stage of the disease is a very important aspect to be considered. The early stage detection of diseases affecting liver, one of the most vital organ in the human body intimately involved in almost every aspect of body's processes, requires foremost attention. Positive contrast enhancement which gives hyperintensity to the site using Gd based contrast agents is the commonly practiced method. Comparing the organ specificity and the safety profile of contrast agents, for liver and lymph node imaging, currently available Gd contrasts are not preferred due to the less uptake by these tissues resulting in the insignificant contrast enhancement which is not sufficient for proper diagnosis. The present work addresses the related issues to a great extent. The major objective of the present exploration was to develop ironoxide based multi modal nanoprobes for liver imaging using Citrate, Dextran, Alginate and Pullulan as surface stabilizers. The other objective was to evaluate the feasibility of the developed MR and optical contrast agents in the early stage detection of liver diseases in animal models. The therapeutic potential of the materials has also been evaluated.

The ironoxide nanoparticles were prepared by co-precipitating iron salts in the presence of NaOH. Utmost care was taken to follow green approach during each stages of the synthesis procedure. These USPIONS of 12 nm core size were surface modified with citrate, the smallest ligand surface stabilizer. Citrate was chosen for surface modification initially to check whether the final system retains all the physico-chemical and magnetic properties of the as prepared C-SPIONs. Since the ultimate aim was for liver imaging, the carbohydrate polymers which show affinity to the liver abnormalities were chosen at later stage for the surface stabilization which included dextran (D-SPIONs), alginate (A-SPIONs) and pullulan (P-SPIONs). The XRD pattern revealed the magnetite phase of the SPIONs and the hydrodynamic diameter revealed about 30 nm for C-SPIONs, 50 nm for D-SPIONs, 40 nm for A-SPIONs and 80 nm for P-SPIONs. FTIR and TGA analysis showed shifts in the corresponding bands in the respective graphs on comparison with the bare USPIONS and polymers. The most important property of magnetic nanoparticles, the magnetic hysteresis was evaluated using VSM. The hysteresis curve confirmed the superparamagnetic nature of USPIONS at room temperature with a high saturation magnetization (M_s), in all the cases. The M_s values varied as 57.5 emu/g for C-SPIONs, 45.8 emu/g for D-SPIONs, 53 emu/g for A-SPIONs and 24.9 emu/g for P-SPIONs. The presence of the surface coating reduced the magnetic property of the systems slightly as reflected in the reduced saturation magnetization compared to 62.7 emu/g of USPIONS. As far as an MR contrast agent is concerned, the relaxivity measurements which gives an idea about how far these materials are efficient in inducing relaxation to the neighbouring protons, have great

importance. The longitudinal and transverse relaxation rates, r_2 and r_1 values obtained for C-SPIONs, D-SPIONs, A-SPIONs and P-SPIONs were 102 & 2.69, 140.7 & 2.5, 117.84 & 3.86 and 146.91 & 2.15 $\text{mM}^{-1}\text{s}^{-1}$ respectively. As the Fe concentration increased, T_1 and T_2 weighted MR images respectively showed increase and decrease in the pixel intensity of the phantom, eventhough the decrease in T_2 weighted images were more appreciable than the increase in the T_1 weighted images favouring the use of the developed materials as T_2 contrast agents. The preliminary evaluation on the heat generation capacity of the SPIONs promises its candidature in hyperthermia application making the developed probes suitable for both imaging and therapy. The temperature raised above 40°C for all the coated SPIONs within 10 minutes of application of 300 to 400A current.

For multimodal contrast agent development, the D-SPIONs, A-SPIONs and P-SPIONs were ultrasonically interacted with the NIR emitting ATTO dye. The NIR emission at 710 nm was retained in the Atto modified USPIONs (DSPIONs-AT, ASPIONs-AT and PSPIONs-AT) favouring the *in vivo* imaging application. Among the hybrid nanomaterials considered, USPIONs conjugated with CDTS with emission around 500 nm were found to be more efficient than Au clusters with emission around 680nm. The comparison of the important properties of all USPION based MR contrast agents developed in this study and their optical imaging potential are summarized in the Table 1.

Probes	Size (nm)	r₂ (mM⁻¹s⁻¹)	r₁ (mM⁻¹s⁻¹)	r₂/r₁ ratio	Zeta Potential(mV)	Excitation Emission (nm)	Fluorescence Efficiency
USPIONs	12	57.11	1.56	36.6	-9.29	-	-
C-SPIONs	12	102	2.69	37.91	-19.6	-	-
DSPION-AT	12	140.7	2.5	56.28	-5.5	675, 710	4.02x10⁻⁴
ASPION-AT	12	117.84	3.86	30.52	-19.9	675, 710	4.60x10⁻⁴
PSPION-AT	12	146.91	2.15	68.33	-5.5	675, 710	4.53x10⁻⁴
CDTS	7-8	-	-	-	-8.3	430,500	1.06x10⁻³
Au BSA	1-2	-	-	-	-11.3	465,680	1.49x10⁻⁴
ASPION-Au	20	4.673	0.91	5.13	-23.4	465,680	1.27x10⁻⁵
ASPION-CDTS	20	21.698	4.0342	5.38	-14.1	430,500	6.65x10⁻⁴

PSPION-CDTS	90	70.895	5.2673	13.5	-3.31	430,500	3.23x10⁻⁴
--------------------	-----------	---------------	---------------	-------------	--------------	----------------	-----------------------------

Table 1 – Comparison of important physical, optical and magnetic properties of different systems developed under this study.

Further *in vitro* and *in vivo* studies were carried out with all the SPIONs based nanoprob es (C-SPIONs, D-SPIONs, A-SPIONs and P-SPIONs), multimodal nanoprob es (DSPION-AT, ASPION-AT and PSPION-AT) and hybrid SPION-CDTS (ASPION-CDTS & PSPION-CDTS) nanoprob es. The biocompatibility evaluation of the developed nanoprob es included both hemocompatibility and cytocompatibility. All the nanoprob es were found to be hemocompatible and cytocompatible.

For the *in vivo* evaluation of the nanoprob es, animal model development for liver fibrosis was the first step. Liver fibrosis was induced in rat model for MR imaging with the periodic injection of CCl₄ and olive oil as per the reported protocol. For optical imaging, mouse model of liver fibrosis was developed. The development of liver fibrosis was indicated by the Liver Function Test (LFT). The animals showed elevated level of liver specific enzymes, SGOT and SGPT corresponding to the early stage of liver disease. Pre and post contrast T₂ weighted coronal MR images of the liver fibrosis induced animals were acquired using a 1.5T clinical MRI. All the four SPIONs based nanoprob es have shown enhanced image contrast of liver through considerable shortening of T₂ relaxation times. This shortening of T₂ relaxation leads to signal drop with the decrease in the pixel intensity at the sites where the SPIONs were accumulated. The contrast efficiency of all the four MR probes was compared with the pre to post contrast percentage signal intensity variation. The percentage signal intensity varied as

39% for C-SPIONs, 55% for D-SPIONs, 44% for A-SPIONs and 67% for P-SPIONs. Thus, considering the contrast enhancement among all the nanoprobe developed in this study, it can be observed that P-SPION provides excellent results. The pre to post contrast signal intensity ratio also depicts the enhanced liver uptake of pullulan coated SPIONs (Figure – 63). On the hypointense liver, the presence of few streaky linear hyperintense areas are visualized corresponding to the fibrotic regions in the affected liver. This further helps in the early diagnosis of liver fibrosis.

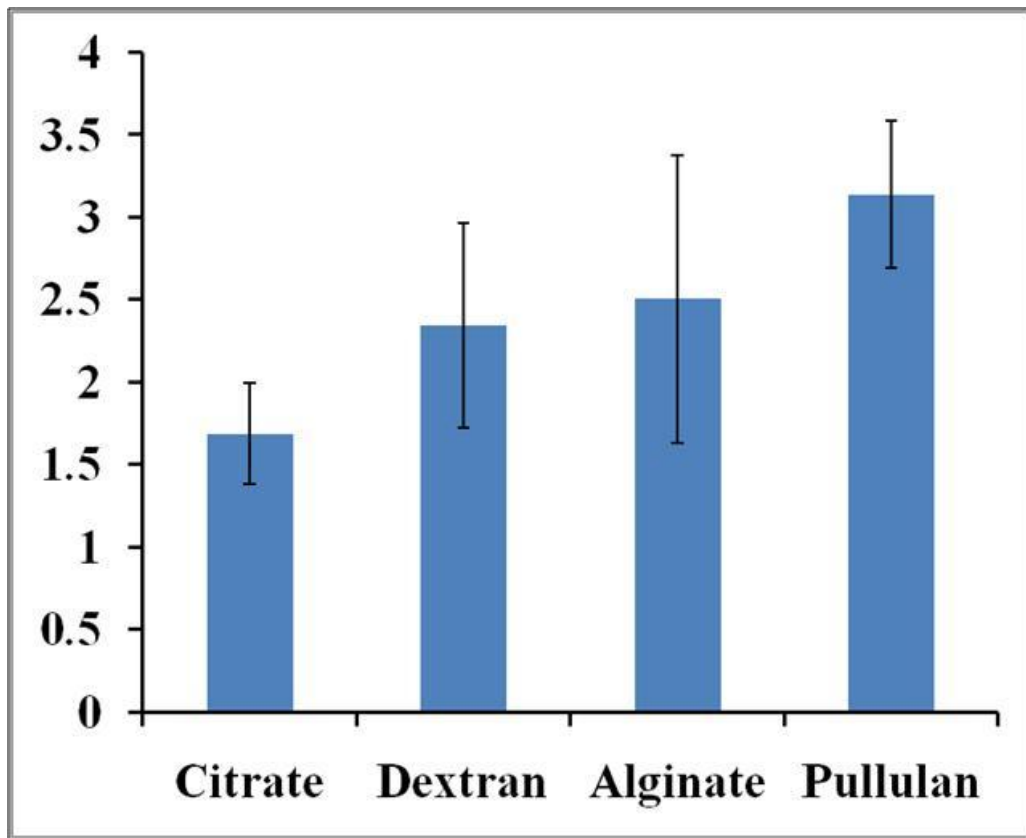


Figure – 63. Comparison of Pre to Post contrast Signal Intensity Ratio of the *in vivo* MR imaging

Optical imaging of fibrosed mice model administered with DSPION-AT, ASPION-AT and PSPION-AT showed intense optical signal at the liver site, indicating the uptake of the particles by the liver and the potential of the materials for liver imaging.. The optical images of the extracted organs also showed high fluorescence intensity in liver. Of the three AT based contrast agents, animals injected with PSPION-AT showed highest efficiency which indicated the highest liver affinity of PSPION-AT. The *in vivo* optical imaging of ASPION-CDTS and PSPION-CDTS administered mouse model showed comparatively high fluorescence intensity at the liver site. In the hybrid material study, tissue penetration of the emitted fluorescence signals had low signal output because the 530 nm range emission of CDTS interfere with the autofluorescence from the animal body. The *ex vivo* liver showed higher fluorescence efficiency. Here also, PSPION-CDTS showed highest efficiency for fluorescence imaging compared to the other two. Histological analysis of liver sections with H&E, MT and PB staining performed after the MR imaging reconfirmed the fibrosis stage and the iron uptake in liver.

6.2 Conclusion

In conclusion, ironoxide based multimodal nanoprobes were successfully synthesized and the *in vivo* MR and optical imaging of liver fibrosis was evaluated. The USPIO based nanoprobes also demonstrated thermal properties required for hyperthermia which is useful for cancer treatment. The work emphasizes on the development of SPION based MR contrast agents, SPION modification with NIR dye and CDTS for multimodal contrast agent for liver targeting. The nanoprobes showed

high level of blood compatibility and less cytotoxicity on liver cells confirming its safety for *in vivo* application. On MRI, the nanoprobe administration improved the contrast difference between the fibrotic tissue and the rest of the extracellular matrix rich hepatic parenchyma at the fibrosis stage. The hyperintense streaks observed in the hypointense fibrotic liver MR image further helps in visualizing the extent of fibrosed tissue as part of the progression of liver disease. Optical imaging was also successful with the signals from the observed liver site on SPION-AT and SPION-CDTS application proving its potential in optical imaging. Comparing *in vivo* application of all the nanoprobe, P-SPION based nanoprobe provided enhanced contrast of liver parenchyma with the discriminative contrast power of fibrosed areas in the early stage of liver abnormalities. Considering all the factors concerned with early detection of liver diseases, P-SPION based nanoprobe can be considered as a new platform for *in vivo* liver imaging. In a preliminary study, all the developed probes were found to be suitable for hyperthermia application also. Thus the materials under this study could be used for theranostic application in future.

6.3 Future prospects

The developed SPION nanoprobe can be used for other biomedical applications like cell sorting, targeted drug delivery and magnetic therapeutic application. These SPION based probes are good candidates for *in vivo* stem cell MRI tracking. Carbon dots (CDTS) developed in the present study can be tuned for NIR emission which in turn will yield better result in the *in vivo* application. Due to the technical limitations, the animal model from same species couldn't be made possible for MR and optical

imaging. The improved technical aspects will favour the multimodal imaging with single probe administration. The detailed toxicological and pharmacokinetic effects of the developed SPION based probes in biological entity has to be studied in detail in future and concentrating more on these aspects may adjoin successful clinical application of the particles.

BIBLIOGRAPHY

Albanese A, Tang P S, Chan W C W (2012) The Effect of Nanoparticle Size, Shape, and Surface chemistry on Biological Systems. *Ann. Rev. Biomed. Engineering* 14: 1-16.

Ali I, Wani W A and Saleem K (2011) Cancer Scenario in India with Future Perspectives. *Cancer Therapy*. 8: 56-70.

Anilkumar P, Wang X, Cao Li, Sahu S, Liu J H, Wang P, Korch K, Tackett II K N, Parenzan A and Sun Y P (2011) Toward quantitatively fluorescent carbon-based “quantum” dots. *Nanoscale*. 3: 2023-7.

Bae H, Ahmad T, Rhee I, Chang Y, Jin S U and Hong S (2012) Carbon-coated iron oxide nanoparticles as contrast agents in magnetic resonance imaging. *Nanoscale Res. Lett.* 7:44.

Bautista M C, Bomati-Miguel O, Morales M P, Serna C J, Veintemillas-Verdaguer S (2005) Surface characterization of dextran-coated iron oxide nanoparticles prepared by laser pyrolysis and coprecipitation. *J. Magn. Magn. Matter*. 293: 20-27.

Bera D, Qian L, Tseng T K and Holloway P H (2010) Quantum Dots and Their Multimodal Applications: A Review . *Materials*. 3: 2260-2345.

Bernstein E J, Lauber C S, Kay J (2012) Nephrogenic systemic fibrosis: A systemic fibrosing disease resulting from gadolinium exposure. *Best Practice & Research Clinical Rheumatology*. 26 (4): 489-503.

Berry C C and Curtis A S G (2003) Functionalization of magnetic nanoparticles for applications in biomedicine. *J. Phys. D Appl. Phys*. 36: R198-R206.

Bertorelle F, Wilhelm C, Roger J, Gazeau F, Me'nager C and Cabuil V (2006) Fluorescence-Modified Superparamagnetic Nanoparticles: Intracellular Uptake and Use in Cellular Imaging. *Langmuir*. 22: 5385-5391.

Bourlinos A B, Stassinopoulos A, Anglos D, Zboril R, Georgakilas V, and Giannelis E P. (2008) Photoluminescent Carbogenic Dots. *Chem. Mater*. 20: 4539–4541.

Brust M, Walker M, Bethell D, Schiffrin D J and Whyman R (1994) Synthesis of Thiol-derivatised Gold Nanoparticles in a Two-phase Liquid-Liquid System. *J. Chem. Soc., Chem. Commun*. 801-802.

Bulte J W M and Kraitchman D L (2004) Iron oxide MR contrast agents for molecular and cellular imaging. *NMR Biomed*. 17:484–499.

Cao L, Yang S T, Wang X, Luo P G, Liu J H, Sahu S, Liu Y, Sun Y P (2012) Competitive Performance of Carbon “Quantum” Dots in Optical Bioimaging. *Theranostics* 2: 295-301.

Carp O, Patron L, Culita D C, Budrugaec P, Feder M, Diamandescu L (2010) Thermal analysis of two types dextran-coated magnetite. *J Therm Anal Calorim*. 101:181–7.

Castillo A S, Avidad M A, Pritz C, Robles M C, Ferná'ndez B, Rama M J R, Ferná'ndez A M, Ferná'ndez A L, Gonzalez F S, Fischerb A S and Vallveya L F C (2013) Carbon dots for copper detection with down and upconversion fluorescent properties as excitation sources. *Chem. Commun*. 49: 1103-1105.

Cha E J, Jang E S, Sun I C, Lee I J, Ko J H, Kim Y I, Kwon I C, Kim K, Ahn C H (2011) Development of MRI/NIRF ‘activatable’ multimodal imaging probe based on iron oxide nanoparticles. *J. Controlled Release*. 155:152–158.

- Chao J I, Perevedentseva E, Chung P H, Liu KK, Cheng C Y, Chang C C, and Chengy C L (2007) Nanometer-Sized Diamond Particle as a Probe for Biolabeling. *Biophysical Journal* 93(6): 2199–2208.
- Chen J, Zhang Q F, Bonaccorso T A, Williard P G, and Wang L S (2014) Controlling Gold Nanoclusters by Diphospine Ligands. *J. Am. Chem. Soc.* 136: 92–95.
- Cheraghipour E, Javadpour S and Mehdizadeh A R (2012) Citrate capped superparamagnetic iron oxide nanoparticles used for hyperthermia therapy. *J Biomed Sci Eng.* 5: 715-719.
- Chertok B, David A E and Yang V C (2010) Polyethyleneimine-modified iron oxide nanoparticles for brain tumor drug delivery using magnetic targeting and intra-carotid administration. *Biomaterials.* 31: 6317-6324.
- Chevrier D M, Chatt A and Zhang P (2012) Properties and applications of protein-stabilized fluorescent gold nanoclusters: short review. *J Nanophoton.* 6(1): 064504-1.
- Chung E Y, Kima H M, Lee G H, Kwak B K, Jung J S, Kuh H J, Lee J (2012) Design of deformable chitosan microspheres loaded with superparamagnetic iron oxide nanoparticles for embolotherapy detectable by magnetic resonance imaging. *Carbohydr. Polym.* 90: 1725– 1731.
- Constandinou C, Henderson N & Iredale J P (2005) Modeling liver fibrosis in rodents. *Methods Mol Med,* 117: 237-250.

Corr S A, Byrne A O, Gun'ko Y K, Ghosh S, Brougham D F, Mitchell S, Volkov Y and Mello A P (2006) Magnetic-fluorescent nanocomposites for biomedical multitasking. *Chem. Commun.* 4474–4476.

Corr S A, Rakovich Y P and Gun'ko Y K (2008) Multifunctional Magnetic-fluorescent Nanocomposites for Biomedical Applications., *Nanoscale Res Lett.* 3:87–104.

Das M, Mishra D, Dhak P, Gupta S, Maiti T K, Basak A and Pramanik P (2009) Biofunctionalized, Phosphonate-Grafted, Ultrasmall Iron Oxide Nanoparticles for Combined Targeted Cancer Therapy and Multimodal Imaging. *Small*.5(24): 2883–2893.

Davis M E, Chen Z G and Shin D M (2008) Nanoparticle therapeutics: an emerging treatment modality for cancer. *Nature Reviews drug discovery.* 7:771-782.

Douma K, Prinzen L, Slaaf D W, Reutelingsperger C P M, Biessen E A L, Hackeng T M, Post M J, and van Zandvoort M A M J (2009) Nanoparticles for Optical Molecular Imaging of Atherosclerosis. *Small.* 5(5): 544–557.

Duan H, Kuang M, Wang X, Wang Y A, Mao H, and Nie S (2008) Reexamining the Effects of Particle Size and Surface Chemistry on the Magnetic Properties of Iron Oxide Nanocrystals: New Insights into Spin Disorder and Proton Relaxivity. *J. Phys. Chem. C,* 112: 8127–8131.

Durgadas C V, Sharma C P and Sreenivasan K (2011) Fluorescent gold clusters as nanosensors for copper ions in live cells. *Analyst.* 136: 933-940.

Durgadas C V, Sharma C P and Sreenivasan K (2011) Fluorescent gold clusters as nanosensors for copper ions in live cells. *Analyst.* 136: 933-940.

Fang Y, Guo S, Li D, Zhu C, Ren W, Dong S, and Wang E (2012) Easy Synthesis and Imaging Applications of Cross-Linked Green Fluorescent Hollow Carbon Nanoparticles. *ACSNano*.6(1);400-409.

Feest T G (1976) Low molecular weight dextran: a continuing cause of acute renal failure. *British medical journal*, 2(6047), 1300.

Ferrari M (2005) Cancer Nanotechnology: Opportunities And Challenges. *Nature Reviews Cancer*. 5:161-171.

Gao H, Cai Y, Zhou J, Xie X, Ouyang W, Zhang Y, Wang X, Zhang X, Wang X, Zhao L, Tang J (2010) Pullulan acetate coated magnetite nanoparticles for hyper-thermia: Preparation, characterization and *in vitro* experiments. *Nano Res*. 3(1) : 23-31.

Gao L, Xie L, Long X, Wang Z, He C Y, Chen Z Y, Zhang L, Nan X, Lei H, Liu X, Liu G, Lu J, Qiu B (2013) Efficacy of MRI visible iron oxide nanoparticles in delivering minicircle DNA into liver via intrabiliary infusion. *Biomaterials*. 34: 3688-3696.

George J and Chandrakasan G (2000) Biochemical Abnormalities during the Progression of Hepatic Fibrosis Induced by Dimethylnitrosamine. *Clinical Biochemistry*. 33(7): 563–570.

Geraldes C F G C and Laurent S (2009) Classification and basic properties of contrast agents for magnetic resonance imaging. *Contrast Media Mol. Imaging*, 4: 1–23.

Goh E J, Kim K S, Kim Y R, Jung H S, Beack S, Kong W H, Scarcelli G, Yun S H, and Hahn S K (2012) Bioimaging of Hyaluronic Acid Derivatives Using Nanosized Carbon Dots. *Biomacromolecules*. 13: 2554–2561.

Goya G F, Berquo T S, Fonseca F C (2003) Static and dynamic magnetic properties of spherical magnetite nanoparticles. *J Appl Phys.* 94(5):3520–8.

Gupta A K & Wells S (2004) Surface-modified superparamagnetic nanoparticles for drug delivery: Preparation, characterization, and cytotoxicity studies. *Ieee Trans.on Nanobiosci.*, 3(1): 66-73.

Guy C and Ffytche D (2005) *An Introduction to the Principles of Medical Imaging.* Imperial College Press, London.

Haacke E M, Brown R B, Thompson M R (1999) *Magnetic Resonance Imaging: Physical Principles and Sequence Design.* John Wiley & Sons, Newyork.

Hashemi R H, Bradley W G and Lisanti C J (2010) *MRI: The Basics*, 3rd Edition. Lippincott Williams & Wilkins.

Hou C H, Hou S M, Hsueh Y S, Lin J, Wu H C, Lin F H (2009) The *in vivo* performance of biomagnetic hydroxyapatite nanoparticles in cancer hyperthermia therapy. *Biomaterials.* 30: 3956–3960.

Hu D, Sheng Z, Gong P, Zhanga P and Cai L (2010) Highly selective fluorescent sensors for Hg²⁺ based on bovine serum albumin-capped gold nanoclusters. *Analyst.* 135: 1411–1416.

Huang G, Sayed M A E (2010) Gold nanoparticles: Optical properties and implementations in cancer diagnosis and photothermal therapy., *Journal of Advanced Research* 1: 13–28.

Huang H S and Hainfeld J F (2013) Intravenous magnetic nanoparticle cancer hyperthermia. *Int J Nanomedicine.*8: 2521–2532.

Hui-li Ma, Xian-rong Qi, Yoshie Maitani and Tsuneji Nagai (2007) Preparation and characterization of superparamagnetic iron oxide nanoparticles stabilized by alginate. *Int. J. of Pharm.* 333: 177–186.

Husein M M and Nassar N N (2008) Nanoparticle Preparation Using the Single Microemulsions Scheme. *Current Nanoscience.* 4: 370-380.

Ibrahim M, Serrano K G, Noe L, Garcia C, Verelst M (2009) Electroprecipitation of magnetite nanoparticles: an electrochemical study. *Electrochimica Acta.* 55(1):155-158.

Jain R K and Stylianopoulos T (2010) Delivering nanomedicine to solid tumors. *Nat Rev Clin Oncol.* 7(11): 653–664.

Jemal A, Bray F, Center M M, Ferlay J, Ward E, Forman D (2011) Global cancer statistics. *Cancer J Clin.* 61(2):69-90.

Jenkins J T, Halaney D L, Sokolov K V, Ma L L, Shipley H J, Mahajana S, Loudon C L, Asmis R, Milner T E, Johnston K P, Feldman M D (2013) Excretion and toxicity of gold–iron nanoparticles. *Nanomed Nanotech Biol Med.* 9: 356–365.

Jiang S, Gnanasammandhan M K and Zhang Y (2010) Optical imaging-guided cancer therapy with fluorescent nanoparticles. *J. R. Soc. Interface* 7: 3–18.

Jin L, Weinberger D S, Melaimi M, Moore C E, Rheingold A L and Bertrand G (2014) Trinuclear Gold Clusters Supported by Cyclic (alkyl)(amino)carbine Ligands: Mimics for Gold Heterogeneous Catalysts. *Angew. Chem. Int. Ed.* 53: 9059 –9063.

Joshi B P and Wang T D (2010) Exogenous Molecular Probes for Targeted Imaging in Cancer: Focus on Multi-modal Imaging. *Cancers* 2: 1251-1287.

Kaneo Y, Tanaka T, Nakano T, Yamaguchi Y (2001) Evidence for receptor-mediated hepatic uptake of pullulan in rats. *J Controlled Release*.70: 365–373.

Kathryn M. L. Pashow T, Rocca W J D, Huxforda W R C and Lin W (2010) Hybrid nanomaterials for biomedical applications. *Chem. Commun.* 46: 5832–5849.

Kim B H, Lee N, Kim H, An K, Park Y I, Choi Y, Shin K, Lee Y, Kwon S G, Na H B, Park Je G, Ahn T Y, Kim Y W, Moon W K, Choi S H and Hyeon T (2011) Large-Scale Synthesis of Uniform and Extremely Small-Sized Iron Oxide Nanoparticles for High-Resolution T1 Magnetic Resonance Imaging Contrast Agents. *J. Am. Chem. Soc.* 133: 12624 - 12631.

Kim D K, Mikhaylova M, Wang F H, Kehr J, Bjelke B, Zhang Y, Tsakalacos T , and Muhammed M (2003) Starch-coated superparamagnetic nanoparticles as MR contrast agents. *Chem. Mater.* 15(23): 4343–4351.

Kim D K, Mikhaylova M, Wang F H, Kehr J, Bjelke B, Zhang Y, Tsakalacos T and Muhammed M (2003) Starch-Coated Superparamagnetic Nanoparticles as MR Contrast Agents. *Chem. Mater.* 15: 4343-4351.

Kim D K, Zhang Y, Voit W, Rao K V, Muhammed M (2001) Synthesis and characterization of surfactant-coated superparamagnetic monodispersed iron oxide nanoparticles., *J. Magn. Mater.* 225 : 30-36.

Kim H, Achermann M, Balet L P, Hollingsworth J A and Klimov V I (2005) Synthesis and Characterization of Co/CdSe Core/Shell Nanocomposites: Bifunctional Magnetic-Optical Nanocrystals. *J. Am. Chem. Soc.* 127: 544-546.

Kircher M F, Mahmood U, King R S, Weissleder R and Lee Josephson (2003) A Multimodal Nanoparticle for Preoperative Magnetic Resonance Imaging and Intraoperative Optical Brain Tumor Delineation. *CANCER RESEARCH*, 63: 8122–8125.

Kircher M F, Mahmood U, King R S, Weissleder R, and Josephson L (2003) A Multimodal Nanoparticle for Preoperative Magnetic Resonance Imaging and Intraoperative Optical Brain Tumor Delineation. *Cancer Res.* 63:8122-8125.

Ko H Y, Chang Y W, Paramasivam G, Jeong M S, Cho S and Kim S (2013) *In vivo* imaging of tumour bearing near-infrared fluorescence-emitting carbon nanodots derived from tire soot. *Chem. Commun.* 49: 10290-10292.

Kotsmar C, Yoon K Y, Yu H, Ryoo S Y, Barth J, Shao S, Prodanovic M, Milner T E, Bryant S L, Huh C and Johnston K P (2010) Stable Citrate-Coated Iron Oxide Superparamagnetic Nanoclusters at High Salinity. *Ind. Eng. Chem. Res.* 49: 12435–12443.

Laurent S, Forge D, Port M, Roch A, Robic C, Vander Elst L, Muller RN (2008) Magnetic iron oxide nanoparticles: synthesis, stabilization, vectorization, physicochemical characterizations, and biological applications. *Chem Rev* 108(6):2064-110.

Le Naour F, Sandt C, Peng C Y, Trcera N, Chiappini F, Flank A M, Guettier C, & Dumas P (2012) In Situ Chemical Composition Analysis of Cirrhosis by Combining Synchrotron Fourier Transform Infrared and Synchrotron X-ray Fluorescence Microspectroscopies on the Same Tissue Section. *Analytical Chemistry*. 84(23): 10260-10266.

Lee H Y, Lee S H, Xu C, Xie J, Lee J H, Wu B, Koh A L, Wang X, Sinclair R, Wang S X, Nishimura D G, Biswal S, Sun S, Cho S H and Chen X (2008) Synthesis and characterization of PVP-coated large core iron oxide nanoparticles as an MRI contrast agent. *Nanotechnology*. 19: 165101-7.

Lee S and Chen X (2009) Dual-Modality Probes for *In Vivo* Molecular Imaging, *Molecular Imaging*. 8(2) : 87–100.

Leung K C F, Xuan S, Zhu X, Wang D, Chak C P, Lee S F, Ho W K W and Chung B C T (2012) Gold and iron oxide hybrid nanocomposite materials. *Chem. Soc. Rev.* 41: 1911–1928.

Li C L, Ou C M, Huang C C, Wu W C, Chen Y P, Lin T E, Ho L C, Wang C W, Shih C C, Zhou H C, Lee Y C, Tzeng W F, Chiou T J, Chu S T, Cangm J and Chang H T (2014) Carbon dots prepared from ginger exhibiting efficient inhibition of human hepatocellular carcinoma cells. *J. Mater. Chem. B*. 2: 4564-4571.

Li J, Zhou Y, Li M, Xia N, Huang Q, Do H, Liu Y N, Zhou F (2011) Carboxymethylated dextran-coated magnetic iron oxide nanoparticles for regenerable bioseparation., *J Nanosci Nanotechnol*. 11:10187-92.

Li Q, Tang G, Xue S, He X, Miao P, Li Y, Wang J, Xiong L, Wang Y, Zhang C and Yang G Y (2013) Silica-coated superparamagnetic iron oxide nanoparticles targeting of EPCs in ischemic brain injury. *Biomaterials*. 34: 4982-4992.

Li Z, Wang C, Cheng L, Gong H, Yin S, Gong Q, Li Y, Liu Z (2013) PEG-functionalized iron oxide nanoclusters loaded with chlorin e6 for targeted, NIR light induced, photodynamic therapy. *Biomaterials*. 34: 9160-9170.

Li Z, Yi P W, Sun Q, Lei H, Zhao H L, Zhu Z H, Smith S C, Lan M B, Lu G Q M (2012) Ultrasmall water-soluble and biocompatible magnetic iron oxide nanoparticles as positive and negative dual contrast agents. *Adv. Funct. Mater.* 22: 2387–2393.

Lin C A J, Lee C H, Hsieh J T, Wang H H, Li J K, Shen J L, Chan W H, Yeh H I, Chang W H (2009) Synthesis of Fluorescent Metallic Nanoclusters toward Biomedical Application: Recent Progress and Present Challenges. *J. Med. and Bio. Eng.* 29(6): 276-283.

Link S and Sayed M A E (1999) Size and Temperature Dependence of the Plasmon Absorption of Colloidal Gold Nanoparticles. *J. Phys. Chem. B*. 103: 4212-4217.

Liu H L, Ko S P, Wu J H, Jung M H, Min J H, Lee J H, An B H, Kim Y K (2007) One-pot polyol synthesis of monosize PVP-coated sub-5nm Fe₃O₄ nanoparticles for biomedical applications. *J. Magn. Magn. Mater.* 310: 815–817.

Liu Y, Ai K, Cheng X, Huo L and Lu L (2010) Gold-Nanocluster-Based Fluorescent Sensors for Highly Sensitive and Selective Detection of Cyanide in Water. *Adv. Funct. Mater.* 20: 951–956.

Lu A H, Salabas E L, and Schth F (2007) Magnetic Nanoparticles: Synthesis, Protection, Functionalization, and Application. *Angew. Chem. Int. Ed.* 46: 1222 – 1244.

Lu H, Yi G, Zhao S, Chen D, Guo L H and Cheng J (2004) Synthesis and characterization of multi-functional nanoparticles possessing magnetic, up-conversion fluorescence and bio-affinity properties. *J. Mater. Chem.* 14: 1336 – 1341.

Lu Y, Yin Y, Mayers B T and Xia Y(2002) Modifying the Surface Properties of Superparamagnetic Iron Oxide Nanoparticles through A Sol-Gel Approach. *Nano Lett.* 2(3): 2002.

Luker & Luker (2008) Optical Imaging: Current Applications and Future Directions. *J Nucl Med.* 49:1–4.

Luo P G, Sahu S, Yang S T, Sonkar S K, Wang J, Wang H, LeCroy G E, Cao Le and Sun Y P (2013) Carbon “quantum” dots for optical bioimaging. *J. Mater. Chem. B.* 1: 2116–2127.

Mahmoudi M, Simchi A and Imani M (2009) Cytotoxicity of Uncoated and Polyvinyl Alcohol Coated Superparamagnetic Iron Oxide Nanoparticles. *J. Phys. Chem. C.* 113: 9573–9580.

Mahmoudi M, Stroeve P, Milani A S, Arbab A S (2011) Superparamagnetic Iron Oxide Nanoparticles: Synthesis, Surface Engineering, Cytotoxicity & Biomedical Applications. Nova publishers.

Manju S, Sharma C P & Sreenivasan K (2011) Targeted coadministration of sparingly soluble paclitaxel and curcumin into cancer cells by surface engineered magnetic nanoparticles. *J Mater. Chem.*, 21(39): 15708-15717.

MICAD Research Team (2006) Citrate-coated (184th variant) very small superparamagnetic iron oxide particles. In: *Molecular Imaging and Contrast Agent Database (MICAD)* [Internet]. Bethesda (MD): National Center for Biotechnology Information (US); 2004-2013.

Mohammad R K and Islam S (2011) Thermal Behavior with Mechanical Property of Fluorinated Silane Functionalized Superhydrophobic Pullulan/Poly(vinyl alcohol) Blends by Electrospinning Method. *J. Nanomaterials*. 979458: 7.

Montet X, Ntziachristos V, Grimm J, and Weissleder R (2005) Tomographic Fluorescence Mapping of Tumor Targets. *Cancer Res*. 65: (14) 6330-6.

Morgan T O, Little J M & Evans W A (1966) Renal failure associated with low-molecular-weight dextran infusion. *British Medical Journal*, 2(5516): 737-739.

Morjan I, Dumitrache F, Alexandrescu R, Birjega R, Fleaca C, Voicu I, Gavrila L, Soare I, Filotti G, Kuncser V and Ciupina V (2007) Nanoscale Maghemite Iron Oxide Powders Prepared by Laser Pyrolysis. 4: 234-237.

Mua Q, Yang L, Davis J C, Vankayala R, Hwang K C, Zhao J, Yan B (2010) Biocompatibility of polymer grafted core/shell iron/carbon nanoparticles. *Biomaterials*. 31: 5083-5090.

Mundry K M, Plonsey R, Bronzino J (2003) *Biomedical imaging*. CRC press.

Murthy N, Robichaud J R, Tirrell D A, Stayton P S, Hoffmana A S (1999) The design and synthesis of polymers for eukaryotic membrane disruption. *J. Controlled Release.* 61: 137–143.

Na H B, Song I C, and Hyeon T (2009) Inorganic Nanoparticles for MRI Contrast Agents., *Adv. Mater.* 21:2133–2148.

Nair L V , Philips D S, Jayasree R S and Ajayaghosh A (2013) A Near-Infrared Fluorescent Nanosensor (AuC@Urease) for the Selective Detection of Blood Urea. *Small.* 9(16): 2673–2677.

Negishi Y, Takasugi Y, Sato S, Yao H, Kimura K, Tsukuda T (2004) Magic-numbered Au(n) clusters protected by glutathione monolayers (n = 18, 21, 25, 28, 32, 39): isolation and spectroscopic characterization. *J. Am. Chem. Soc.* 126: 6518 – 6519.

Nicole L , Rozes L and Sanchez C (2010) Integrative Approaches to Hybrid Multifunctional Materials: From Multidisciplinary Research to Applied Technologies. *Adv. Mater.* 22: 3208–3214.

Nidhin M, Shaiju Nazeer S S, Jayasree R S, Kiran M S, Nair B U, Sreeram K J (2013) Flower shaped assembly of cobalt ferrite nanoparticles: application as T2 contrast agent in MRI. *RSC Advances.* 3 (19): 6906-6912.

Nigam S, Barick K C, Bahadur D (2011) Development of citrate-stabilized Fe₃ O₄ nanoparticles: conjugation and release of doxorubicin for therapeutic applications. *J. Magn. Mater.* 323 (2): 237-243.

Nimi N, Paul W & Sharma C P (2011) Blood protein adsorption and compatibility studies of gold nanoparticles. *Gold Bull.* 44:15–20.

Nune S K, Gunda P, Thallapally P K, Lin Y Y, Forrest Y L, and Berkland C J (2009) Nanoparticles for biomedical imaging. *Expert Opin Drug Deliv.* 6(11): 1175–1194.

Qin J, Li K, Peng C, Li X, Lin J, Ye K, Yang X, Xie Q, Shen Z, Jin Y, Jiang M, Zhang G, Lu X (2013) MRI of iron oxide nanoparticle-labeled ADSCs in a model of hindlimb ischemia. *Biomaterials.* 34: 4914-4925.

Qin W, Lohrman J, and Ren S (2014) Magnetic and Optoelectronic Properties of Gold Nanocluster–Thiophene Assembly. *Angew. Chem. Int. Ed.* 53: 7316–7319.

Qu S, Wang X, Lu Q, Liu X, and Wang L (2012) A Biocompatible Fluorescent Ink Based on Water-Soluble Luminescent Carbon Nanodots., *Angew. Chem. Int. Ed.* 51; 12215–12218.

Ralph Weissleder (2006) Molecular Imaging in Cancer. *Science.* 312: 1168-1171.

Reimer P, Weissleder R, Lee AS, Buettner S, Wittenberg J, Brady TJ (1991) Asialoglycoprotein receptor function in benign liver disease: evaluation with MR imaging. *Radiology.* 1991 178(3):769-74.

Saboktakin M R, Tabatabaie R M, Maharramov A, Ramazanov M A (2010) A synthetic macromolecule as MRI detectable drug carriers: Aminodextran-coated iron oxide nanoparticles. *Carbohydr. Polym.* 80: 695–698.

Sailor M J and Park J H (2012) Hybrid Nanoparticles for Detection and Treatment of Cancer. *Adv. Mater.* 24: 3779–3802.

Saraswathy^a A, Shaiju S N, Madhumol J, Nimi N, Sabareeswaran A, Varma PRH, Jayasree R S (2014) Citrate coated iron oxide nanoparticles with enhanced relaxivity for *in vivo* Magnetic Resonance Imaging of liver fibrosis. *Colloids Surf., B: Biointerfaces*.117: 216–224.

Saraswathy^b A, Shaiju S N, Nimi N, Sabareeswaran A, Sachin J S, Jayasree R S (2014) Synthesis and characterization of Dextran stabilized superparamagnetic iron oxide nanoparticles for *in vivo* MR imaging of liver fibrosis. *Carbohydr. Polym.* 101:760–768.

Shi W, Zeng H, Sahoo Y, Ohulchanskyy T Y, Ding Y, Wang Z L, Swihart M and Prasad P N (2006) A General Approach to Binary and Ternary Hybrid Nanocrystals. *Nano Lett.*, 6(4):875-881.

Shichibu Y, Negishi Y, Tsunoyama H, Kanehara M, Teranishi T and Tsukuda T (2007) Extremely High Stability of Glutathionate-Protected Au₂₅ Clusters Against Core Etching. *Small*. 3: 835–839.

Silva A C, Oliveira T R, Mamani J B, Malheiros S M, Malavolta L, Pavon L F, Sibov T T, Amaro E Jr, Tannús A, Vidoto E L, Martins M J, Santos R S, Gamarra L F (2011) Application of hyperthermia induced by superparamagnetic iron oxide nanoparticles in glioma treatment., *Int. J Nanomedicine*. 6: 591–603.

Simberg D, Park J H, Karmali P P, Zhang W M, Merkulov S, McCrae K, Bhatia S N, Sailor M, & Ruoslahti E (2009) Differential proteomics analysis of the surface heterogeneity of dextran iron oxide nanoparticles and the implications for their *in vivo* clearance. *Biomaterials*. 30(23-24): 3926-3933.

Smith A M, Duan H, Mohs A M, Nie S (2008) Bioconjugated quantum dots for *in vivo* molecular and cellular imaging. *Advanced Drug Delivery Reviews*. 60: 1226–1240.

Soares J P, Santos J E, Chierice G O, Cavaleiro E T G (2004) Thermal behavior of alginic acid and its sodium salt. *Ecl. Quím., São Paulo*, 29(2): 53-56.

Sodipo B K, and Aziz A A (2013) Sonochemical Synthesis of Silica Coated Super Paramagnetic Iron Oxide Nanoparticles. *Materials Science Forum* 756 : 74-79.

Soptei B, Mihaly J, Visy J, Wacha A and Bota A (2014) Intercalation of Bovine Serum Albumin Coated Gold Clusters Between Phospholipid Bilayers: Temperature-Dependent Behavior of Lipid-AuQC@BSA Assemblies with Red Emission and Superlattice Structure. *J. Phys. Chem. B*. 118: 3887–3892.

Srivastava A, Singh P, Gunjekar V G, Sinha A P B (1985) Study of the thermal decomposition of iron and barium citrates. *Thermochim. Acta* 86 : 77-84.

Stefanescu R, Born R, Moise A, Ernst B, Przybylski M (2011) Epitope structure of the carbohydrate recognition domain of asialoglycoprotein receptor to a monoclonal antibody revealed by high-resolution proteolytic excision mass spectrometry. *J Am Soc Mass Spectrom*. 22(1):148-57.

Sun S and Zeng H (2002) Size-Controlled Synthesis of Magnetite Nanoparticles. *J. Am. Chem. Soc*. 124: 8204-8205.

Sun Y P, Zhou B, Lin Y, Wang W, Fernando K A S, Pathak P, Meziani M J, Harruff B A, Wang X, Wang H, Luo P G, Yang H, Kose M E, Chen B, Veca L M and Xie S Y (2006) Quantum-Sized Carbon Dots for Bright and Colourful Photoluminescence. *J. Am. Chem. Soc*. 128 (24): 7756–7757.

Takami S, Sato T, Mousavand T, Ohara S, Umetsu M, Adschiri T (2007) Hydrothermal synthesis of surface-modified iron oxide nanoparticles. *Materials Letters*. 61: 4769–4772.

Talwalkar J A, Yin M, Fidler J L, Sanderson S O, Kamath P S and Ehman R L (2008) Magnetic Resonance Imaging of Hepatic Fibrosis: Emerging Clinical Applications. *Hepatology*. 47(1), 332-342.

Tao H, Yang K, Ma Z, Wan J, Zhang Y, Kang Z, and Liu Z (2012) *In Vivo* NIR Fluorescence Imaging, Biodistribution, and Toxicology of Photoluminescent Carbon Dots Produced from Carbon Nanotubes and Graphite. *Small*. 8(2): 281–290.

Tao H, Yang K, Ma Z, Wan J, Zhang Y, Kang Z, and Liu Z (2012) *In Vivo* NIR Fluorescence Imaging, Biodistribution, and Toxicology of Photoluminescent Carbon Dots Produced from Carbon Nanotubes and Graphite. *Small*. 8(2): 281–290.

Tartaj P, Morales M P, Verdaguer S V, Carre T G and Serna C J (2003) The preparation of magnetic nanoparticles for applications in biomedicine. *J. Phys. D: Appl. Phys.* 36: 182–197.

Taylor A, Krupskaya Y, Costa S, Kramer S O K, Fussel S, Klingeler R, Buchner B, Palen E B, Wirth M P (2010) Functionalization of carbon encapsulated iron nanoparticles. *J Nanopart Res.* 12:513–519.

Teng X, Black D, Watkins N J, Gao Y and Yang H (2003) Platinum-Maghemite Core-Shell Nanoparticles Using a Sequential Synthesis. *Nano Lett.* 3(2): 261–264.

Torres M M, Jain T K, Labhasetwar V, Pelecky D L (2005) Magnetic studies of iron oxide nanoparticles coated with oleic acid and Pluronic® block copolymer. *J. Appl. Phys.* 97, 10Q905(1-3).

Van de Bovenkamp M, Groothuis G M, Meijer D K, Olinga P (2007) Liver fibrosis *in vitro*: cell culture models and precision-cut liver slices. *Toxicol In Vitro.* 21:545-57.

Verma A, Stellacci F (2010) Effect of surface properties on nanoparticle-cell interactions. *Small.* 6 (1):12-21.

Vlasov I I, Shiryaev A A, Rendler T, Steinert S, Lee S Y, Antonov D, Voros M, Jelezko F, Fisenk A V, Semjonova L F, Biskupek J, Kaiser U, Lebedev O I, Sildos I, Hemmer P R, Konov V I, Gali A and Wrachtrup J (2014) Molecular-sized fluorescent nanodiamonds. *Nature Nanotechnology* 9: 54-58.

Wan J Q, Jiang X H, Li H, & Chen K Z (2012) Facile synthesis of zinc ferrite nanoparticles as non-lanthanide T-1 MRI contrast agents. *Journal of Materials Chemistry.* 22(27): 13500-13505.

Wang H, Shen J, Li Y, Wei Z, Cao G, Gai Z, Hong K, Banerjee P and Zhou S (2014) Magnetic iron oxide–fluorescent carbon dots integrated nanoparticles for dual-modal imaging, near-infrared light-responsive drug carrier and photothermal therapy. *Biomater. Sci.* 2: 915.

Wang H, Shen J, Li Y, Wei Z, Cao G, Gai Z, Hong K, Banerjee P and Zhou S (2014) Magnetic iron oxide–fluorescent carbon dots integrated nanoparticles for dual-modal imaging, near-infrared light-responsive drug carrier and photothermal therapy. *Biomater. Sci.* 2: 915-923.

Wang X, Qu K, Xu B, Rena J and Qu X (2011) Microwave assisted one-step green synthesis of cell-permeable multicolor photoluminescent carbon dots without surface passivation reagents. *J. Mater. Chem.* 21: 2445-2450.

Wang Y J (2011) Superparamagnetic iron oxide based MRI contrast agents: Current status of clinical application. *Quantitative Imaging in Medicine and Surgery.* 1(1) : 35–40.

Weinstein J S, Varallyay C G, Dosa E, Gahramanov S, Hamilton B, Rooney W D, Muldoon L L & Neuwelt E A (2010) Superparamagnetic iron oxide nanoparticles: diagnostic magnetic resonance imaging and potential therapeutic applications in neurooncology and central nervous system inflammatory pathologies, a review. *Journal of cerebral blood flow and metabolism : official journal of the International Society of Cerebral Blood Flow and Metabolism,* 30(1): 15-35.

Wu , He Q and Jiang C (2008) Magnetic Iron Oxide Nanoparticles: Synthesis and Surface Functionalization Strategies. *Nanoscale Res Lett.* 3:397–415.

Wu W, Shen J, Banerjee P, Zhou S (2010) Core shell hybrid nanogels for integration of optical temperature-sensing, targeted tumor cell imaging, and combined chemophotothermal treatment. *Biomaterials.* 31: 7555-7566.

Xie H, Zhu Y, Jiang W, Zhou Q, Yang H, Gu N, Zhang Y, Xu H, Xu H and Yang X (2011) Lactoferrin-conjugated superparamagnetic iron oxide nanoparticles as a specific MRI contrast agent for detection of brain glioma *in vivo*. *Biomaterials.* 32: 495-502.

Xie J P, Zheng Y G and Ying J Y (2009) Protein-directed synthesis of highly fluorescent gold nanoclusters. *J. Am. Chem. Soc.* 131:888-9.

Xie J, Zheng Y and Ying J Y (2009) Protein-Directed Synthesis of Highly Fluorescent Gold Nanoclusters. *J. Am. Chem. Soc.*131: 888–889.

Xu X, Ray R, Gu Y, Ploehn H J, Gearheart L, Raker K and Scrivens W A (2004) Electrophoretic Analysis and Purification of Fluorescent Single-Walled Carbon Nanotube Fragments. *J. Am. Chem. Soc.* 126: 12736-12737.

Xu X, Ray R, Gu Y, Ploehn H J, Gearheart L, Raker K, Scrivens W A (2004) Electrophoretic analysis and purification of fluorescent single-walled carbon nanotube fragments. *J Am Chem Soc.*126(40):12736-7.

Xue B, Tong X D and Sun Y (2001) Characterization Of Pva-Based Magnetic Affinity Support For Protein Adsorption, *Separation Science And Technology.* 36(11):2449–2461.

Yang S T, Cao L, Luo P G, Lu F, Wang X, Wang H, Meziani M J, Liu Y, Qi G, Sun Y P (2009) Carbon Dots for Optical Imaging *in vivo* *J. Am. Chem. Soc.* 131: 11308-11309.

Yang Z, Li Z, Xu M, Ma Y, Zhang J, Su Y, Gao F, Wei H, Zhang L (2013) Controllable Synthesis of Fluorescent Carbon Dots and Their Detection Application as Nanoprobes. *Nano-Micro Lett.* 5(4): 247-259 (2013).

Yim H, Yang S G, Jeon Y S, Park I S, Kim M, Lee D H, Bae Y H and Kun Na (2011) The performance of gadolinium diethylene triamine pentaacetate-pullulan hepatocyte-specific T1 contrast agent for MRI. *Biomaterials.* 32: 5187-5194.

- Yim H, Yang S G, Jeon Y S, Park I S, Kim M, Lee D H, Bae Y H, Naa K (2011) The performance of gadolinium diethylene triamine pentaacetate-pullulan hepatocyte-specific T1 contrast agent for MRI. *Biomaterials*. 32: 5187-5194.
- Yin H, Liao L and Fang J (2014) Enhanced Permeability and Retention (EPR) Effect Based Tumor Targeting: The Concept, Application and Prospect. *JSM Clin. Oncol. Res.* 2(1): 1010
- Yu C, Li X, Zeng F, Zheng F and Wu S (2013) Carbon-dot-based ratiometric fluorescent sensor for detecting hydrogen sulfide in aqueous media and inside live cells. *Chem. Commun.* 49: 403-405.
- Zeng H and Sun S (2008) Syntheses, Properties, and Potential Applications of Multicomponent Magnetic Nanoparticles. *Adv. Funct. Mater.* 18: 391–400.
- Zhang C, Wängler B, Morgenstern B, Zentgraf H W, Eisenhut M, Unterecker H, Krüger R, Huss R, Seliger C, Semmler W, Kiessling F (2007) Silica- and Alkoxysilane-Coated Ultrasmall Superparamagnetic Iron Oxide Particles: A Promising Tool To Label Cells for Magnetic Resonance Imaging. *Langmuir*. 23: 1427-1434.
- Zhang R, Liu Y, Yu L, Li Z and Sun S (2013) Preparation of high-quality biocompatible carbon dots by extraction, with new thoughts on the luminescence mechanisms. *Nanotechnology*. 24: 225601.
- Zhang Y, Yang M, Park Ji-Ho, Singelyn J, Ma H, Sailor M J, Ruoslahti E, Ozkan M, and Ozkan C A (2009) Surface-Charge Study on Cellular-Uptake Behavior of F3-Peptide-Conjugated Iron Oxide Nanoparticles. *Small*. 5(17): 1990–1996.

Zheng J, Zhang C, and Dickson R M (2004) Highly Fluorescent, Water-Soluble, Size-Tunable Gold Quantum Dots. *PhysRevLett.* 93: 077402.

Zhou J, Booker C, Li R, Zhou X, Sham T K, Sun X and Ding Z (2007) An Electrochemical Avenue to Blue Luminescent Nanocrystals from Multiwalled Carbon Nanotubes (MWCNTs). *J. Am. Chem. Soc.* 129: 744-745.

Zhou Li, He B and Huang J (2013) Amphibious fluorescent carbon dots: one-step green synthesis and application for light-emitting polymer nanocomposites. *Chem. Commun.* 49: 8078-8080.

Zhu C, Zhaia J and Dong S (2012) Bifunctional fluorescent carbon nanodots: green synthesis via soy milk and application as metal-free electrocatalysts for oxygen reduction. *Chem. Commun.* 48: 9367–9369.

Zhu S, Meng Q, Wang L, Zhang J, Song Y, Jin H, Zhang K, Sun H, Wang H, and Yang B (2013) Highly Photoluminescent Carbon Dots for Multicolor Patterning, Sensors, and Bioimaging. *Angew. Chem. Int. Ed.* 52; 3953 –3957.

List of Publications

1. Ariya S, Shaiju S N, Madhumol J, Nimi N, Sabareeswaran A, Varma PRH, Jayasree R S., Citrate coated iron oxide nanoparticles with enhanced relaxivity for *in vivo* Magnetic Resonance Imaging of liver fibrosis., **Colloids and Surfaces B: Biointerfaces** 117 (2014) 216–224.
2. Nature India highlighted the research work entitled, ‘Magnetic Nanoparticles for Liver Imaging’, doi:10.1038/nindia.2013.164; Published online 10 December 2013.
3. Ariya S, Shaiju S N, Nimi N, Sabareeswaran A, Sachin JS, Jayasree R S., Synthesis and characterization of Dextran stabilized superparamagnetic iron oxide nanoparticles for *in vivo* MR imaging of liver fibrosis., **Carbohydrate Polymers**. 2014.101 (760– 768).
4. Shaiju S N, Saraswathy A, Gupta A K and Jayasree R S., Fluorescence spectroscopy to discriminate neoplastic human brain lesions: a study using the spectral intensity ratio and multivariate linear discriminant analysis., **Laser Phys.** 24 (2014) 025602 (12pp).
5. Nazeer SS, Saraswathy A, Gupta AK, Jayasree RS., Fluorescence spectroscopy as a highly potential single-entity tool to identify chromophores and fluorophores: study on neoplastic human brain lesions. **Journal of Biomedical Optics** (2013) 18 (6):067002-067002 .
6. Shaiju SN, Ariya S, Asish R, Haris PS, Anita B, Kumar GA, Jayasree RS., Habits with killer instincts: *in vivo* analysis on the severity of oral mucosal alterations using autofluorescence spectroscopy. **Journal of Biomed. Optics** 16(8), 087006 (August 2011).

7. Ariya S et al., “Optimum wavelength for the differentiation of brain tumour using autofluorescence spectroscopy”, **Photomed. Laser surgery, Mary Ann Liebert Inc.**, 27(3),2009,425-433.

Conference Proceedings

1. Poster presentation on “**Super Paramagnetic Iron Oxide Nanoparticles for in-vivo Magnetic Resonance Imaging of Liver Fibrosis**” in “2nd International Conference on Advanced Functional Materials,19th to 21st February 2014 and secured **Best Poster Award**.
2. Poster presentation on “**Alginate stabilized Super Paramagnetic Iron Oxide nanoparticles for in-vivo Imaging of liver fibrosis**” in “Indo-German Conference Laser Applications and Nanoscience, 5th to 7th December 2013.
3. Oral presentation on “**In-Vivo evaluation of liver fibrosis using Dextran stabilised Super Paramagnetic IronOxide nanoparticles**” in NCMST-2013 (IIST).
4. Oral presentation on “**A Novel Iron Oxide Based Contrast Agent For Magnetic Resonance Imaging Of Liver Diseases**” in 25th Kerala Science Congress, 2013.
5. Poster presentation on “**Ultra Small Superparamagnetic Ironoxide nanoparticles with high magnetic properties for Biomedical Applications**” in NSFC, 2011.(IIST).
6. Poster presentation on “**FT Raman and Autofluorescence Spectral Analysis of Human Brain tumor**” in Indo-French workshop on Biomedical Applications of Vibrational Spectroscopy and Imaging, 2010.
7. Oral presentation on “**Study on Progression of Atherosclerotic plaque using FT-Raman Spectroscopy**” in 21st Kerala Science Congress, 2009.
8. Poster presentation on “**Spectroscopic studies on Organically modified ceramic based dental composites**” in 19th Annual General Meeting of Material Research Society of India (MRSI-AGM 2008).

9. Poster presentation on “**Optimum Excitation Wavelength for the Demarcation of Brain Tumour**”, in National Conference on Recent Trends in Optoelectronics & Laser Technology (NCOL 2007).

Curriculum vitae

Education

PhD (2010 till date) Enrolled in January 2010 at SCTIMST, Kerala, India.

Advisor : Dr. R S Jayasree PhD

M.Phil (2004-2006) Photonics with 'A' grade from Department of Optoelectronics, University of Kerala, Kariavattom, Kerala.

M.Sc (2001-2003) Physics with **62.0 %** from S T Hindu College, Manonmaniam Sundaranar University, Nagercoil.

B.Sc (1998-2001) Physics with **83.0 %**, Mar Ivanios College, Kerala University, Kerala, India.

Experience

Worked as a **Technician (Instruments)** in SCTIMST, Trivandrum in the period **2007 - 2009**.

Personal Details:

Date of Birth : 25-04-1981
Sex : Female
Nationality : Indian
Marital Status : Married
Home address : Sreevalsam, TC 53/592
Karakkad Lane
Karakkamandapam, Nemom P O
Thiruvananthapuram
Mob:9895133418, 04712490198 (Home)
Email: ariya.saraswathy@gmail.com

